Dissertation
submitted to the
Combined Faculties for the Natural Sciences and for Mathematics
of the Ruperto-Carola University of Heidelberg, Germany
for the degree of
Doctor of Natural Sciences

presented by
Dipl. Phys. LEILA NAGEL
born in Karlsruhe

day of oral exam:
03.04.2014

Active Thermography to Investigate Small-Scale Air-Water Transport Processes in the Laboratory and the Field

Abstract: The active controlled flux technique is a tool to measure heat transfer velocities with a high temporal and spatial resolution. As heat, momentum and gas transport underlie the same physical processes, heat can be used as a proxy tracer for gases. Nevertheless the scaling of the measured heat transfer rates to the ones for gases is under discussion since the last decade due to the large differences in the diffusion constants of heat and gas. In this thesis simultaneous heat and gas transfer measurements have been conducted in the laboratory. Using an amplitude damping method, where the system response to different large-scale laser stimulations is investigated, a good agreement between scaled heat and gas transfer rates is found. The results show that, knowing the actual Schmidt number exponent, a scaling of heat to gas transfer rates is possible. During three campaigns in the Baltic Sea reliable transfer rates were determined. The obtained values are in the range of the expectations obtained from the laboratory measurements in the Aeolotron. They show, that the wind speed alone is not able to parametrise the gas transfer. Due to the different laser forcings required for this analysis, the integration time is in the order of 30 minutes. For an investigation of the underlying transport processes two fast analysis methods have been evaluated during laboratory measurements. The used methods are based on the surface renewal model. The results show, that these assumptions are too restrictive. To obtain reliable transfer velocities with a high temporal resolution, the development of a model independent analysis method is necessary.

Zusammenfassung: Aktive Thermographie ermöglicht die Messung von Wärmetransferraten mit einer hohen räumlichen und zeitlichen Auflösung. Da Wärme-, Impuls- und Gasaustausch durch die selben physikalischen Prozesse gesteuert werden, kann eine gemessene Transferrate für Wärme auf die von Gasen umskaliert werden. Jedoch ist diese Skalierung auf Grund der großen Unterschiede in den Diffusionskonstanten umstritten. Im Rahmen dieser Arbeit wurden gleichzeitig Wärme- und Gasauschtauschmessungen unter Laborbedingungen durchgeführt. Mit Hilfe einer Amplitudendämpfungsanalyse, bei der die Systemantworten auf unterschiedliche, großflächige Laser-Anregungen untersucht werden, konnte eine gute Übereinstimmung zwischen den skalierten Wärme- und Gasaustauschraten gefunden werden. Die Ergebnisse der Labormessungen zeigen, dass unter der Voraussetzung eines bekannten Schmidtzahlexponenten, die Skalierung von Wärme- auf Gasaustauschgeschwindigkeiten möglich ist. Während drei Messkampagnen in der Ostsee wurden Wärmetransferraten zuverlässig bestimmt. Die erhaltenen Werte liegen in einem, aus den Labormessungen im Aeolotron erwarteten Bereich und zeigen, dass die Windgeschwindigkeit alleine nicht ausreicht um den Gasaustausch zu parametrisieren. Auf Grund der notwendigen Anregungen mit verschiedenen Frequenzen beträgt die Messzeit pro zu bestimmender Austauschrate etwa 30 Minuten. Für eine detaillierte Untersuchung der zugrunde liegenden physikalischen Transportprozesse wurden bei zusätzlichen Labormessungen zwei weitere schnelle Analysemethoden auf der Basis des Oberflächenerneuerungsmodells evaluiert. Die dabei verwendeten Modellannahmen erwiesen sich als zu einschränkend. Zur verlässlichen Bestimmung von zeitlich hoch aufgelösten Transferraten ist die Entwicklung eines modellunabhängigen Verfahrens notwendig.

Contents

1. Introduction

In recent scientific and political discussions about the world's climate, the cycles of greenhouse gases play an important role. The most important and frequently investigated example for greenhouse gases is carbon dioxide [IPCC, 2007]. To understand the cycles of such gases their sources and sinks have to be investigated. This knowledge is necessary to improve the prediction of the world's climate. Next to the natural sources, anthropogenic sources (for example fossil fuel combustion or cement production, but also land-use) have played an important role since the beginning of the industrialisation. Two different sinks, terrestrial and oceanic, including the biospheres, take up the natural as well as the anthropogenic CO_2. In the average from 2002 to 2011 8.3 Gt carbon were emitted per year [Ciais et al., 2013]. As about $\frac{2}{3}$ of the world's surface is covered by oceans, the oceanic sink is very important, as it takes up about 30 % of this yearly emission. For carbon dioxide, [Le Quéré et al., 2013] found the ocean to be the main sink with 2.6 ± 0.5 Gt of carbon per year for the years 2003 - 2012. By this uptake the oceanic source reduces the increase rate of carbon dioxide in the atmosphere. However, this leads to an acidification of the ocean with unknown impact on sea dwellers, for example corals, algae, phyto- and zooplankton or bacteria [Feely et al., 2004].

The processes regulating the transport of gases from the atmosphere into the ocean have been investigated for several decades. The most important quantity characterising the air-sea gas exchange is the transfer velocity, which describes how fast gases are transported through the boundary layers existing at both sides of the air-sea interface. The thickness of this layers is determined by near-surface turbulence, which is influenced by different parameters. Wind flowing over the water surface transfers momentum to the water and creates waves which are increasing the subsurface turbulence.

The transfer velocity is commonly described as a function of the wind speed by empirical parametrisations [Ho et al., 2011]. As wind speed data are globally available and can be determined from satellite data, it is a parameter, which is easy to access. Nevertheless, other parameters are additionally influencing the near surface turbulence. One example are surfactants, which are damping waves and decrease the air-sea gas transfer [Frew, 1997]. Therefore, mean square slope, friction velocity or turbulent kinetic energy dissipation are supposed to be better parameters to describe the gas transfer [Garbe et al., 2014].

To improve the understanding of air-sea gas exchange and the influencing parameters, laboratory and field measurements are conducted. To do this, several different techniques to measure transfer rates are available (see for example [Nightingale, 2009]). They include mass balance and deliberate tracer methods, eddy correlation measurements and thermographic approaches. Each of these techniques has advantages and drawbacks, which make them applicable in different types of studies. Mass balance approaches are a very valuable tool for laboratory measurements, but have a very long integration time, which is in the order of hours to days under open ocean conditions [Liss, 1983]. Eddy covariance measurements are fast (in the order of some 10 minutes), but have a large footprint (in the order of kilometres) and have demanding technical requirements [Aubinet et al., 2012]. Thermographic measurements can be used both under laboratory and field conditions and have a high temporal (10 seconds to 20 minutes depending on the analysis method) and spatial (about 50 by 50 centimetres) resolution [Schimpf et al., 2011].

But thermographic techniques measure heat transfer velocities, which have to be scaled to the ones of gases by the so-called Schmidt number scaling [Liss and Slater, 1974].

Due to the described advantages, this thesis focusses on thermographic measurements. Since the thermographic measurements were proposed the first time to investigate ocean atmosphere interactions, a lot of different measurement procedures and analysis techniques have been developed, aided by the technical progress in camera and laser technology in the last decades.

The first time thermographic measurements of heat exchange were proposed by [Libner, 1987]. He used an active technique with periodic large scale heat forcings with different frequencies and Fourier analysis to determine the system response to the given heat flux. The comparison of the measured and scaled transfer rates to gas transfer velocities was promising, even though the heat transfer measurements seemed to give slightly higher results. He justified that by the difference occurring due to the comparison of the locally measured heat transfer velocities with the globally integrated gas transfer rates. Furthermore he found a clear fetch dependency for low wind speeds. [Jähne et al., 1989] used the same data for a more detailed process study.

In the work of [Haußecker, 1996] for the first time a laser was used as a heat source, heating up the water surface at a small spot. He simulated the propagation of the deposited heat to describe the temporal decrease of the temperature. By analysing the measured evolution of a heated patch, using the description obtained from the simulation, the response time of the system was determined.

Passive thermographic measurements were used by [Schimpf, 2000] and [Garbe, 2001] to determine transfer rates by using the surface renewal model. For the measured and scaled heat transfer velocities determined by [Schimpf, 2000] his comparison with empiric gas transfer parametrizations was successful. In addition, he detected turbulent structures and quantified them according to their size and orientation to gain an insight into the turbulent processes at the air water interface.

[Popp, 2006] developed the active controlled flux technique (ACFT) instrument for laboratory measurement. He obtained results for the heat transfer measurements with a heated area and an analysis of the temperature response in the Fourier domain. They are in good accordance with gas transfer parametrisations.

All these presented works showed a good agreement between measured heat transfer rates and gas transfer rates, which were either measured in the same facility or predicted with the help of empiric gas transfer parametrisations. They all indicate that a scaling between heat and gas transfer is possible.

However, there are also several works, which are in contradiction to this result. By using the analysis method proposed by [Haußecker, 1996], different studies under laboratory and field conditions found a difference of a factor of about two between scaled heat and measured gas transfer rates (see for example [Asher et al., 2004], [Atmane et al., 2004] or [Zappa et al., 2004]). Tracers, including gases and heat, have to diffuse through a thin layer at the air-water interface. As the diffusion constant for heat and carbon dioxide differ by two orders of magnitude, it is unclear if the underlying turbulent processes, influencing this diffusion layer are the same.

To solve this inconsistency further studies are necessary. Besides simultaneous heat and gas transfer measurements a detailed investigation of the possibilities and limitations of the different methods to analyse the ACFT images is necessary. To achieve that, different requirements for laboratory or field measurements have to be taken into account.

In this thesis four laboratory measurements at two different wind-wave facilities were conducted, using an ACFT instrument as developed by [Popp, 2006]. The obtained data was used to investigate the different analysis methods. Furthermore the most promising technique was tested under field conditions during three ship campaigns in the Baltic Sea.

This thesis is divided into seven chapters. After this introduction (chapter 1), chapter 2 introduces the theoretical background for the conducted work, including heat and gas transfer processes as well as the description of possible parameters influencing the air-sea gas transfer. Afterwards in chapter 3 the different measurement methods to measure gas transfer velocities, including mass balance approaches, eddy covariance techniques and different thermographic techniques for heat transfer measurements, are described in detail and compared to each other.

The focus of this work lies on measurements with active thermography, meaning that the water surface is heated up with a known flux density and image time series are acquired with an infrared camera. These images can be evaluated in different ways depending on the spatial and temporal flux density forced to the water surface. Chapter 4 describes four different analysis methods.

Chapter 5 describes the used instruments, the facilties and locations and the measuring procedures. The laboratory measurements, conducted in the wind-wave facilities in Heidelberg and Marseille, allow to compare the heat exchange measurements with measured gas exchange rates. The field measurements, conducted from research vessels in the Baltic Sea enable a comparison of the measured heat transfer rates with different empirical parametrisations of the gas transfer velocity with wind speed. As the measurements were conducted with the same technique as the laboratory measurements, they allow to compare between laboratory and ocean conditions. Chapter 6 shows the results for the heat transfer rates measured during the different laboratory and field campaigns. Furthermore comparisons of the heat with gas transfer measurements as well as of different analysis methods to determine heat transfer rates from thermographic measurements are shown. In the end chapter 7 will summarize the findings of this thesis and will give an outlook for future developments and measurements with thermography techniques.

2. Theory

This chapter describes the theoretical background needed for this thesis. It is divided in three sections. The first part (section 2.1) deals with topics concerning heat as a proxy tracer for air-sea gas exchange and includes a short introduction into the infrared radiometry. Section 2.2 describes the air-sea transport processes, which describes the exchange of all tracers, including gases, heat and momentum. Furthermore, empiric parametrisations found for the gas transfer velocity with wind speed are shown. In the last section (2.3) different parameters influencing air-sea gas exchange are introduced.

2.1. Heat

The mean heat energy $\overline{W}$ of a material is linked to its temperature T by

$$\overline{W} = \frac{f}{2} k_B T \tag{2.1}$$

with the Boltzmann constant $k_B = 1.381 \cdot 10^{-23} \frac{\text{J}}{\text{K}}$ and the number of degrees of freedom f of the molecule.

The heat Q is linked to the temperature T of an object by:

$$\frac{Q}{V} = \rho c_{\text{v}} T \tag{2.2}$$

V is the volume, ρ the density of the object and c_{v} is the specific heat at constant volume of the material. For water the specific heat is $c = 4.187 \frac{\text{kJ}}{\text{kg} \cdot \text{K}}$ [Erdmann, 2011].

2.1.1. Heat Fluxes

In general, three different types of heat fluxes can be distinguished: sensible, latent and radiative heat flux.

Sensible Heat Flux   The sensible heat flux results from the contact of two media with different temperatures T_1 and T_2. At the interface a heat flux from the cooler to the warmer media occurs. It lasts until both media have the same temperature. Under usual conditions on the ocean the sensible heat flux is between $j_{\text{s}} = -50 \frac{\text{W}}{\text{m}^2}$ and $+50 \frac{\text{W}}{\text{m}^2}$ [Popp, 2006].

Latent Heat Flux   The latent heat flux occurs due to the phase transformation from liquid to gaseous. Therefore, energy is needed which is taken from the water. In this process the water cools at the surface and an energy gradient from the water surface to the deep water is occurring and balanced by a resulting heat flux. The driving force for the latent heat flux is the humidity. The heat flux decreases with increasing humidity. Under natural conditions on the ocean, the latent heat flux can increase up to $j_l = -200 \frac{\text{W}}{\text{m}^2}$ [Popp, 2006].

Radiative Heat Flux   Electromagnetic radiation with wavelengths between $\lambda = 0.7\,\mu$m and $\lambda = 1000\,\mu$m is called infrared radiation. Each body emits radiation depending on its temperature. The spectral radiance ϕ is described by Plancks law:
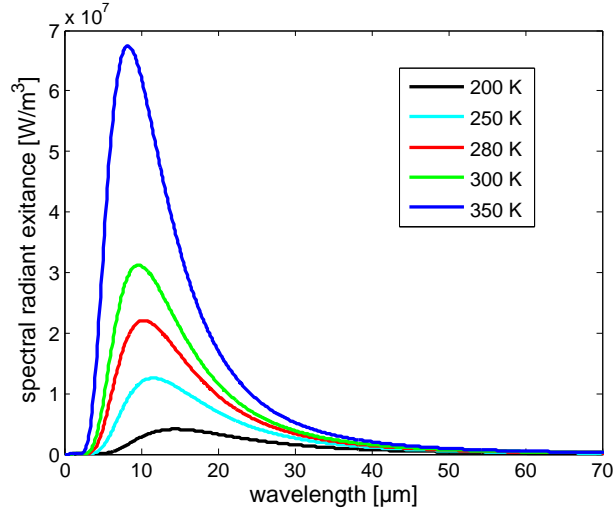
Figure 2.1.: Electromagnetic radiation described by Plancks law for different temperatures.

$$\phi\left(\lambda, T\right) = \frac{2\pi h c^2}{\lambda^5} \frac{1}{\left(e^{\frac{hc}{\lambda k_B T}} - 1\right)} \tag{2.3}$$

with the Planck's constant $h = 6.626 \cdot 10^{-34}$ Js, the speed of light $c = 2.99792458 \cdot 10^8\,\frac{\text{m}}{\text{s}}$ and the Boltzmann constant $k_B = 1.38 \cdot 10^{-23}\,\frac{\text{J}}{\text{K}}$. λ is the wavelength, which is given in μm and the Temperature T is given in Kelvin. Figure 2.1 shows this law for temperatures between 200 K and 350 K. As shown in the figure, the area under the curve increases and the maximum radiance is shifted towards lower wavelength with increasing temperatures.

Integrating equation 2.3 over all wavelengths yields to the heat flux density, described by the Stefan-Boltzman law:

$$j_{\text{rad}} = \int\limits_{-0}^{\infty} d\lambda \frac{dj_{\text{rad}}\left(\lambda, T\right)}{d\lambda} = \sigma T^4 \tag{2.4}$$

with the Stefan-Boltzmann constant $\sigma = 5.669 \cdot 10^{-8}\,\frac{\text{W}}{\text{m}^2\text{K}^4}$. The product of the wavelength with the emission maximum λ_{max} and the temperature T is a constant value. This is described by Wien's displacement law

$$\lambda_{\text{max}} T = 2891\,\mu\text{mK}. \tag{2.5}$$

Under natural conditions, the radiative heat flux depends a lot on environmental factors, like sun irradiation or cloudiness and can show in both directions, depending on weather and daytime.

In the following chapters only heat fluxes between water and air phase are considered. Thereby positive fluxes are defined as downwards directed, meaning the flux is directed from the air to

the water. For that case the sensible heat flux is

$$j_s = k_h \rho_a c_{pa} \left(T_a - T_s \right) \tag{2.6}$$

where k_h is the transfer rate for heat in the air, ρ_a is the density of air, c_{pa} is the specific heat in the air at constant pressure and T_s is the surface temperature. The latent heat flux is given by

$$j_l = -\lambda k_v c_e \left(1 - h \right) \tag{2.7}$$

with the evaporation heat λ, the transfer rate of water vapour k_v, the saturation concentration of water vapour c_e and the relative humidity h.

In addition to the heat fluxes between different materials, another transport mechanism in one fluid or gas exists:

Convection   Convection results from heat differences in one medium, for example in water. If water is heated up at one point, its density decreases and due to buoyancy the heated water moves upwards, while the unheated water flows downwards. If the convection results from other forces, for example a pressure gradient, it is called forced convection.
In difference to the other heat fluxes, convection yields not only to an energy transport, but also to a mass transport. Convection occurs in liquids or gases, but it transports no heat over the liquid gas interface.

2.1.2. Infrared Radiometry

Blackbody Irradiation   Each object emits and adsorbs energy (see section 2.1.1), depending on its temperature. The absorbance $\epsilon(\lambda)$ depends on the temperature and on the properties of the object and on the wavelength of the radiation λ. The object is called a blackbody, if $\epsilon = 1$ at all wavelengths and all incident energy is absorbed. A good absorber is always also a good emitter [Dereniak and Boreman, 1996].

Objects, which are not a blackbody are not able to absorb all incident radiation. For these materials, there is a part which is reflected with a rate $r(\lambda)$ and one, which is transmitted with the rate $\tau(\lambda)$. The energy conservation has to be fulfilled, leading to

$$\epsilon(\lambda) + r(\lambda) + \tau(\lambda) = 1, \tag{2.8}$$

which is called Kirchhoffs law.
Considering this law, radiators can be categorize in five types. A solid is called opaque radiator if there is no transmission: $\tau(\lambda) = 0$. It is called transparent, if all irradiation is transmitted: $\tau(\lambda) = 1$. At a mirror all incoming radiation is reflected: $r(\lambda) = 1$. And a blackbody absorbs all radiation $\epsilon(\lambda) = 1$. A physical body is called gray body, if the absorption ϵ is independent of the wavelength. Next to the absorption there is a part of the incoming irradiation, which is reflected $r(\lambda) = 1 - \epsilon(\lambda)$. The emitted radiation has the same spectral resolution as for a blackbody, but the effective radiated power is lower [Meschede, 2006].

In general the radiated power is depending on the irradiation angle. However, water surfaces act as a lamberts surface as long as the viewing angle is less than $\theta = 55°$, what means the irradiation is independent of the angle in the cut-off angles $0 - 55°$ [Haußecker, 1996].

Infrared detectores are only sensitive in a specific wavelength range. Therefore, the measured radiation is lower than the total emitted radiation of the observed object and equation 2.4 reduces to:

$$R_{\mathrm{D}}\left(T\right) = \int\limits_{\lambda_1}^{\lambda_2} \epsilon\left(\lambda\right) \frac{dj\left(\lambda, T\right)}{d\lambda} d\lambda \tag{2.9}$$

where R_{D} is the radiation absorbed by the infrared detector, λ_1 the lower bound and λ_2 the upper bound of wavelength, the detector is sensitive to. This integral has an explicit dependency on the temperature no matter which range of wavelengths is chosen. Therefore, the temperature can be determined by measuring the radiation.

2.1.3. Characteristics of the Water Surface in the Infrared

Incoming radiation is partly refracted, absorbed and reflected depending on the material of the body. This properties can be described with the help of the complex refraction index of the material:

$$N = n\left(\lambda\right) + ik\left(\lambda\right) \tag{2.10}$$

Snellius law states

$$\frac{\sin\vartheta_1}{\sin\vartheta_2} = \frac{n_2\left(\lambda\right)}{n_1\left(\lambda\right)} \tag{2.11}$$

where ϑ_1 is the angle of the incident radiation, ϑ_2 the angle of the radiation after passing the interface and with the refraction indice $n_1\left(\lambda\right)$ and $n_2\left(\lambda\right)$ for the different materials. At the water surface the refraction indexes are the one for air and water: $n_1 = n_{\mathrm{air}}$ and $n_2 = n_{\mathrm{water}}$. With a refraction index for air $n_{\mathrm{air}} = 1$ the refraction index for water is given by:

$$n_{\mathrm{water}}\left(\lambda\right) = \frac{\sin\vartheta_1}{\sin\vartheta_2} \tag{2.12}$$

The absorption $\beta\left(\lambda\right)$ of the water can be described by the imaginary part of the refraction index $k\left(\lambda\right)$ and is the inverse of the penetration depth $z_{\mathrm{p}}\left(\lambda\right)$:

$$\beta\left(\lambda\right) = \frac{1}{z_{\mathrm{p}}\left(\lambda\right)} = \frac{4\pi k\left(\lambda\right)}{\lambda} \tag{2.13}$$

The penetration depth in pure water for electromagnetic radiation with wavelengths from $\lambda = 2 - 60\,\mu\mathrm{m}$ is shown in figure 2.2. The values are taken from [Downing and Williams, 1975]. In the wavelength regime from $3 - 5\,\mu m$, which was used for the conducted infrared measurements, the penetration depth varies over three orders of magnitude.

The reflection at the water surface depends on the polarization of the incoming light. As polarization effects are not regarded in the framework of this work, the derivation of the reflectivity will be skipped here. It can be found for example in [Meschede, 2006]. The reflectivity depends on the wavelength of the incident radiation and can be described for small angles by:

$$r\left(\lambda\right) = \frac{\left(n\left(\lambda\right) - 1\right)^2 + k\left(\lambda\right)^2}{\left(n\left(\lambda\right) + 1\right)^2 + k\left(\lambda\right)^2}. \tag{2.14}$$

In the wavelength regime of the infrared cameras, which is $3 - 5\,\mu\mathrm{m}$ see section 5.1.1, the averaged emissivity of pure water is $\epsilon = 0.9738$ and the averaged reflectivity is $r = 0.0262$. For $10.6\,\mu\mathrm{m}$, what is the wavelength of the used CO_2 laser (see section 5.1.5) even more energy
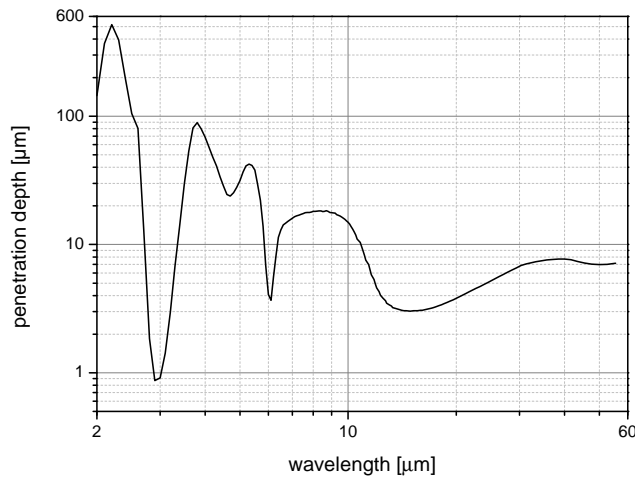
Figure 2.2.: Penetration depth of electromagnetic radiation in pure water - values taken from [Downing and Williams, 1975].

is absorbed, $\epsilon = 0.9924$ and the reflection is very low, $r = 0.00763$ [Downing and Williams, 1975].

2.1.4. Cool Skin Layer

Regarding the water temperature, in absence of sun irradiation, the temperature directly at the surface is found to be lower than in the water bulk. This effect is called cool skin layer.
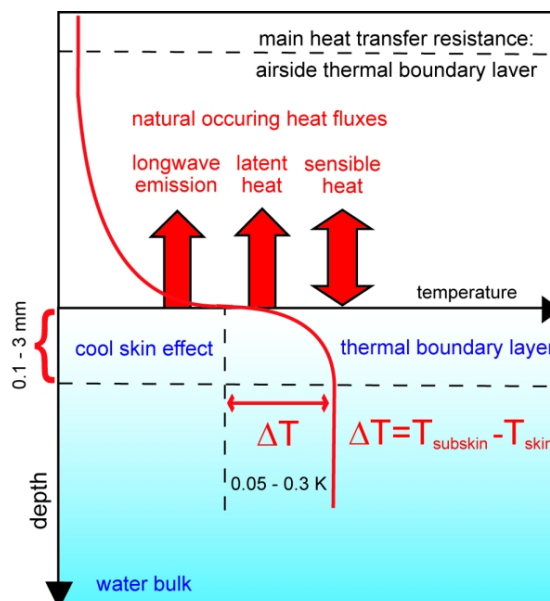
Figure 2.3.: Heat fluxes and resulting cool skin layer for conditions without sun irradiation.

In absence of sun irradiation, when the surface is not heated by the sun, the water at the ocean's surface is cooled down by latent heat flux. At night under clear sky conditions, the temperature of the clear sky is colder than the water temperature. Therefore, an additional cooling by radiative heat flux from the water to the air occurs. The sky acts like a black body and the water like a

gray body with an emission of $\epsilon = 0.95$. The net heat flux can be calculated by:

$$j = j_\mathrm{l} + \epsilon_\mathrm{sky}\epsilon_\mathrm{w}\left[j_\mathrm{rad}\left(T_\mathrm{sky}\right) - j_\mathrm{rad}\left(T_\mathrm{w}\right)\right] \tag{2.15}$$

These reflections can distort the measured temperatures by up to $0.7\,\mathrm{K}$ [Haußecker, 1996]. The temperature difference between surface and bulk water is in the order of $0.01 - 0.1\,\mathrm{K}$ [Fairall et al., 1996]. Figure 2.3 shows the natural occurring heat fluxes and the resulting cool skin layer at the water surface.

On sunny days, this process can be reversed. The radiative heat flux can superpose the latent heat flux and the surface water is warmer than the bulk [Saunders, 1967].
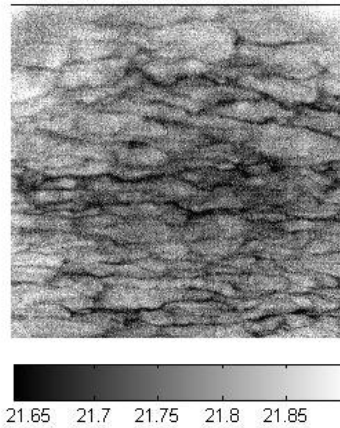
Figure 2.4.: Infrared image taken in the Heidelberg Aeolotron in September 2001, showing the typical cold streaks occurring at the water surface due to evaporation. The structure shows the near surface turbulence. Taken from [Nagel, 2009].

Nevertheless, under all conditions the surface temperature is not homogeneously distributed. Regarding the spatial distribution of the surface temperature a pattern of streaks is visible. This is caused by areas where surface divergence exists due to turbulences. The turbulent transport processes will be described in detail in section 2.2. At this point it is only important, that there are parts of the water surface, which are renewed with warmer bulk water by turbulence and there are divergences, which are in contact with the air for a longer time than the surrounding water, which is less cooled. Therefore, the inhomogeneous surface temperature arises. Figure 2.4 shows this typical streaks in an infrared image of the water surface.

2.2. Air-Sea Interaction

This section describes the transport processes across the water surface for momentum, heat and gases. There are many publications, giving an overview over these transport processes. Examples are [Jähne, 2009], [Nightingale, 2009] or [Liss and Johnson, 2014].

2.2.1. Diffusion and Turbulent Transport

Gases, heat and momentum can be transported by two different mechanisms: diffusive and turbulent transport. Turbulent transport is very effective for long distances and mixes the tracer away from the interface. With closer distances to the water surface, eddies become smaller, because they can not penetrate the water surface. This regime, in which the diffusion dominates, is called the diffusive (or molecular) boundary layer and has a thickness of $20 - 200\,\mu\mathrm{m}$ on the water-side and up to $1\,\mathrm{cm}$ at the air-side.

In this section all transport processes are described for gases. Nevertheless, it holds for heat and momentum, too. To convert the formulas to heat the concentration c is replaced by the temperature T and the diffusion constant D is replace by the thermal diffusivity a, which corresponds to the heat conductivity divided by the density and the specific heat $a = \frac{\lambda}{\rho c_\mathrm{p}}$. To get the description for momentum, the concentration c is replaced by the flow rate v and the diffusion constant D is replaced by the kinematic viscosity ν. Therefore, the diffusive boundary layer for momentum is often called viscous boundary layer, while fore gases, it is called mass boundary layer.

A concentration difference Δc causes a flux, which tries to balance the difference. This transport process is called diffusion and is described by Fick's first law

$$j = -D\nabla c \tag{2.16}$$

where j is the flux and D is the diffusion constant.

When there are no sinks and sources, the continuity equation is given by:

$$\frac{dc}{dt} + \nabla j = 0 \tag{2.17}$$

Combining equation 2.16 and 2.17 leads to Fick's second law, which is also called diffusion equation

$$\frac{dc}{dt} = -\nabla j = D\nabla^2 c. \tag{2.18}$$

By splitting of the total differential in equation 2.18 the transport equation is given by

$$\frac{\partial c}{\partial t} = D\Delta c - \vec{u}\nabla c. \tag{2.19}$$

This formulation divides the transport into a diffusive part due to the concentration difference and an advective part due to the velocity field $\vec{u}$.

The diffusion only dominates the turbulence in a thin layer at the-air water interface. With larger distance to the water surface the turbulent transport prevails. To describe this turbulent transport a turbulent diffusion coefficient can be defined in analogy to equation 2.16:

$$j = (D + K(z))\nabla c \tag{2.20}$$

where $K(z)$ is the turbulent diffusion constant. It is related to the water depth z by [Jähne, 2009]

$$K(z) = \frac{\kappa}{Sc_\mathrm{t}} u_* z \tag{2.21}$$

where the Karman constant $\kappa = 0.41$, Sc_t is the turbulent Schmidt number (see equation 2.50) and u_* the friction velocity, which will be explained in detail in section 2.3.1.

In a stationary homogeneous case and when the continuity equation holds, equation 2.20 can be integrated to

$$c(z_\mathrm{r}) - c(0) = j \int_0^{z_\mathrm{r}} \frac{1}{D + K(z)} dz \tag{2.22}$$

which gives the concentration profile over the depth.

The ratio of the concentration difference between water and air and the resulting flux has the dimension of a velocity. It is called transfer velocity k and is given by

$$k = \frac{j}{\Delta c}. \tag{2.23}$$

The transfer velocity is independent of the concentration and can be regarded as the velocity with which a gas is transported through the diffusive boundary layer. It is an averaged property and does not explain the underlying processes. In literature the transfer velocity is also called transfer rate or piston velocity. These different terms will be used in an identical way in this thesis.

The transfer resistance is defined as the inverse of the transfer velocity:

$$R = \frac{1}{k} = \frac{\Delta c}{j} \tag{2.24}$$

In analogy to electrical resistances, the total transfer resistance can be regarded as the sum of the resistances of the water and the air-side [Liss and Slater, 1974]:

$$R_{\text{tot}} = \alpha R_{\text{a}} + R_{\text{w}}. \tag{2.25}$$

In terms of the transfer velocity equation 2.25 becomes:

$$\frac{1}{k_{\text{tot}}} = \frac{\alpha}{k_{\text{a}}} + \frac{1}{k_{\text{w}}}. \tag{2.26}$$

where α is the dimensionless Ostwald solubility (see section 2.2.6).

Like described at the beginning of this section, these formulations for the gas transfer can be converted in the ones for heat or momentum. For the heat transfer the concentration in equation 2.23 has to be replaced. As the measured variable is not heat but temperature equation 2.2 can be used for conversion. Than the transfer velocity for heat is:

$$k_{\text{h}} = \frac{j_{\text{h}}}{\rho c_{\text{v}} \Delta T} \tag{2.27}$$

where ρ is the density, c_{v} the specific heat at constant volume and ΔT the temperature difference between air and water.

2.2.2. Reynolds Number

The Reynolds number is a dimensionless quantity to characterize the ratio of convection to diffusion. It is defined as:

$$Re = \frac{\rho v d}{\eta} = \frac{v d}{\nu} \tag{2.28}$$

where ρ is the density, v the characteristic drift velocity, d the characteristic length, η the dynamic viscosity and ν the kinematic viscosity.

At a specific Reynolds number Re_{crit} the flow turns from laminar to turbulent.

2.2.3. Boundary Layer Thickness and Time Constant

Close to the water surface molecular diffusion is the dominant transport process. The thickness of this diffusive boundary layer is given by:

$$z_* = \frac{D}{k}. \tag{2.29}$$

In this laminar layer a constant flux yields to a linear increase of the concentration. For that reason the boundary layer thickness z_* can also be determined geometrically. Then it is given as the intercept of a tangent to the concentration profile at the surface and the tangent to the bulk concentration. Figure 2.5 shows this geometrical relationship. Typical sizes of the water sided boundary layer are $20 - 200 \, \mu\text{m}$ [Jähne, 1985].
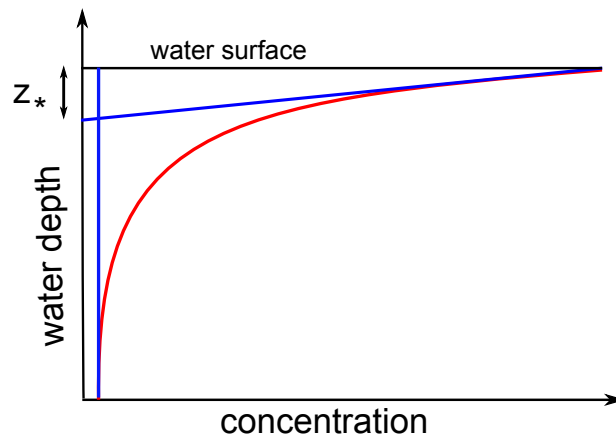
Figure 2.5.: Concentration profile and geometrical construction of the boundary layer thickness - modified after [Schimpf, 2000]

In analogy an air-sided boundary layer exists. The diffusion constants for tracers in air are larger than in water. Therefore, the air-sided boundary layer is two order of magnitude larger.

The time to cross this diffusive boundary layer is given by the response time

$$\tau = \frac{z_*}{k} = \frac{D}{k^2} \tag{2.30}$$

Typical time constants are in the order of $0.04 - 4 \, \text{s}$. There are three different parameters describing the air sea gas exchange: the transfer velocity k, the boundary layer thickness z_* and the time constant τ. Each of them can be calculated from the others, using equations 2.29 and 2.30. If the diffusion constant is known, only one of the parameters must be measured to investigate the exchange process.

2.2.4. Fluxes and Partial Pressure

The flux of a gas is linked to its difference of the partial pressures in air and water by:

$$j = kK_\alpha \left(p\left(\text{Gas}_\text{w} \right) - p\left(\text{Gas}_\text{a} \right) \right) \tag{2.31}$$

where k is the transfer rate and K_α the aqueous solubility in unit concentration per pressure. It is linked to the dimensionless Ostwald solubility α by the ideal gas constant R and the water temperature T_w by:

$$K_\alpha = \alpha \left(RT_\text{w} \right)^{-1} \tag{2.32}$$

The Ostwald solubility is defined by

$$\alpha = \frac{c_{\mathrm{w}}}{c_{\mathrm{a}}} \tag{2.33}$$

where the concentration of water c_{w} and air c_{a} are given in $\left[\frac{\mathrm{mol}}{\mathrm{l}}\right]$.

2.2.5. Navier-Stockes Equation and Reynolds Approach

The velocity field $\vec{u}$ of a liquid is described by the Navier-Stockes equation for incompressible fluids:

$$\frac{\partial \vec{u}}{\partial t} + \vec{u}\nabla\vec{u} = \vec{f} - \frac{1}{\rho}\nabla p + \nu \bigtriangleup \vec{u} \tag{2.34}$$

where ν is the kinematic viscosity, p the pressure, ρ the density and $\vec{f}$ the sum of all other forces, applied to the fluid. Because of the non-linearity the Navier-Stockes equation can only be solved numerically. To solve it analytically boundary conditions can be used to linearise the equation.

The Reynolds approach separates the velocity field and the concentration in mean and fluctuating parts:

$$\begin{aligned} \vec{u} &= \langle\vec{u}\rangle + \vec{u}' \\ c &= \langle c\rangle + c' \end{aligned} \tag{2.35}$$

The fluctuation components are statistical oscillations with high frequencies. The mean value of the velocity field equal zero,$\langle\vec{u}\rangle = 0$, if the integration time is high in comparison to the time constants of the fluctuations. Combing this assumption with equation 2.35 and the transport equation 2.19 results in [Popp, 2006]:

$$\frac{\partial\langle c\rangle}{\partial t} + \langle\vec{u}\rangle\nabla\langle c\rangle = -\nabla\langle\vec{j}\rangle = -\nabla\left[\langle c'\vec{u}'\rangle - D\nabla\langle c\rangle\right] \tag{2.36}$$

where $\langle\vec{j}\rangle$ is the sum over all turbulent and diffusive fluxes.

The equation can be simplified, if a one-dimensional current in x-direction can be assumed and the concentration does only change with the water depth, which is defined as z-direction. These boundary conditions can be expressed as:

$$\begin{aligned} u_y &= u_z = 0 \\ \frac{\partial c}{\partial x} &= \frac{\partial c}{\partial y} = 0 \end{aligned} \tag{2.37}$$

Applying these boundary conditions to equation 2.36 yields to an averaged flux density

$$\langle j\rangle = -\left(D\frac{\partial\langle c\rangle}{\partial z} - \langle u_x' u_z'\rangle\right) \tag{2.38}$$

and for the velocity field to the Reynolds equation:

$$\frac{\partial\langle u_x\rangle}{\partial t} = \rho\frac{\partial}{\partial z}\left(\nu\frac{\partial\langle u_x\rangle}{\partial z} - \langle u_x' u_z'\rangle\right) \tag{2.39}$$

where $\langle u_x' u_z'\rangle$ is called Reynolds stress.

2.2.6. Air- and Water-Side Controlled Tracers

Regarding the distributiom of a gas concentration with height, there is a discontinuity of the concentration at the water surface due to the solubility, which is described by Henry's law

$$c_{\mathrm{ws}} = \alpha c_{\mathrm{as}} \tag{2.40}$$

where c_{ws} is the water concentration at the surface, c_{as} the air concentration at the water surface and α the dimensionless Ostwald solubility (see section 2.2.4).
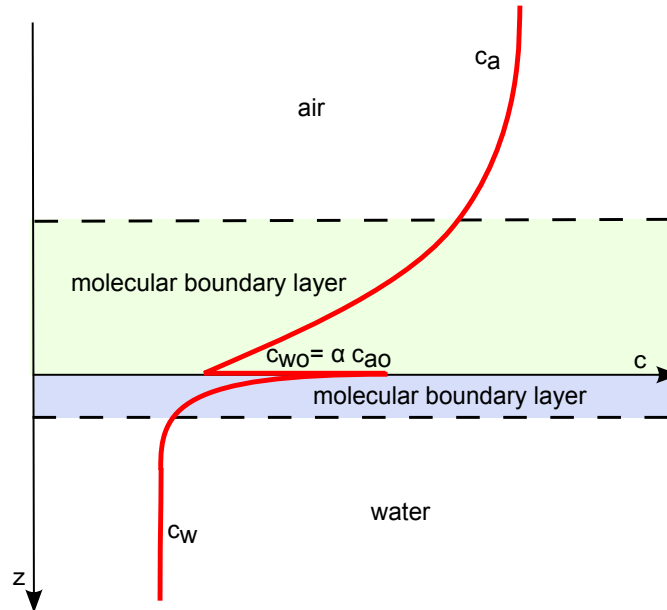
Figure 2.6.: Concentration profile at the air water interface - image taken from [Kräuter, 2011]

Figure 2.6 shows a typical concentration profile with a jump at the air water interface due to Henry's law. The air-side boundary layer is marked in green, the water-side boundary layer in blue.

A tracer has to cross both boundary layers. Therefore, the total transfer velocity as well as the total transfer resistance can be splited into a water (k_{w} or R_{w}) and an air sided part (k_{a} or R_{a}) (see section 2.2.1). Additionally the profile can be regarded from an air-side or a water-side perspective:

$$
\begin{aligned}
\text{airside}: \quad & \frac{1}{k_{\mathrm{at}}} = \frac{1}{k_{\mathrm{a}}} + \frac{1}{\alpha k_{\mathrm{w}}}, \quad R_{\mathrm{at}} = R_{\mathrm{a}} + \frac{R_{\mathrm{w}}}{\alpha} \\
\text{waterside}: \quad & \frac{1}{k_{\mathrm{wt}}} = \frac{\alpha}{k_{\mathrm{a}}} + \frac{1}{k_{\mathrm{w}}}, \quad R_{\mathrm{wt}} = \alpha R_{\mathrm{a}} + R_{\mathrm{w}}
\end{aligned}
\tag{2.41}
$$

An observer sees a constant profile, while the air- or the water-side concentration, depending on his position, is modified by the solubility.

Gases with a low solubility have their main resistance in the water and are therefore called water side controlled gases. Gases with a high solubility have their main resistance in the air and are called air side controlled gases.

Figure 2.7 shows the dimensionless solubility α over the Schmidt number Sc (see section 2.2.7) for the tracer used in the framework of this thesis. [Kräuter, 2011] deduced, that the ratio
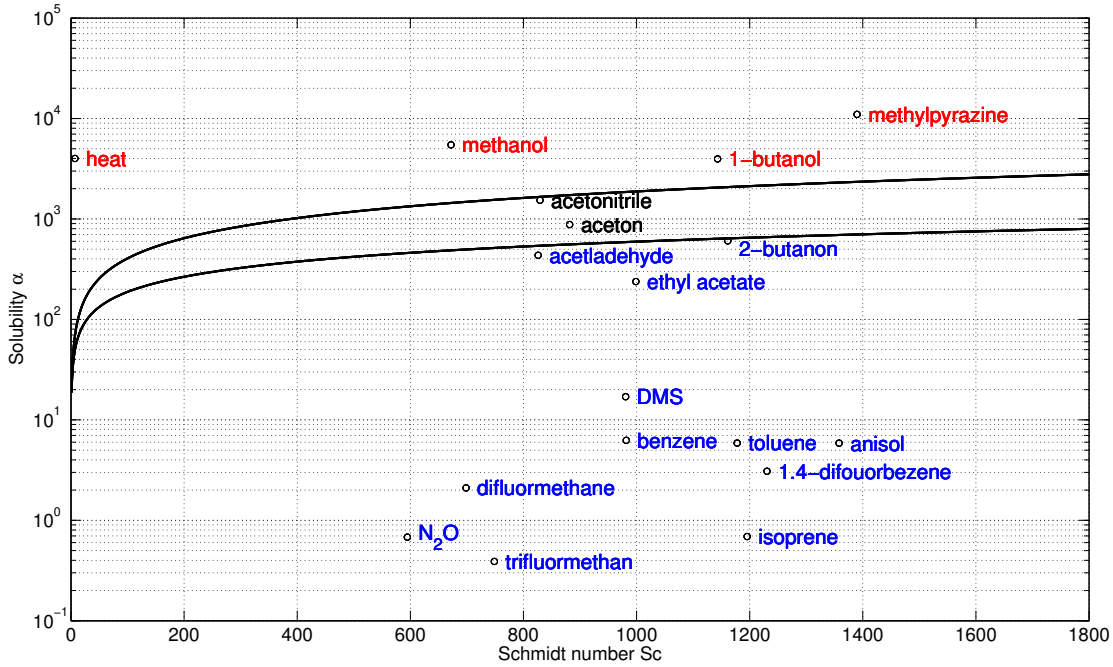
Figure 2.7.: Solubility α over the Schmidt number Sc for the used gases and heat - modified after [Kräuter, 2011]

of the air and the water sided resistances is:

$$\frac{\alpha R_\mathrm{a}}{R_\mathrm{w}} = 0.055 \cdot \alpha \cdot Sc_\mathrm{w}^{-n} \tag{2.42}$$

The solid lines in the figure show at which solubility and Schmidt number, the air- and the water-side resistance have the same values: $\frac{\alpha R_\mathrm{a}}{R_\mathrm{w}} = 1$. Tracers, which are lying over these lines are air-sided controlled, they are marked in red. Tracers under these lines are water sided controlled and marked in blue. In-between the two lines, which represent the smooth ($n = \frac{2}{3}$) and the rough ($n = \frac{1}{2}$) water surface, is the transition zone. For tracers in the transition zone both, the water- and the air-side resistance are of the same order. For most of the gases the contributions of both, the air- and the water-side resistance, to the total transfer resistance have to be considered.

Heat is also included in figure 2.7. The solubilty of heat is defined by the specific heat c_p in air and water and the densities ρ:

$$\alpha_\mathrm{heat} = \frac{\rho_\mathrm{a} c_\mathrm{pa}}{\rho_\mathrm{w} c_\mathrm{pw}}. \tag{2.43}$$

Analogously with that the solubility for momentum is defined by:

$$\alpha_\mathrm{momentum} = \frac{\rho_\mathrm{a}}{\rho_\mathrm{w}}. \tag{2.44}$$

2.2.7. Schmidt Number Scaling

Theoretical modelling shows that the transfer velocity can be described by [Deacon, 1977]

$$k = \frac{1}{\beta} u_* Sc^{-n} \tag{2.45}$$

where u_* is the friction velocity (see section 2.3.1), β is a constant, Sc is the Schmidt number and n the Schmidt number exponent. β and n depend on the surface conditions. The Schmidt

number is a dimensionless variable, which depends on the tracers properties. It is defined as the quotient of the kinematic viscosity and the diffusion constant:

$$Sc = \frac{\nu}{D} \tag{2.46}$$

In general the Schmidt number exponent changes from $n = \frac{2}{3}$ for a completely flat to $n = \frac{1}{2}$ for a wavy water surface [Jähne, 1980]. For heat the Schmidt number is also called Prandtl number Pr and can be expressed by

$$Pr = \frac{\nu \rho c_{\mathrm{v}}}{\lambda} \tag{2.47}$$

thereby ρ is the density, c_{v} the specific heat capacity at a constant pressure and λ the heat conductivity.

The Schmidt number is defined both, in the air and in the water. While the water-side Schmidt numbers span a huge range of values (for example at $20°C$ heat has a Prandtl number of 7, while CO_2 has a Schmidt number of 600), the air-side Schmidt number is closed to one for gases, heat and momentum. This implies, that the air-side boundary layer thickness for gases, heat and momentum have nearly the same size.

Transfer rates of different tracers can be scaled to each other. By dividing equation 2.45 for both tracers one gets:

$$\frac{k_1}{k_2} = \left(\frac{Sc_2}{Sc_1} \right)^n \tag{2.48}$$

With this formula the transfer rates of different gases, measured under the same surface conditions, can be calculated from each other, if the Schmidt numbers are known. If in addition to the friction velocity, the water temperature is the same for both measurements, the kinematic viscosity is identical and the Schmidt number can be substituted by the diffusion constants:

$$\frac{k_1}{k_2} = \left(\frac{D_1}{D_2} \right)^n \tag{2.49}$$

However, it is not possible to use equation 2.48 to calculate the transfer velocity of a water-side controlled tracer from the one for an air-side controlled tracer.

For the turbulent transport a turbulent diffusion constant was defined in equation 2.20. For that reason a turbulent Schmidt number can be defined by:

$$Sc_t = \frac{K_{\mathrm{m}}}{K_{\mathrm{c}}} \tag{2.50}$$

where K_{m} is the turbulent diffusion constant for momentum and K_{c} is the turbulent diffusion constant for the concentration of the tracer.

2.2.8. Gas Transfer Models

There are several models, trying to describe the transition from diffusive to turbulent transport.

Film Model   The film model was first described by [Whitman, 1923] as a general model for liquid gas interfaces. [Liss and Slater, 1974] adopted it to the atmosphere ocean interface. It assumes a turbulent and therefore well mixed bulk, with a constant concentration c_{bulk}. Close to the interface, it assumes a completely separated stagnant layer, where only diffusion takes place. The size of this layer corresponds to the boundary layer thickness z_* (see section 2.2.3). In this film layer the flux is laminar and therefore the concentration linearly increases towards the bulk. The Reynolds number increases with depth. When it reaches the critical value the flux becomes turbulent in the bulk. Therefore, the bulk is well mixed. As no turbulent transport occurs in the film layer, the transfer velocity is directly proportional to the diffusion constant D:

$$k = \frac{D}{z_*} \tag{2.51}$$

where z_* is the boundary layer thickness. This model can be regarded as a lower limit for the transfer velocities as it is not a physical assumption, that the turbulence ends suddenly at a specific water depth and any turbulence in the boundary layer would increase the gas exchange. The concentration profile with depth can best be described with dimensionless variables:

$$c_+ = \frac{c - c_{\mathrm{b}}}{c_{\mathrm{s}} - c_{\mathrm{b}}} \qquad \text{and} \qquad z_+ = \frac{z}{z_*} \tag{2.52}$$

where c_{b} is the bulk concentration, c_{s} the concentration at the water surface and z_* the boundary layer thickness. With these definitions the concentration profile with depth is given by

$$c_+ \left(z_+ \right) = 1 - z_+ \qquad \text{for } 0 < z_+ < 1. \tag{2.53}$$

Small Eddy Model   The small eddy model, which is also called diffusion model, assumes that turbulent transport is conducted by eddies. The eddy size decreases with decreasing distance to the water surface, as they can not penetrate the air-water interface. To describe this assumption a turbulent diffusion constant is defined. It is zero at the water surface and increases with increasing water depth ([Coantic, 1986]). Thus directly at the water surface the diffusion is still the dominant transport process. With increasing distance to the surface, the turbulence gets more and more effective until it is the dominating process in the bulk. For the turbulent diffusion coefficient a quadratic profile is assumed: $K \left(z \right) = \alpha z^2$. Out of this assumption the concentration profile can be assumed to be [Reichardt, 1951]:

$$K \left(z \right) = \kappa u_* \left(\frac{z}{z_1} - \tanh \frac{z}{z_1} \right) \tag{2.54}$$

where κ is the Karman constant, u_* the friction velocity and z_1 a constant which has to be determined from experiments. This profile is valid for the case of a flat water surface.

Based on this profile [Deacon, 1977] found a description of the transfer resistance R_{w}. Thereby the Schmidt number exponent as well as the constant of proportionality depend on the Schmidt number. For small Schmidt numbers (like for heat) n was found to be 0.61, and $\frac{2}{3}$ for higher Schmidt numbers in case of a smooth water surface:

$$R_{\mathrm{w}} = \begin{cases} 15.2 Sc^{0.61} & \text{for } 0.6 < Sc < 10 \\ 12.1 Sc^{\frac{2}{3}} + 2.7 \log_{10} Sc + 2.9 & \text{for } Sc > 10 \end{cases} \tag{2.55}$$

This formulation is only valid for a flat water surface.

In a more general way the transfer rates for high Schmidt numbers can be written as

$$k \propto Sc^{-1+\frac{1}{m}} u_* \tag{2.56}$$

where the Schmidt number exponent $n = -1 + \frac{1}{m} = \frac{2}{3}$ for a rigid wall and $n = \frac{1}{2}$ for a free surface.

The concentration profile depends on the choice of m. For a rigid wall ($n = \frac{2}{3}$) [Friedl, 2013] solved the transport equation and got a concentration profile which is given by

$$c_+ (z_+) = \frac{3}{4} + \frac{3}{2\pi} \tan^{-1} \left(\frac{1}{\sqrt{3}} - \frac{4\pi}{9} z_+ \right) - \frac{\sqrt{3}}{2\pi} \ln \left(9 + 2\sqrt{3}\pi z_+ \right)$$
$$+ \frac{\sqrt{3}}{4\pi} \ln \left(3 \left(27 - 6\sqrt{3}\pi z_+ \right) + 4\pi^2 z_+^2 \right) \tag{2.57}$$

using again the dimensionless constants defined in equation 2.52. For a free surface ($n = \frac{1}{2}$) it is described by:

$$c_+ (z_+) = \frac{2}{\pi} \cot^{-1} \left(\frac{\pi}{2} z_+ \right) \tag{2.58}$$

Surface Renewal Model   Similar to the film model, the surface renewal model assumes two different layers: a diffusive layer at the water surface and a turbulent mixed bulk. In difference to the film model, the diffusion layer is sometimes penetrated by a surface renewal event, which replaces the surface water by water from the depth at a certain position. The surface renewal model was first introduced for applications in chemical engineering by [Higbie, 1935]. He assumed periodically recurring renewal events with a constant renewal time. [Danckwerts, 1951] improved the model by replacing the periodically by statistically distributed surface renewal events. They are characterized by the mean time between two renewal events, which is called the renewal time τ. It is influenced by several parameters like waves, convection, wave breaking, rain or surfactants. This renewal time and thus the renewal rate $\lambda = \frac{1}{\tau}$, is depth dependent. It can be described by $\lambda = \gamma_p z^p$. In that case $p \geq 0$ is the probability density function which describes the probability that a renewal event takes place in a time interval $[t, t + \Delta t]$. This leads to a description for the transfer rate:

$$k \propto Sc^{-1 + \frac{1}{p+2}} u_*. \tag{2.59}$$

Like in the small eddy model, this leads to Schmidt number exponents of $n = \frac{2}{3}$ or $n = \frac{1}{2}$ depending on the surface condition. Out of these model assumptions the boundary layer thickness can be calculated by

$$z_* = \sqrt{D\tau}. \tag{2.60}$$

Therefore, the transfer velocity can be expressed as:

$$k = \frac{D}{\tau} \tag{2.61}$$

For the concentration profiles with depth, again two different cases have to be distinguished. For a rigid surface ($p = 1$), according to [Jähne et al., 1989], one gets:

$$c_+ (z_+) = \frac{1}{\text{Ai}(0)} \text{Ai} \left(-\frac{\text{Ai}(0)}{\text{Ai}'(0)} z_+ \right) \tag{2.62}$$

where Ai is the Airy function.

For a free surface ($p = 0$) the concentration profile with depth is given by:

$$c_+ (z_+) = \exp (-z_+). \tag{2.63}$$

The surface renewal model is often applied for heat exchange investigations. The temperature at the water surface can be assumed to be lower than the bulk temperature (see 2.1.4). The renewal events move warmer water to the surface. Between two renewal events the surface cools down because of the heat fluxes (see section 2.1.4).

Surface Penetration Model   A further development of the surface renewal model is the surface penetration model (which is also called random eddy model), first described by [Harriott, 1962]. It assumes that there are renewal events, which do not reach the water surface, but are only replacing a part of the boundary layer. For that reason in addition to the probability distribution function of the renewal time the distribution of the eddy approach distance z and the eddy lifetime distribution have to be taken into account. The assumptions for this model do not allow to scale between gases with huge differences in the boundary layer thickness, as the influence of the eddies differs a lot.

Facet Model   The Facet Model describes the continuous transition of the Schmidt number exponent from $n = \frac{2}{3}$ for a flat to $n = \frac{1}{2}$ for a wavy water surface. Therefore, the water surface is divided in two parts: a smooth area a_s and a wavy area a_w, which is increasing with increasing turbulence. In combination with equation 2.45 it can be described by

$$k = a_\mathrm{s} k_\mathrm{s} + a_\mathrm{w} k_\mathrm{w} = (1 - a_\mathrm{w}) \frac{u_*}{\beta_\mathrm{s}} Sc^{-n_\mathrm{s}} + a_\mathrm{w} \frac{u_*}{\beta_\mathrm{w}} Sc^{-n_\mathrm{w}} \tag{2.64}$$

[Zappa et al., 2002] showed in a laboratory study, that the wave area, which was quantified as a fractional area where microscale wave breaking occurs, is linked to the gas transfer velocities.

Comparison of the Models   Despite of the surface penetration model, all the models coincide in the relation between transfer velocity, Schmidt number and friction velocity:

$$k = \frac{1}{\beta} u_* Sc^{-n}. \tag{2.65}$$

Except for the film model, were $n = 1$, the variables for each of the models can be chosen in a way that the Schmidt number exponent becomes $n = \frac{2}{3}$ for a flat water surface. For rough water surfaces one gets $n = \frac{1}{2}$. This values can be determined, out of model independent considerations, at the boundary conditions (see [Jähne, 1980]). For air-side controlled tracers, the Schmidt number exponent was found to be $n = 0.61$ (see [Deacon, 1977]). The constant β was found to be $\beta = 16$ for the surface renewal model and for the small eddy model according to [Deacon, 1977] to be

$$\beta = \begin{cases} 15.2 & \text{for } 0.6 < Sc < 10 \\ 12.1 & \text{for } Sc > 10 \end{cases} \tag{2.66}$$

For the surface penetration model the transfer rate is not directly be scaled to the diffusion constant [Atmane et al., 2004].

However, the models differ significantly in the depth profiles of the concentrations. For that reason it is not possible to distinguish between the different models by measuring transfer velocities or Schmidt number exponents in dependency of the friction velocity. To investigate the different models a visualization technique to measure depth dependent concentrations is necessary (see for example [Münsterer, 1996], [Herzog, 2010] or [Friedl, 2013]).

2.2.9. Gas Transfer Parametrisations

There are a huge number of different semi-empiric and empiric parametrisations of gas transfer. Some of them are presented here and used later on for comparison. They are all scaled to $Sc = 660$ or $Sc = 600$ which are the Schmidt number for CO_2 at $20°C$ in sea or fresh water, respectively. As the forcing parameter, they all use wind speed in ten meters height u_{10}, as it is

very robust and can be determined from remote sensing from satellites.

LM-86 One often used semi-empiric parametrisation was developed by [Liss and Merlivat, 1986]. They used field data gained in lake measurements. This data were extrapolated to a larger wind speed regime, using knowledge from a number of different wind wave tunnel studies. In this parametrisation the exchange rates are divided in three different regimes: flat surface up to the wind speed $u_{10} = 3.6 \frac{m}{s}$, where the transfer rate is only slightly changing with wind speed, a wave influenced surface up to $u_{10} = 13 \frac{m}{s}$ where the change of the transfer velocity is increased and a regime, which is influenced by bubbles and breaking waves at higher wind speeds:

$$k = \begin{cases} 0.17\, u_{10}, & \text{for } u_{10} \leq 3.6 \frac{m}{s} \\ 2.85\, u_{10} - 9.65, & \text{for } 3.6 \frac{m}{s} \leq u_{10} \leq 13 \frac{m}{s} \\ 5.9\, u_{10} - 49.3, & \text{for } u_{10} \geq 13 \frac{m}{s} \end{cases} \tag{2.67}$$

This parametrisations holds for gases with a Schmidt number of $Sc = 600$ and includes a sudden jump from Schmidt number exponent $n = \frac{2}{3}$ for wind speeds $u_{10} < 3.6 \frac{m}{s}$, corresponding to a flat surface to $n = \frac{1}{2}$ for higher wind speeds,corresponding to a wavy surface. This jump is not confirmed by measurements (see for example [Krall, 2013]). In comparison with a huge number of field measurements a good agreement was found. Nevertheless, wind wave tank measurements are underestimated.

W-92 [Wanninkhof, 1992] proposed a quadratic relationship between the transfer rate for gases with Schmidt number $Sc = 660$ and wind speed. Laboratory data were used to determine the quadratic form of the parametrisation, field data were used to determine the absolute values. The parametrisation considers the integration times of the wind speed measurements. For instantaneous measurements or for steady state conditions, like in laboratory measurements, the best description of the relation between the measured transfer rates and the wind speed is:

$$k = 0.31 u_{10}^2 \left(\frac{Sc}{660} \right)^{-\frac{1}{2}} \tag{2.68}$$

For long time integrated wind speeds the parametrisation differs to:

$$k = 0.39 u_{10}^2 \left(\frac{Sc}{660} \right)^{-\frac{1}{2}} \tag{2.69}$$

The transfer velocities, predicted with this parametrisations, are underestimated in comparison to measured transfer velocities at high wind speeds. Furthermore, the parametrisation assumes open ocean conditions, as a limited fetch, like on small lakes, would decrease the transfer rates.

W-99 [Wanninkhof and McGillis, 1999] suggested a parametrisation with a cubic dependency of the CO_2 transfer rate ($Sc = 660$) with wind speed. They used eddy covariance measurements conducted in a sink region in the North Atlantic in 1998. There they collected more than 1500 data points with integration times of about 30 minutes. These data, which show a good agreement with dual tracer measurements, were plotted over the wind speed in ten meters height u_{10}. The resulting parametrisation for short integration time or steady state conditions is given by:

$$k = 0.0283 u_{10}^3 \left(\frac{Sc}{660} \right)^{-\frac{1}{2}} \tag{2.70}$$

And the one for a long integration time by:

$$k = \left(1.09u_{10} - 0.333u_{10}^2 + 0.078u_{10}^3\right) \left(\frac{Sc}{660}\right)^{\frac{1}{2}} \tag{2.71}$$

This parametrisation assumes a Schmidt number exponent of $n = \frac{1}{2}$ over the whole range of wind speeds.

N-2000 [Nightingale et al., 2000] used dual tracer measurements (with He, SF_6 and spores of a bacterium) under fetch limited conditions in the North Sea. They converted the measured transfer rates to the Schmidt number $Sc = 600$ by Schmidt number scaling (see section 2.2.7). The best fit of the data is given by

$$k = 0.222u_{10}^2 + 0.333u_{10} \tag{2.72}$$

W-09 Another parametrisation was proposed by [Wanninkhof et al., 2009]. They assume a cubic dependency with a non-zero intercept for zero wind speed as still buoyancy forces are creating fluxes. With this approach the relation between the transfer velocity and the shear stress is represented by the quadratic term, while the relation to energy dispersion is presented by the cubic term. To determine the values of the terms, he used a combination of different measurements and model assumptions, leading to

$$k = 3 + 0.1u_{10} + 0.06u_{10}^2 + 0.011u_{10}^3 \tag{2.73}$$

for averaged wind speeds. Nevertheless, for wind speeds less than $u_{10} = 15 \frac{m}{s}$ a quadratic approximation is sufficient:

$$k = 0.24u_{10}^2 \tag{2.74}$$
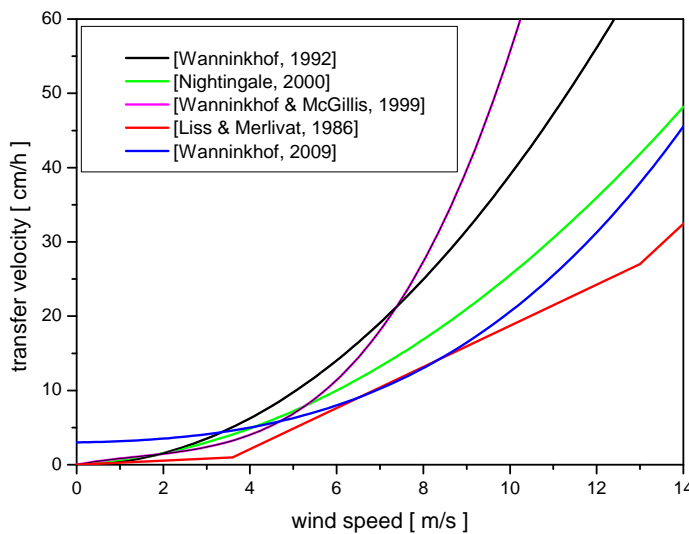
Figure 2.8.: Different parametrisations for the transfer velocities for CO_2 (Schmidt number $Sc = 600$) with the wind speed in ten meters height u_{10}.

Figure 2.8 show all the parametrisations, described in this section. There are significant differences in the parametrisations which can easily be a factor of two or more at higher wind speeds. Furthermore, the data used to determine the parametrisations scattered a lot, indicating that there are more parameters than the wind speed, influencing the transfer velocities. [Ho et al., 2011] used field data, obtained with dual tracer techniques (see section 3.1.4) and evaluated by different techniques to test the most commonly used parametrisations. For measurements with medium wind speeds from 6 to 12 $\frac{m}{s}$ all the tested parametrisations fitted quite well. However other measurements with a wider range of wind speeds from 2 to 16 $\frac{m}{s}$ W-92 and W-99 overestimate and LM-86 underestimates the measured transfer rates. Despite their different functional forms N-2000 and W-09 explain more than 80% of the variances in all $^3He/SF_6$ dual tracer measurements, so it is not possible to determine the form from the field measurements. [Ho et al., 2011] furthermore concludes that for slightly soluble gases wind speed can be considered as the dominant parameter influencing the air-sea gas exchange on time scales of days while other effects only have a small influence. Furthermore, parametrisations can be used to describe the gas exchange on varying locations, independent of the locations, where they were determined. These findings are confirmed by [Garbe et al., 2014] who compiles the findings of a huge number of measurements with different methods from different locations and authors. He agrees in the quadratic form of the N-2000 parametrisation. Furthermore, he concludes that the parametrisations are not valid for intermediate (or highly) soluble gases like DMS. These gases are less affected by the bubble mediated gas transfer (see section 2.3.4). For that reason there are deviations between the different parametrisations at high wind speeds.

2.3. Parameters Influencing the Air-Sea Gas Exchange

All existing parametrisations (see section 2.2.9) describe the transfer velocity in dependency of the wind speed. Although the driving force for the creation of waves is the wind, which smears over the water surface, the wind speed is only one of several parameters influencing the near surface turbulence and therefore the air-sea gas exchange. In this section different processes influencing the exchange and different parameters which could be candidates to parametrise the gas exchange are described. A summary of the most important parameters is for example given in [Garbe et al., 2014].

2.3.1. Friction Velocity and Wind Profile

For stationary cases, where the mean velocity and the mean concentration does not change with time, the Reynolds equation 2.39 can be integrated over the z-direction and yields to a constant flux density:

$$j_{\mathrm{m}} = \rho \left(\nu \frac{\partial \bar{u}_x}{\partial z} - \langle u'_x u'_z \rangle \right) =: \tau \qquad (2.75)$$

This corresponds exactly to the definition of the shear stress τ. To describe the momentum transport often the friction velocity u_* instead of the shear stress is used. It can be calculated from the shear stress divided by the density ρ:

$$u_*^2 = \frac{\tau}{\rho} \qquad (2.76)$$

It corresponds to the velocity of the momentum transported in the water.

The friction velocity can be defined for both, the air- and the water-side. They are related by their densities:

$$u_{*\mathrm{w}} = \sqrt{\frac{\rho_\mathrm{a}}{\rho_\mathrm{w}}} u_{*\mathrm{a}} \tag{2.77}$$

The shear stress does directly cause the wind profile far away from the boundary layer, where the turbulent transport of momentum dominates. It has a logarithmic shape, which is directly linked to the air-side friction velocity:

$$u\left(z\right) = u_{*\mathrm{a}} \kappa^{-1} \ln\left(\frac{z}{z_0}\right) \tag{2.78}$$

z_0 is the effective roughness of the water surface and κ the Karman constant, which is roughly 0.42. Due to this relation it is possible to determine the friction velocity by measuring the wind profile.

Furthermore, the wind speed in ten meter hight u_{10} can be linked to the air-side friction velocity by the drag coefficient C_d which acts a an air-side roughness parameter:

$$C_\mathrm{d} = \left(\frac{u_{*\mathrm{a}}}{u_{10}}\right)^2 \tag{2.79}$$

and to the water-side friction velocity:

$$u_{10} = \left(\frac{\rho_\mathrm{w}}{\rho_\mathrm{a}}\right)^{-\frac{1}{2}} u_{*\mathrm{w}} C_\mathrm{d}^{-\frac{1}{2}} \tag{2.80}$$

The friction velocity is one of the possible parameters which can be used to describe the air sea gas exchange.

2.3.2. Waves

The motion of the water surface does not directly influence the air-sea gas exchange. Nevertheless, waves play an important role regarding the air-sea interaction processes. Especially high frequency waves, having a short wave length, increase the momentum transfer because of the higher surface roughness. Additionally they vary the boundary layer thickness periodically. In wave troughs the boundary layer is thinner as it is stretched. In the wave crests it is compressed and therefore thicker. the averaged transfer velocity is increased by that process.

In opposite to this effects the direct increase of the water surface due to the waves is small. Furthermore, the increasing water surface decreases the flux density. Both processes balance out and the transfer velocity is not influenced.

Under laboratory conditions the waves are only produced by one process. They are either wind induced or grid stirred. Under field condition the wave field is an interference of the local created wind waves and the swell, which is created by storms in farer distances and can have other directions than the local wind waves.

There are different wave parameters which could be candidates for parametrise the air sea gas transfer.

Mean Square Slope

The mean square slope is a statistical wave parameter, which is defined as the variance of the surface slope:

$$\langle s^2 \rangle = \sigma^2 \qquad (2.81)$$

The mean square slope increases the gas exchange [Jähne et al., 1987]. As small capillary waves have steeper slopes then the long-wave gravity waves, they have a bigger influence on the transfer rates.

[Frew, 1997] found that the mean square slope is a better parameter than the wind speed to describe the air sea gas exchange at a surfactant covered water surface.

Wave Age

The wave age is a parameter, which considers that the wind has to smear over the water surface for a certain time until the wave field is developed. It is defined as the ratio of the phase velocity and the friction velocity $\frac{c_{\text{peak}}}{u_*}$. It distinguishes between young and mature waves. Young waves are generated by local wind, but had not the time to reach an equilibrium state. Mature wave did reach the equilibrium or are mainly influenced by swell.

Microscale Wave Breaking

Waves are breaking if the velocity of a fluid element near the wave crest higher than the propagation speed. They are called microscale breakers, if they do not entrain air during breaking. Nevertheless, they introduce additional near-surface turbulence by transporting energy and momentum from the wave field to the turbulence [Banner and Phillips, 1974].

[Zappa et al., 2004] found the fractional area coverage of microbreakers A_{B} to be a better parameter to describe the gas transfer velocity than the mean square slope.

$$k \propto (\epsilon \nu)^{\frac{1}{4}} Sc^{-n}. \qquad (2.82)$$

2.3.3. Surfactants

One very important influence on the wave field is the presence of surfactants. In general surfactants are substances which consist of two parts: a hydrophilic headt and a hydrophobic tail. The hydrophobic part is typically an alkyl chain with 8 to 18 carbon atoms. As this part of the molecule wants to avoid the presence of the water, it tends to stick to the water surface. Surfactants decrease the surface tension. Until a certain concentration is reached, they form a monomolecular layer at the water surface. If the concentration is high enough, excess molecules go into the water body and stick together in clusters to minimize the contact of the hydrophobic part with the surrounding water. This clusters are called micelles. For a more detailed description of the chemical properties and a classification of the different types of surfactants see for example [Tsujii, 1998].

In most cases the surfactant layer at the water surface is no direct barriers for the gas molecules [Liss, 1983]. But surfactants change the water surface elasticity and are working against contractions created by waves. Thereby they dampen waves and near-surface turbulence. They influence the energy input by wind shear as well as the energy dissipation in the wave field and the energy transfer. The influence is larger at low wind speeds as the films can rupture and be mixed in the bulk at high wind speeds. Especially soluble surfactants can reduce the air sea gas

transfer up to 50 % (see [Frew et al., 1990]), because they reduce the velocity of eddies and therefore decrease the surface renewal rates and increase the thickness of the viscous boundary layer. The value of the Schmidt number exponent (see section 2.2.7) depends on the surface condition, which is altered by the change in the elasticity of the water surface by the surfactant. Therefore, the gas transfer velocities are reduced in the presence of surfactants.

[Wurl et al., 2011] investigated the presence of transparent exopolymer particles (TEP), one example for surface active materials. This particles were found in nearly all oceans independent of algae blooms, which is a source for the TEP. This study shows that surface active materials play a role for nearly all air-sea interaction processes as they are nearly everywhere present, especially in coastal areas.
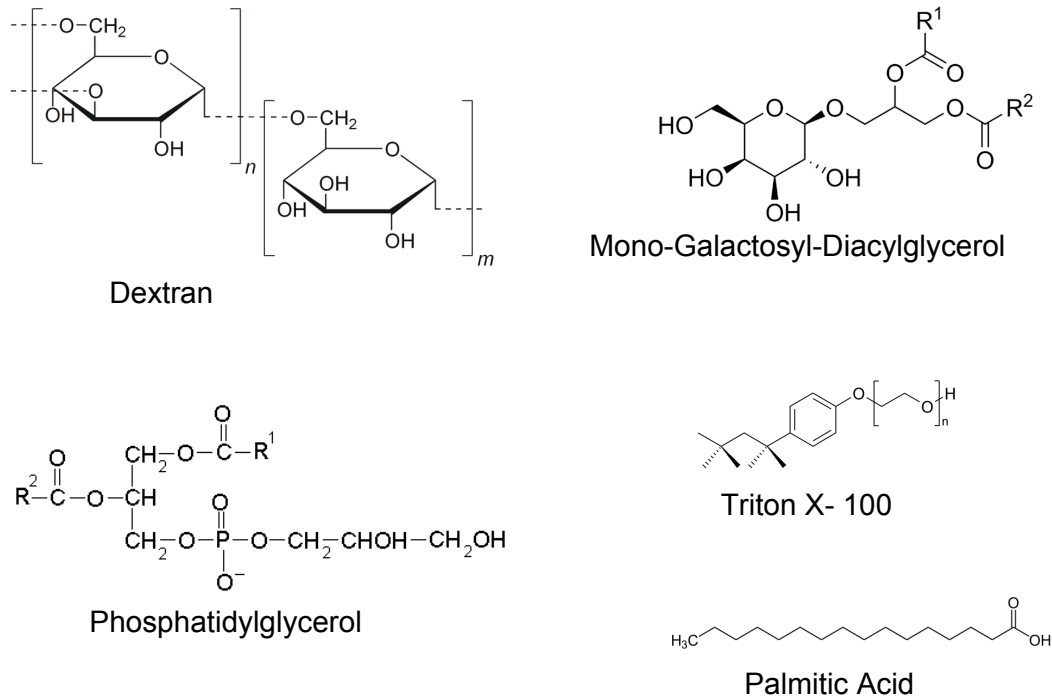
Figure 2.9.: Chemical structure of the surfactants used for the experiments. R^1 and R^2 denotes organic radicals.

In this work, five different surfactants were used to investigate the influence of surfactant on the air sea gas transfer. Figure 2.9 shows their chemical structures. As the air sea gas exchange is sensitive to the concentration of the surfactant [Frew, 1997], measurements were conducted with different concentrations. Two different types of measurements were conducted. To study the physical behaviour of the air-sea gas exchange a synthetic tracer was used:

Triton X-100 is the trivial name of polyethylene glycol p-(1,1,3,3-tetramethylbutyl)-phenyl ether ($C_{14}H_{22}O(C_2H_4O)_n$), where $n = 9.5$ in average. It is a synthetic, non-ionic soluble surfactant. Its molecular mass is $647 \frac{g}{mol}$ and its density is $1.07 \frac{g}{cm^3}$. The viscosity varies in a wide range depending on the temperature, from $0.3 \frac{g}{cm \cdot s}$ at $10°C$ up to $2.7 \frac{g}{cm \cdot s}$ at $125°C$. Micelles start to built at a critical micelle concentration of $0.22 - 0.24 \frac{mol}{l}$.

The second type of experiments tried to reproduce a natural films. Among others, [Tepić et al., 2009], [Gašparović et al., 2007] and [Ćosović and Vojvodić, 1998] investigated the chemical composition of the marine surfactant layer. The main components found are polysaccharides, lipids and fatty acids. Out of these chemical classes a mixture of different surfactants, which consisted of four different types of chemicals were selected for the measurements:

Dextran is a natural occurring, soluble surfactant. It consists of a mixture of polysaccharides, which are made of many glucose molecules with the molecular formula $(C_6H_{10}O_5)_n$. Their molecular weight is between 10.000 and 50.000.000 u. In nature it occurs as a product of the synthesis of sucrose by several bacteria. According to [Tepić et al., 2009] dextran can be used to model the influence of polysaccharid components of the surfactants on the air-sea gas transfer.

Palmitic Acid is a natural, insoluble surfactant with the molecular formular $C_{16}H_{32}O_2$. Palmitic acid is produced during fatty acid synthesis by marine organisms. In this study, it was used to model the chemical class of fatty acids.

Phosphatidylglycerol is a natural and insoluble surfactant. It is a part of the membranes of many bacteria and some algaes and marine organisms. It belongs to the chemical group of phospholipids and was chosen as the model substance for the lipids found in natural surfactants.

Mono-Galactosyl-Diacylglycerol is a natural and insoluble surfactant. It is produced in algaes and is the main lipid components of the various membranes of chloroplasts. It is classified as a glycolipid, meaning a lipid with an attached carbohydrate.

2.3.4. Bubbles

Bubbles have an important influence to the air-sea gas exchange in different ways [Woolf et al., 2007]. Especially at high wind speed breaking waves are creating bubbles. They insert air with the atmospheric gas composite into the water. The containing gases can diffuse through the boundary layer around the bubble and have not to pass the boundary layer at the water surface. Then there are two possibilities, which appear depending on the hydrostatic pressure and therefore the depth and size [Memery and Merlivat, 1985]. First, they can dissolve entirely, so that the volume flux of the dissolved bubbles contributes completely to the gas exchange during invasion. Than the bubble is an additional path for the transport from the air to the water. This path does not contribute to the evasion of gases.

Second, bubbles can rise through the water column and burst at the surface. The rising velocity and therefore the exposure time in the water depends on buoyancy, surfactants and currents. While the bubbles are rising, they add an additional air-water interface. As bubbles have a limited volume, for high soluble gases, the air space is saturated after a very short period of time. Therefore, the interface between the bubble and the surrounding water is more efficient for low soluble gases. At the water surface they burst and eject the gas to the atmosphere. By bursting, they create sea salt aerosols. Following this second pathway, the bubble mediated gas transfer is not directly proportional to the concentration difference between air and water, but depends also on solubility. Increasing solubility leads to an decreasing of the bubble mediated gas transfer. For that reasons it can not be completely included into the classical Schmidt number scaling from one tracer to another, described in section 2.2.7. Furthermore, bubbles have different influence on invasion and evasion measurements due to the described processes.

As a second effect, next to the additional surface, the rising bubbles disrupt the surface microlayer, what enhances the turbulence and therefore the air-sea gas transfer through the water surface.

Bubbles were found to be relevant at wind speed above $u_{10} = 12\,\frac{\text{m}}{\text{s}}$. The bubble injection can be regarded as proportional to the whitecap coverage. The transfer rate of bubble induced gas transfer depends in addition to the described influence of the single bubbles to the distribution and the sizes of the bubbles in plumes. [Woolf, 1997] found for clean bubbles, meaning bubbles, which are not covered with surfactants a parametrisation for the air-sea gas exchange:

$$k_t = k_0 + 850 \cdot W \left[\frac{\text{cm}}{\text{h}} \right] . \tag{2.83}$$

Thereby k_t is the total transfer velocity, k_0 the transfer rate without bubble mediated transfer and W the whitecap coverage. It can be approximated by:

$$W = 3.264 \cdot 10^{-3} u_{10}^{3.41} \tag{2.84}$$

where u_{10} is the wind speed. When surfactants are solved in the water, they cover the bubbles surfaces and influence the diffusion out of and into the bubble. Then the bubble mediated gas transfer is less than described by the parametrisation (equation 2.83), see [Memery and Merlivat, 1985] and [Patro et al., 2002].

2.3.5. Chemical Enhancement

Gases like O_3 or SO_2 underlie chemical reactions when they are solved in water. These reactions increase the concentration difference between air and water. The chemical reaction can be regarded as an additional resistance which is in parallel circuit to the water side gas transfer resistance. CO_2 in water is hydrated to carbon acid. This chemical reaction depends on the pH and does not occur at pH values of less than 5. The process is rather slow and depends on the temperature. A chemical reaction does only enhance the gas transfer, if it is faster than the transport through the boundary layer. Therefore, under most conditions, unless conditions with very low turbulence and high response times, the chemical enhancement for CO_2 can be neglected (see for example [Hoover and Berkshire, 1969] or [Quinn and Otto, 1971]). For averaged oceanic conditions the enhancement was found by [Liss, 1983] to be in the order of 1-2 % and therefore negligible for most applications.

3. Experimental Methods

This chapter introduces different methods to measure air sea gas exchange velocities. It starts with two thermographic techniques to measure heat exchange rates. Section 3.1.1 presents the main method used in this thesis, the active controlled flux method. For this technique different anaylsis methods exit and will be described in chapter 4. In section 3.1.2 the passive thermography is introduced. Afterwards, in section 3.1.3, a mass balance method, which is the mainly used method under laboratory conditions to measure gas transfer rates, is presented. The following section 3.1.4 describes different dual tracer methods, which are also mass balance approaches, used under field conditions. In section 3.1.5 the eddy covariance method, a micro-meteorological approach to measure fluxes is introduced. As all of the methods have advantages and drawbacks a comparison of the different methods follows in section 3.1.6. Last, section 3.2 describes the methods which are used to measure the parameters influencing the air-sea gas transfer, including wave and friction velocity measurements.

3.1. Methods to Determine Transfer Rates

3.1.1. Active Controlled Flux Technique (ACFT)
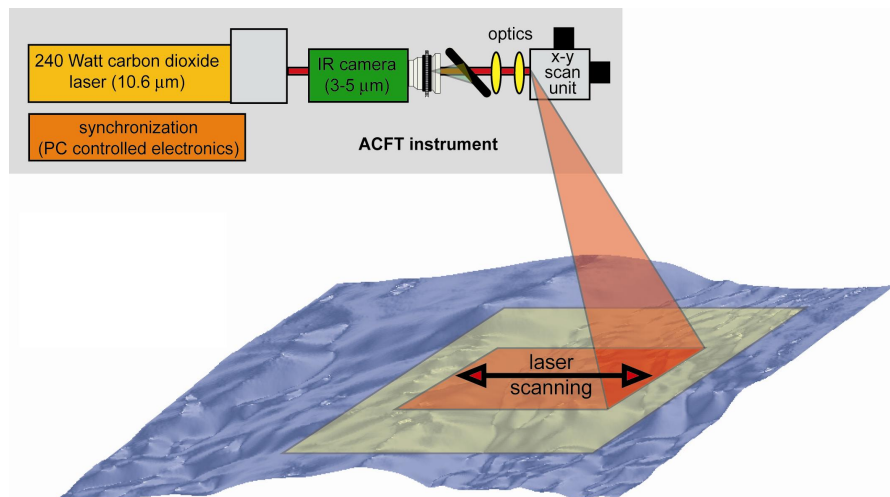
Figure 3.1.: Schematic of the experimental setup for the ACFT measurements - modified after [Schimpf et al., 2011].

The active controlled flux technique (ACFT) was suggested by [Jähne et al., 1989]. The big advantage of this method is the possibility to determine heat transfer velocities under laboratory as well as under field conditions with a high temporal and spatial resolution. Therefore, the principle of the classical measurements (creating a difference in the gas concentration and measure the resulting flux) is inverted: A known flux density is forced to the water surface and the concentration difference Δc over the diffusive boundary layer or the time constant τ is measured. Both parameters can be directly linked to the transfer velocity. If the concentration difference

is measured, the definition of the transfer rate can be used (see equation 2.23: $k = \frac{j}{\Delta c}$). For a measured response time the transfer velocity is $k = \sqrt{\frac{D}{\tau}}$ (see equation 4.10). In practice, heat is used as tracer and then transferred to gas exchange rates by Schmidt number scaling (see section 2.2.7).

Figure 3.1 shows a schematic sketch of the ACFT instrument for heat exchange measurements. A CO_2-laser is used to force a well-known heat flux to the water surface, which is absorbed in the upper few tens of microns. Thereby the air-side transfer resistance is short-circuit and only the water-side part of the transfer velocity can be measured. With the help of a mirror scanning system the laser signal can heat the water surface with different patterns. The red marked area in figure 3.1 illustrates the heated area. When the laser beam hits the water surface, the surface temperature increases until an equilibrium is reached. That means that the energy transported into the bulk corresponds to the energy deployed by the laser irradiation. [Haußecker, 1996] derived that a laser beam with a two dimensional Gaussian shape profile with the width σ, which is focused on the water surface at the position (x_0, y_0) heats the water at the position (x, y, z) by

$$\frac{dT(x, y, z)}{dt} = \frac{P_{\text{tot}}}{2\pi\sigma^2 z_{\text{p}} c_{\text{v}} \rho} \exp\left(\frac{(x - x_0)^2 + (y - y_0)^2}{2\sigma^2}\right) \exp\left(-\frac{z}{z_{\text{p}}}\right) \tag{3.1}$$

where (x, y) are the coordinates spanning the water surface, z is the water depth, P_{tot} is the radiated laser power, c_{v} the specific heat at a constant volume and ρ the water density. The penetration depth is $z_{\text{p}} = 11.5\,\mu\text{m}$ for a laser wavelength of $\lambda = 10.6\,\mu\text{m}$ [Downing and Williams, 1975].

An infrared camera measures the surface temperature with a high spatial and temporal resolution (typically on the order of some $10\,\text{cm}$ with $60 - 400\,\text{Hz}$). In figure 3.1, the yellow marked area of the water surface corresponds to the field of view of the camera. From the infrared images the temperature difference or decay rates are determined. Because of its high solubility of $\alpha = 4000$, heat is an air-side controlled tracer (see section 2.2.6). Using the active thermography technique the laser short-circuits the air side resistance and only the water-side fraction of the transfer resistance is measured. This enables a comparison of the measured heat exchange rates to the ones of water sided controlled gases, like carbon dioxide.

As the active controlled flux technique is based on remote sensing of the water surface, the images can be analysed with respect to different parameters in addition to the transfer velocity. Examples are the determination of the surface drift or an investigation of the turbulent structures.

Heat transfer velocities can be determined from active thermography data by different analysis methods. They are described in detail in chapter 4.

3.1.2. Passive Thermography

Like the ACFT described in section 3.1.1, the passive thermography is a method to determine the transfer velocity of heat, which can be transferred to gas transfer velocities by Schmidt number scaling (see section 2.2.7). It can be used both, under laboratory and under field conditions. It directly uses the definition of the heat transfer velocity given in equation 2.27. Therefore, the net heat flux $\vec{j}$ as well as the temperature difference ΔT have to be determined. For the determination of the temperature difference, images of the water surface, gained with an infrared camera, are used. Assuming the surface renewal model (see section 2.2.8), a theoretical description of

the distribution of the surface temperatures can be predicted:

$$h\left(T_{\mathrm{s}}\right) = \frac{2}{\left(\alpha j_{\mathrm{h}}\right)^2}\left(T_{\mathrm{s}} - T_{\mathrm{b}}\right)\int_{t(T)}^{\infty}\frac{p\left(\tau\right)}{\tau}d\tau \tag{3.2}$$

where T_{s} is the surface temperature, T_{b} the bulk temperature, α is a constant depending on density, specific heat capacity of the water and the diffusion constant of heat in water, j_{h} the heat flux density, τ the renewal time and $p\left(\tau\right)$ the probability distribution of the renewal time. [Garbe et al., 2004] found that this probability distribution is described best by a logarithmic normal distribution of the form:

$$p\left(\tau\right) = \frac{1}{\sqrt{\pi}\sigma\frac{\tau}{t'}}\exp\left(-\frac{\left(\ln\frac{\tau}{t'} - \langle\ln\frac{\tau}{t'}\rangle\right)^2}{\sigma^2}\right), \tag{3.3}$$

where σ^2 is the variance of the logarithm of the scaled random variable for the renewal time τ and t' is a unit scaling factor.

From those assumptions [Garbe et al., 2004] derives a distribution of the surface temperature which is a good description of the measured surface temperature distributions. This distribution includes the bulk temperature as the intersection with the x-axis. The surface temperature corresponds to the expectation value of the distribution. Subsequently the temperature difference $\Delta T = T_{\mathrm{s}} - T_{\mathrm{b}}$ can be calculated. Knowing the total surface fluxes j_{heat} from separate measurements the transfer rate can be determined, using equation 2.27:

$$k_{\mathrm{heat}} = \frac{j}{\rho c_p \Delta T}$$

Different possibilities to determine the heat flux are for example given in [Garbe, 2001].

As it is experimentally difficult to measure the total heat flux at the water surface, according to [Garbe et al., 2004] the heat transfer velocity can be determined by

$$k_{\mathrm{heat}} = \sqrt{\frac{\pi\kappa}{2}}\sqrt{\frac{\dot{T}_{\mathrm{surf}}}{\Delta T}}, \tag{3.4}$$

where $\dot{T}_{\mathrm{surf}} = \frac{d}{dt}T_{\mathrm{surf}}$ is the temporal derivative of the surface temperature and κ the thermal diffusivity. To determine this derivative from the infrared images a motion estimation has to be conducted.

3.1.3. Mass Balance Method

The mass balance method is mainly used under laboratory conditions. For gases with high solubilities invasion measurements are usually conducted (gases are injected into the air space and their transfer into the water is monitored). For gases with low solubilities usually evasion measurements are conducted (gases are given into the water and their transfer into the air is monitored). Therefore, a box model approach is used. In doing so, the air and the water are regarded as well-mixed boxes with the volume V_{a} and V_{w}, respectively. Even if a wind wave tank is nearly gas tight, gases can enter or leave the air and the water volume through leaks. The transfer between the boxes is due to air-water gas transfer. Considering these paths and the mass conservation results in the following differential equations for the change in concentration in the air and water boxes:

$$V_a \dot{c}_a = Ak\left(c_w - \alpha c_a\right) + \dot{V}_a \left(c_a^{in} - c_a\right)$$
$$V_w \dot{c}_w = -Ak\left(c_w - \alpha c_a\right) + \dot{V}_w \left(c_w^{in} - c_w\right)$$

(3.5)

Thereby A is the size of the air water interface, c_a the concentration in the air, c_w the concentration in the water, c_a^{in} the concentration in the air coming in through leaks, c_w^{in} the concentration in the water coming in through the leaks and k the transfer rate from a water-side view.

With these differential equations many different approaches to determine transfer velocities are possible. Two of them will be described in detail. In the more classic way evasion measurements are conducted, where the gas is given into the water at the beginning of the measurements and than degassed to the air space. If the air space is flushed, causing a negligible air concentration and for tracers with small solubilities, equation 3.5 can be simplified by assuming a zero air concentration $c_a = 0$ and a zero concentration in incoming water through leaks c_w^{in} and solved. Then the water sided concentration results as

$$c_w\left(t\right) = c_0 \cdot e^{-\left(k_w \frac{A}{V_w} + \frac{\dot{V}_w}{V_w}\right)t},$$

(3.6)

where the exponent is defined as the inverse of the time constant τ, which can be determined from a fit of the water concentration data:

$$\frac{1}{\tau} = k\frac{A}{V_w} + \frac{\dot{V}_w}{V_w}$$

(3.7)

For the second approach, equations 3.5 can be solved for the transfer rate k. When the air and water concentrations are measured over time and the leak rate is known or measured, transfer rates can be calculated by

$$k = \frac{V_a}{A} \cdot \frac{\lambda_a c_a}{c_w} \cdot \frac{\lambda_a + \frac{\dot{c}_a}{c_a}}{\lambda_a} \cdot \frac{1}{1 - \alpha\frac{c_a}{c_w}}$$

(3.8)

where λ_a is the leak rate, A the water surface and α the solubility. The technique is much more complicated than the classical method, because the absolute values of the air and water concentration and the flush rate have to be measured over time. The advantage of this approach is the low measurement time, allowing the determination of transfer rates within minutes.

Both approaches are explained in detail for example in [Krall, 2013].

3.1.4. Geochemical Tracer Methods

The first experiments conducted under ocean conditions were done with geochemical tracers with a mass balance approach, where the flux can be determined from the water height and the change in concentration with time:

$$j = h_w \dot{c}_w$$

(3.9)

For that purpose, naturally occurring or deliberately added tracers can be used. Differences in the concentration of a natural tracer can be produced for example by biological activity or by changes in temperature, causing changes in solubility. Deliberate tracers have to be injected into the well mixed water bulk. The integration time for this method is on the order of days with

a spatial resolution of a few tens of kilometres. As environmental conditions, like for example wind speed, temperature or film coverage, can change substantially in this time, measured transfer rates are often averaged over different conditions.

Equation 3.9 includes no sinks or sources. In field measurements, the tracer concentration decreases not only because of gas exchange processes, but also because of diffusion and ocean currents. To take this into account dual tracer methods are often used. Thereby, two different tracers are regarded simultaneously. To correct for the dilution effect, the ratio of the transfer rates has to be measured.

The mostly used natural tracer is ^{222}Rn. It is a radioactive source, which arises from the decay of ^{229}Ra. In the absence of gas exchange both elements are in equilibrium, coupled by the decay constant λ. When radon is exchanged, the flux can be determined from the deficit I of ^{222}Rn relative to ^{229}Ra and the decay constant λ, [Roether and Kromer, 1984]:

$$j_{^{222}\text{Rn}} = \lambda I \tag{3.10}$$

The integration time for this tracers is approximately four days.

For deliberate tracers SF$_6$ and ^{3}He are inserted mostly simultaneously. They differ in their Schmidt numbers by a factor of about 8. Therefore, the ratio of the gases in the water body will change with time, as ^3He will have a three times larger transfer rate. The effects of diffusion will not change the ratio. According to [Wanninkhof et al., 1993] the transfer rate for ^3He can then be described as:

$$k\left(^3\text{He}\right) = \frac{-h}{\Delta t} \cdot \Delta \left[\ln\left(\frac{[^3\text{He}]}{[\text{SF}_6]}\right)\right] \cdot \left[1 - \left(\frac{Sc\left(^3\text{He}\right)}{Sc\left(\text{SF}_6\right)}\right)^{-\frac{1}{2}}\right]^{-1} \tag{3.11}$$

where the Δ term is the change in ratio over the time Δt.

3.1.5. Eddy Correlation Method

The eddy correlation method, which is also called eddy covariance method is model independent as it needs no assumptions about the turbulence. It is only usable for field measurements. It uses direct flux measurements, which are standard measurements in micro-meteorology. The flux is regarded as constant in the surface boundary layer, which has an extent of approximately $20 - 50$ m for unstable stratifications [Aubinet et al., 2012]. The flux of a gas can be described with the help of the Reynolds decomposition (see section 2.2.5)

$$j = \langle cw \rangle = \langle \left(\bar{c} + c'\right)\left(\bar{w} + w'\right) \rangle, \tag{3.12}$$

where c is the concentration of the tracer, w is the vertical velocity of the air, the fluctuations of both are signed with $'$ and the temporal mean with $\langle \rangle$. Assuming a vanishing mean vertical velocity and assuming that the average of the fluctuation of each component is zero, this can be transcribed to

$$j = \langle c'w' \rangle. \tag{3.13}$$

To use the eddy covariance technique these fluxes are measured from gas concentrations in the air and the vertical component of the wind speed with either open or closed path gas analysing systems. Both systems have advantages and drawbacks. Closed path systems convince with a known temperature and density in the chamber. But the sampling time is rather long compared to the open path systems, so the high frequency variations can get lost. The open path systems

are fast, and the fluctuations due to temperature and density changes can be corrected. But they are prone to problems due to rain and sea salt deposits. Furthermore for both systems corrections for the humidity fluctuations are necessary [Sahlee et al., 2011]. The velocities are measured by sonic anemometers.

Additional to the measured fluxes, the difference of the partial pressure of the tracer in air and water has to be determined. Then the transfer velocity can be determined like described in section 2.2.4 by the use of

$$k = \frac{j}{K_\alpha \Delta p},$$

(3.14)

where K_α is the aqueous solubility with the unit of concentration per pressure and Δp is the difference in the partial pressure of the tracer in air and water.

This method is difficult to apply, because of the small fluctuations in the fluxes with rather small signal to noise ratios. Furthermore, the movement of the platform or ship must be corrected. Furthermore, corrections for air density and compression, evaporation and water vapour diffusion as well as the consideration of sinks and sources, additional to the air sea interaction are necessary. Nevertheless, eddy covariance methods are widely used for both, air sided controlled tracers, like heat or water side controlled tracers like CO_2 or DMS. This method delivers transfer rates with a high temporal resolution on the order of 20 - 30 minutes and a spatial resolution on the order of some kilometres. A detailed description of the method is described for example in [Kowalski and Serrano-Ortiz, 2007] while a description of the technical requirements and the necessary corrections is given for example in [Aubinet et al., 2012].

### 3.1.6. Comparison of the Different Methods
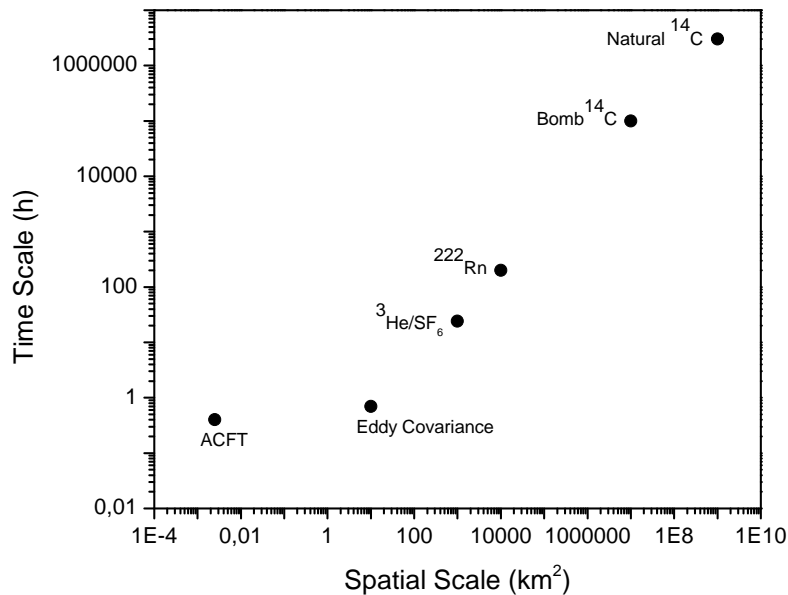
Figure 3.2.: Comparison of the spatial and temporal resolution of different methods - modified after [Garbe et al., 2014].

One of the major differences of the different measurement methods are the spatial and temporal time scales. Figure 3.2 shows a comparison of the different methods, which are applicable for field measurements.

The mass balance method is the most direct way to determine gas transfer velocities. The time scales are large (in the order of hours). For that reason, it is applicable in laboratory measurements, where the conditions can be hold stable over several hours. For a wide range of investigations, this is a valuable technique. Especially the physical understanding of the exchange processes as well as the knowledge of the influence of different parameters, like wind speed, wave statistics, fetch or surfactants on the air sea-gas exchange, can be improved by using mass balance methods.

Under field conditions, a change in concentration is not only due to gas transfer, but also due to other effects like currents or by production or depletion. Therefore, the mass balance method has to be extended to the dual tracer method. With that method, these additional processes are taken into account. However, the long integration time is still a problem as influences like wind speed, rain or surface coverage with surfactants can vary during that time.

Mass balance methods can be used for a wide range of different tracers. In laboratory measurements all kinds of gases with different diffusion constants and solubilities can be used, depending on the available gas measurements techniques. For field measurements with deliberate tracers, environment protection issues have to be considered.

A faster way to determine transfer velocities for several gases is the eddy covariance method. It has high technical requirements, as small differences in the fluxes have to be resolved. Furthermore, corrections for the movement of the platforms or ships, where the measurements are conducted, have to be applied. Additional corrections for the temperature and for water vapour are necessary. Nevertheless, they show good results with a high temporal resolution and are an important tool for investigations under open ocean conditions. However it can not be used in laboratories, so a comparison of laboratory and field studies is not possible with that method.

Passive thermography allows to determine transfer velocities with a high spatial and temporal resolution. The technical implementation is simple as only a calibrated infrared camera is necessary. The technique works very reliably in laboratories. In field measurements it depends on the weather conditions. Given that a cool skin layer appears, it works quite well under clear sky or completely cloud covered conditions. The temperature of the clear sky is about $50°C$ up to $65°C$ less than the air temperature, which can result in an offset of up to $0.7°C$ in the measured temperature due to reflections of the sky. This constant offset does not influence the measurement as only the temperature difference has to be known. But under conditions with unevenly distributed clouds, reflections of the sky adulterate the measured temperature distributions. Moreover, direct sun irradiation disturbs the measurements when sunlight is reflected into the infrared camera. For the analysis with passive thermography the assumption of a surface renewal model with a logarithmic normal temperature distribution is necessary. Additionally the passive thermography measures the transfer rates only for heat, which is an-air side controlled tracer. As the described data analysis does only determine the water-side part of the transfer velocity, a Schmidt number scaling to water-side controlled tracers like CO_2 is possible if the Schmidt number exponent is known.

The active controlled flux technique offers both the possibility to measure under laboratory and under field conditions as well as a high spatial and temporal resolution. It does not depend on further flux measurements and works independently of the weather conditions, except for

direct sun irradiation. ACFT measurements, as all thermographic methods, do not include the contribution of bubble mediated gas transfer. For the determination of the heat transfer velocity this effect is not important. Because of the high solubility of heat in water $\alpha = 4000$ the bubbles are saturated very fast and do not play any role for the gas transfer. But as transfer rates for low soluble gases like CO_2 can be increased to due to bubbles, the comparison to measurements of heat and gas transfer could be distorted. Nevertheless, if simultaneous gas transfer measurements are available, this effect can be used to determine the contribution of the bubble mediated gas transfer to the total gas transfer velocity.

Furthermore, heat is the only tracer which can be used by the active controlled flux technique (as well as with the passive thermography). As only the water-side part of the transfer velocity is measured, a Schmidt number scaling is possible (see section 2.2.7). Nevertheless, it is still under discussion, if a Schmidt number scaling from heat to CO_2 leads to right transfer velocities, because of the big differences in Schmidt number and solubility.

3.2. Methods to Determine the Parameters Influencing the Air-Sea Gas Exchange

3.2.1. Wave Measurements

To find the best parameter to characterise air-sea gas transfer, measurements of different wave parameters are essential. For some of the measurements conducted in the framework of this thesis, simultaneous measurements of the mean squared slope are available. This chapter will present two methods, which were used by co-workers to determine the mean squared slope values for the measurements described in this thesis.

High Speed Imaging Slope Gauge

The high speed imaging slope gauge (ISG) is an instrument to measure the two dimensional slope of the water surface. The measurement principle is described in detail in [Rocholz, 2008] and the used set-up in [Kiefhaber et al., 2014].

It is only used for laboratory measurements, as a light source is installed below the flume of the wind-wave tank. A camera is observing the refraction of light rays at the water surface. The light source, installed below the flume, has an intensity gradient. From the measurement of the intensity of the refracted rays, it is possible to determine their origin on the light source.The slope of the water surface is then computed from the geometry of the setup.

This instrument enables the measurement of the slopes in two directions with a high spatial resolution. It delivers not only the mean squared slope, which is used in this thesis, but the whole three dimensional wavenumber-frequency spectrum and allows to reconstruct the water surface.

Reflective Stereo Slope Gauge

The Reflective Stereo Slope Gauge (RSSG) was developed and constructed by [Kiefhaber, 2010] and extended by [Kiefhaber, 2014] to measure the mean squared slope and the water height (as deviation to a reference height). It combines a reflective statistical slope measurement method, which can be used both in laboratories and in the field, with a stereo setup.

The principle of the measurements of the slope of the water surface is shown in figure 3.4. The camera measures the reflected signal of the flashed light source. The camera can only see a reflection of the light, when the wave slope is in a small range around a specific angle. This
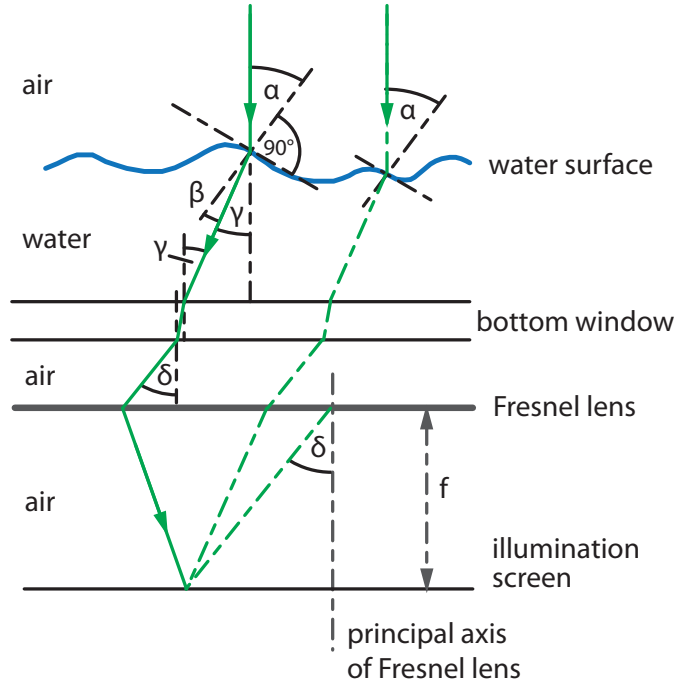
Figure 3.3.: Principle of the measurements with the ISG - image taken from [Kiefhaber et al., 2014].

angle depends on the pixel position in the image. The frequency with which reflections occur at specific image positions is linked to the probability with which a certain surface slope occurs. Thus, it is possible to measure the slope probability density function. Other statistical wave parameters, like the mean squared slope, can be determined from this probability distribution.

A more detailed description of the measurement principle is given in [Kiefhaber et al., 2011].

3.2.2. Friction Velocity

Another important parameter for the comparison of different measurements is the friction velocity. Here only the measuring method used for the determination of the friction velocity in the Heidelberg Aeolotron is described.

As it is a circular wind wave facility, a momentum balance method can be used. The velocity of the water body is determined by the momentum input $\frac{dp}{dt}$ from the wind stress F_{wind} and by the friction at the walls F_{friction}:

$$\frac{dp}{dt} = F_{\text{wind}} - \sum F_{\text{friction}} \tag{3.15}$$

Under the assumption, that the water velocity is constant with depth follows [Bopp, 2011]:

$$V_{\text{w}} \rho_{\text{w}} \frac{\partial u_{\text{w}}}{\partial t} = A \rho_{\text{w}} u_{*\text{ws}}^2 - V_{\text{w}} \rho_{\text{w}} K u_{\text{w}}^2 \tag{3.16}$$

with V_{w} the water volume, A the water surface, ρ_{w} the density of water, u_{w} the water velocity, $u_{*\text{ws}}$ the friction velocity at the water surface, induced by the wind and K the constant of friction of the walls and the build-in instruments. An equilibrium, where the momentum input by the wind equals the loss due to friction at the walls, is reached at a water velocity of:

$$u_{*\text{ws}} = \sqrt{K \frac{V_{\text{w}}}{A}} u_{\text{w}}. \tag{3.17}$$
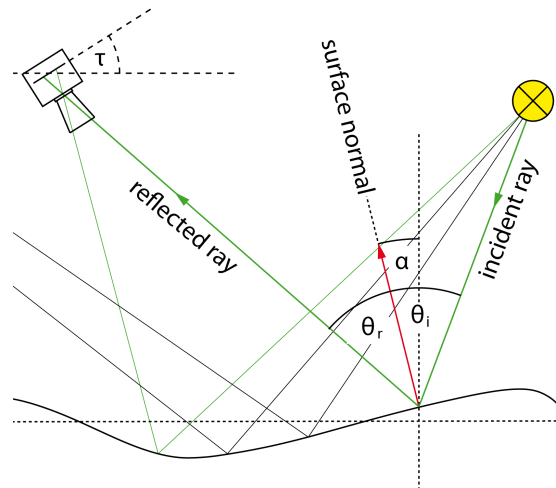
Figure 3.4.: Principle of the slope measurements with the RSSG - image taken from [Kiefhaber et al., 2011].

That means, with a known geometry of the flume only the constant of friction K has to be ascertained to determine the friction velocity from the water velocity. For that reason the water velocity is monitored when the wind is switched on. The wind induced momentum actuates the water body. The time dependent behaviour of the velocity can be described by [Bopp, 2014]:

$$u_{\mathrm{w}}\left(t\right) = u_\infty \cdot \tanh\left(u_\infty K\left(t - t_0\right)\right) \tag{3.18}$$

where u_∞ is the velocity of the water body, when the equilibrium is reached. By fitting 3.18 to the measured data, the constant of friction K can be determined as a fitparameter.

4. Analysis Methods

The ACFT instrument can be used to force fluxes with different shapes (points, lines, area) and different time behaviours (continuous on or periodically varying) to the water surface. There are different possible analysis methods, requiring different stimulations.
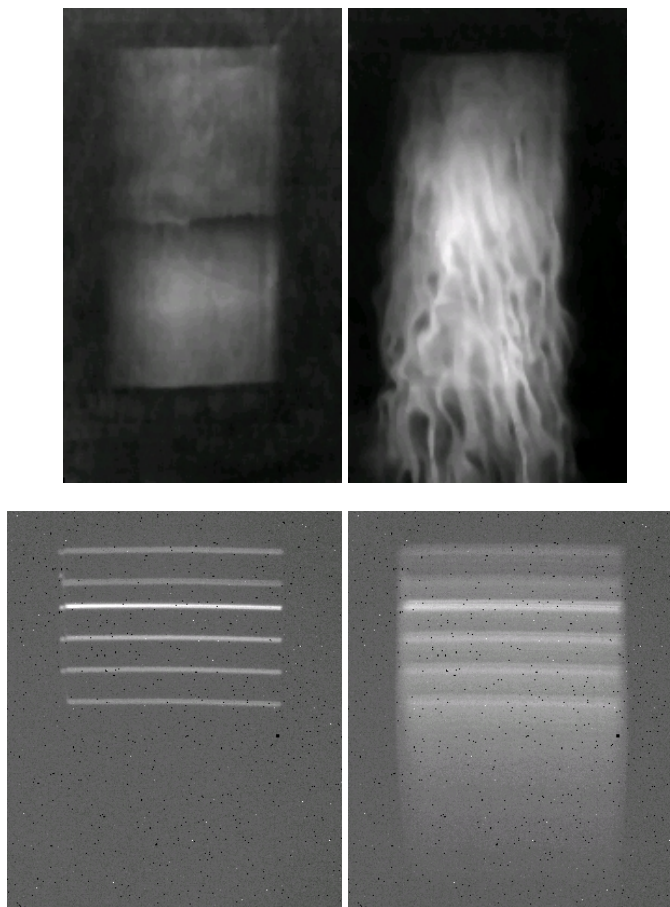
Figure 4.1.: Used laser stimulations: upper images: heated area after 0.15 s and after 5 s of heating, lower images: heated lines after 0.3 s and after 5 s of heating.

Figure 4.1 shows two typical laser stimulations. In the upper part of the images a heated area, created by scanning a line, is shown, on the left side 1.5 s after the begin of the heating phase. On the right-hand side the same sequence is shown after 5 s when the temperature equilibrium is reached. The lower images show the stimulation in the form of lines. The left image shows the sequence after 0.3 s of heating, when each line was heated once. The right part shows the same sequence after 5 s when the surface drift has already smeared the heated lines. The direction of the wind and therefore also the direction of the surface drift is from top to bottom.

4.1. Fourier Analysis: Amplitude Damping

4.1.1. Fourier Analysis

For the amplitude damping method, the laser beam is widened to a line. The line is scanned over the water surface to create a constant heated area. The laser is switched on and off periodically with varying frequencies. Then the same analysis as in signal theory is used, regarding the system response at different frequencies. For frequencies, which are small compared to the decay time, $\omega\tau \ll 1$, the surface temperature reaches the equilibrium state. For higher frequencies the boundary layer acts as a low pass filter, the amplitude is damped and the measured amplitude is proportional to $\frac{1}{\sqrt{\omega}}$. The intersection of a line through this damping part with a line along the undamped amplitude at low frequencies, gives the frequency where $\omega_*\tau = 1$.
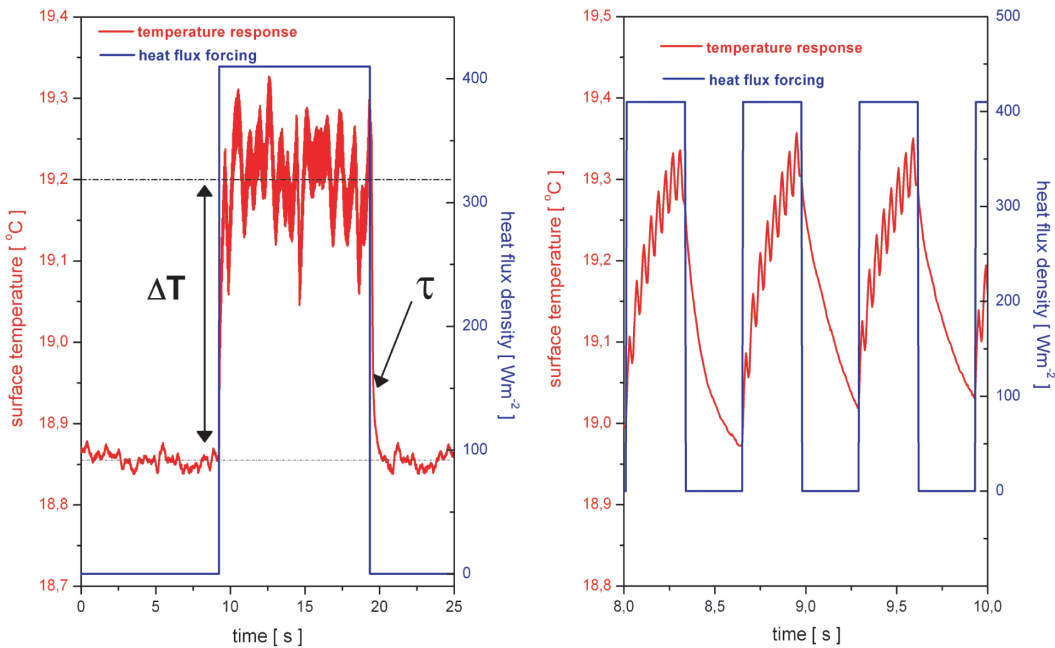

Figure 4.2.: Laser forcing with two different laser frequencies and temperature response of the water surface - taken from [Schimpf et al., 2011]

Figure 4.2 shows the laser forcing and the resulting temperature response for one exemplary measurement conducted on *FS Alkor* (see 6.1.2) for two different laser on/off frequencies. At a forcing frequency of $0.488\,\text{Hz}$ the equilibrium temperature can be reached and the temperature difference ΔT is measured (left part of figure 4.2). At the forcing frequency of $1.5625\,\text{Hz}$ the laser is already switched off before the equilibrium is reached, the measured amplitude is damped (right part of figure 4.2). It is clearly recognizable in the figure, that the signal is superimposed by the scanner signal.

The created laser signal is a superposition of the laser on/off signal and the scanning signal. Using linear signal theory, this signal is analysed by a Fourier transformation in temporal direction. Because of the discrete imaging only a discrete Fourier transformation can be applied. Here the continuous functions will be shown for simplification. Nevertheless, the discrete signals behave nearly identical.

Using a scanner to heat an area of the water surface means, that each pixel is heated only for short moments, when the scanner is passing by. This can be formulated as a Dirac comb, recurring with the scanner frequency ν_s. In the Fourier space the Dirac comb for the scanner

signal results in another Dirac comb:

$$S\left(t\right) = \sum_{n=-\infty}^{\infty} \delta\left(t - n\frac{1}{\nu_\mathrm{s}}\right) \tag{4.1}$$

$$\widehat{S} = \sum_{u=-\infty}^{\infty} \delta\left(\omega - u\omega_\mathrm{s}\right) \tag{4.2}$$

The overlayed laser signal corresponds to a square wave signal with the frequency ν_L. Conducting the Fourier transformation, the square wave signal results in a sinc function:

$$L\left(t\right) = \begin{cases} 1 & \text{for } \nu_\mathrm{L}t < \frac{1}{2} \\ 0 & \text{for } \nu_\mathrm{L}t > \frac{1}{2} \end{cases} \tag{4.3}$$

$$\widehat{L}\left(\omega\right) = \frac{\sin\left(\frac{\omega}{2\nu_\mathrm{L}}\right)}{\frac{\omega}{2\nu_\mathrm{L}}} \tag{4.4}$$

The product of both signals in time space results in a convolution of their Fourier Transform in frequency domain. Thereby the Fourier transform has an entry in the fundamental tone as well as in the uneven overtones.

To determine the amplitude damping, an artificially generated signal is used, which equals zero, when the laser is off and one when the laser is on. It is also analysed in the same way by a discrete Fourier transformation. The amplitude damping is given by the ratio of the measured and the generated signal. It is one for low frequencies and decreases with increasing frequency.
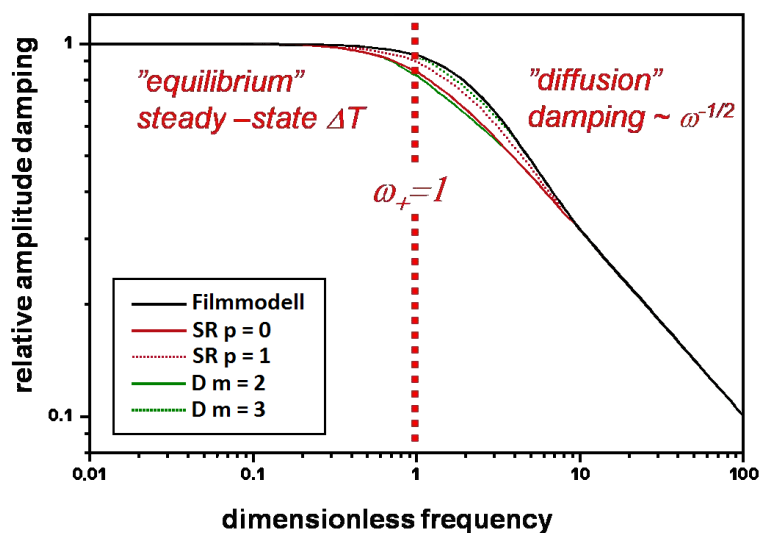

Figure 4.3.: Theoretical Amplitude Damping

This behaviour is shown in 4.3 for different gas transfer models. All models contain the constant part for low frequencies and the same decrease with $\omega^{-\frac{1}{2}}$ for high frequencies. They differ in the transition area. The difference between the different models is quite small, so a distinction between the different models with help of the measurements might be very difficult due to the insufficient accuracy of the currently available measurements.

This analysis is done for each pixel of the heated area. Because of the surface current cold water is flowing into the heated area. Therefore, the temperature at the upwind side of the heated

area is lowered, the decay time τ is underestimated and the transfer velocity overestimated. After a certain distance, the inflowing water is already fully heated and an equilibrium state is reached. Therefore, for the data analysis only a small part at the downwind side is used. It is the same patch like in the ΔT analysis and is depicted in figure 4.6. The determination of this patch is described in section 4.2. Perpendicular to the wind speed, the signal is regarded as constant and is therefore averaged in that direction. To avoid diffusion effects, the edges of the heated area are not considered in the average. Besides that, the analysis can be done for all present signals, which are the laser on off frequencies and the scanner frequency aa well as their harmonics.

4.1.2. Correction for the Penetration Depth of the Infrared Camera

Incident radiation Φ is not completely absorbed at the water surface, but decreases proportional to the water depth z:

$$d\Phi = -\beta\left(\lambda\right)\Phi dz. \tag{4.5}$$

The wave length dependent constant of proportionality $\beta\left(\lambda\right)$ is inversely proportional to the penetration depth $z_{\mathrm{p}} = \frac{1}{\beta}$ (see also 2.1.3). In this layer all incident irradiation is absorbed. Analogously, the radiation emitted from the water surface is created in that layer.

Because of this effect, the infrared camera does not see the temperature direct at the water surface, but integrated over the penetration depth. Therefore, the measured temperatures T_{m} have to be corrected for the penetration depth like proposed in [Popp, 2006].
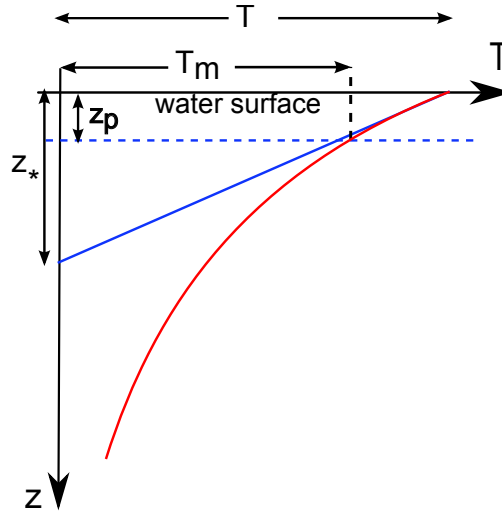

Figure 4.4.: Temperature profile with depth - image modified after [Popp, 2006]

The penetration depth z_{p} is in the order of $2 - 90\,\mu\mathrm{m}$ and therefore smaller than the boundary layer z_*, which is in the order of $300\,\mu\mathrm{m}$ till $1\,\mathrm{mm}$. As a result, the temperature profile with depth is linear for the penetration depth of the infrared camera. Figure 4.4 shows a generic temperature profile with depth (red), boundary layer thickness and penetration depth of the infrared camera as well as the actual and measured temperature. According to the intercept theorem one obtains:

$$\frac{T - T_{\mathrm{m}}}{z_{\mathrm{p}}} = \frac{T}{z_*} \quad \Rightarrow \quad T = T_{\mathrm{m}}\frac{z_*}{z_* - z_{\mathrm{p}}} \tag{4.6}$$

where D is the diffusion constant of heat in water. At a water temperature of 20°C the diffusion constant is given as $D = 0.0014\,\frac{\mathrm{cm}^2}{\mathrm{s}}$ ([Jähne, 2009]).

Rearranging equation 4.6 and using the definition of the boundary layer thickness, given in equation 2.29 yields a corrected temperature:

$$T = T_m \left(\frac{1}{1 - \sqrt{\frac{z_p^2}{D}} \sqrt{\omega}} \right) \tag{4.7}$$

For $z_* \gg z_p$ an approximation can be made:

$$T = T_m \left(1 + \sqrt{\frac{z_p^2}{D}} \sqrt{\omega} \right) \tag{4.8}$$

With the correction factor gained from this equation all amplitudes calculated with the Fourier transformation have to be corrected.
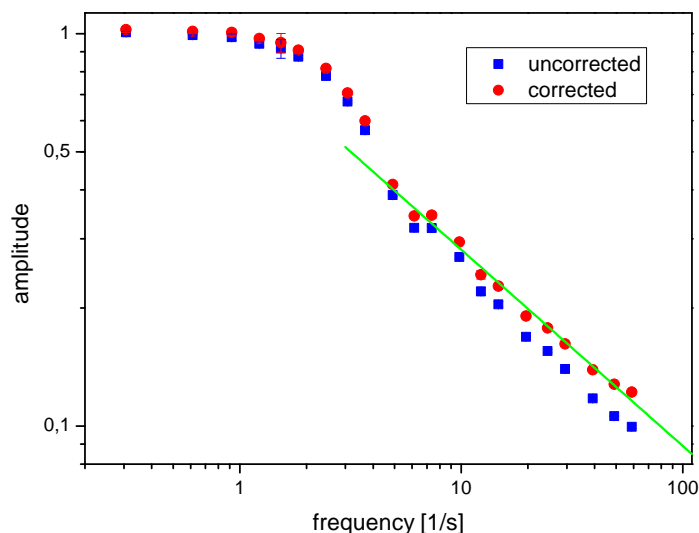
Figure 4.5.: Influence of the correction for the penetration depth at higher wind speeds. The green line shows the expected behaviour $T \propto \omega^{-\frac{1}{2}}$.

Figure 4.5 shows the behaviour of the amplitude with frequency for one exemplary measurement conducted in the Heidelberg Aeolotron. For low frequencies the correction of the penetration depth of the infrared camera yields only to a very small change in the measured amplitude. For higher frequencies the amplitudes corrected for the penetration depth (red) differ from the uncorrected values. The corrected amplitudes show the expected behaviour and are proportional to $\omega^{-\frac{1}{2}}$ which is shown with the green line.

4.1.3. Decay Time

The decay time can be determined from the point of intersection of the linear fit to the constant amplitudes at low frequencies and a second linear fit to the decreasing amplitudes at high frequencies. Alternatively, it is possible to determine a formulation for the behaviour of the amplitude with frequency with the help of the different gas exchange models. As shown in section

4.1.1 the differences between the different models are smaller than the measurement accuracy. Therefore, the formulation for the surface renewal model can be used, as it is the only model allowing to determine the formulation analytically (see [Jähne et al., 1989]):

$$c\left(\omega\right) = c_0 \left(1 + \left(\omega\tau\right)^2\right)^{-\frac{1}{4}} \tag{4.9}$$

Fitting this curve to the measured amplitudes results directly in the response time τ.

4.1.4. Transfer Rates

The transfer velocity can be determined from the response time τ by ([Jähne et al., 1987]):

$$k_{\text{heat}} = \sqrt{\frac{D}{\tau}} \tag{4.10}$$

where D is the diffusion constant of heat in water. It can be assumed as $D = 0.0014\,\frac{\text{cm}^2}{\text{s}}$ ([Jähne, 2009]).

4.1.5. Flux Density

For the determination of the transfer velocity with help of the amplitude damping model it is not necessary to know the exact flux density imprinted to the water surface. Instead it is possible to determine the absolute value of the laser flux density $|\vec{j}|$ from the measured amplitudes at high frequencies $|\tilde{a}|$ ([Jähne et al., 1989]):

$$|\tilde{a}| = \frac{|\vec{j}|}{\left(D\omega\right)^{\frac{1}{2}}} \tag{4.11}$$

## 4.2. Temperature Difference Method

4.2.1. Transfer Rates

The temperature difference method uses the basic idea of the controlled flux technique. Equation 2.27 describes the relation of the transfer velocity k_{heat} with a heat flux density j and the temperature difference ΔT:

$$k_{\text{heat}} = \frac{j}{\rho c_{\text{p}} \Delta T}$$

Using the ACFT the heat flux density can be determined from the total output power of the laser p_{tot} and the size of the heated area A:

$$\dot{j}_{\text{h}} = \frac{p_{\text{tot}}}{A} \tag{4.12}$$

The size of the heated area is determined from a size calibration measurement. The temperature difference, created by this heat flux, corresponds to the temperature difference between the heated area and the surrounding of the heated area. This method leads to high requirements for the camera calibration, which are necessary to correct spatial inhomogeneities of the detectors. To avoid this problem, the laser can be switched on and off with a very low frequency, guaranteeing that an equilibrium temperature can be reached. Then the temperature difference can be determined locally for every pixel by taking the difference between the temperature when the laser is on and the temperature without laser irradiation.

4.2.2. Determination of the Analysed Patch
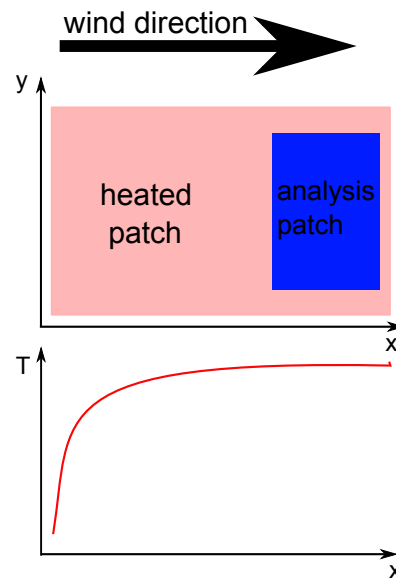
Figure 4.6.: Chosen area for the analysis in the heated patch and generic temperature profile at the same positions

The surface drift carries cold water into the heated area and decreases the measured temperature. After some distance, the water has already undergone sufficient heating to come into an equilibrium state in which temperature does not change along drift direction any more. The temperature reaches a spatial equilibrium. Furthermore, on the edges of the heated area diffusion effects lower the temperature. For that reasons an area is heated by widening the laser beam to a line perpendicular to the wind direction, which is scanned over the water surface. Only a small patch at the downwind side of the heated area is used for the ΔT analysis. Figure 4.6 shows the location of this patch in the heated area and a temperature profile for the same positions.

For practical use as a first step the position of the heated area in the infrared image has to be detected. Therefore, a Fourier transformation in temporal direction is performed for every pixel. Then all pixels with non-zero entries at the laser on/off frequency and the scanner frequency are detected. As a second step the patch, where the thermal equilibrium is reached, has to be detected within this heated area. It is detected with the help of the temperature profiles, as shown in figure 4.6. Therefore, the spatial derivative of these profiles is calculated. The part where the derivative is zero accords to the patch, where the analysis can be done.

4.3. Decay Curves

For the analysis with help of the decay curves a line signal is used, which can be either created by scanning or by widening. When more than one line is created only the last line is used for data evaluation. The laser line moves with the surface drift and has to be tracked first. The tracked signal decreases due to the vertical heat transport into the bulk. The signal can be averaged over the laser line perpendicular to direction of the wind speed. By choosing a section in the middle of the heated line for averaging, diffusion effects in that direction can be neglected. Nevertheless, diffusion in wind direction is still present.

[Haußecker, 1996] showed with a numerical simulation for the surface renewal model, that the decay can be described and fitted with

$$T\left(t\right) = T_0 \frac{h}{\sqrt{h^2 + 4D\left(t - t_0\right)}} \exp\left(-\frac{t - t_0}{\tau}\right) \tag{4.13}$$

where t_0 is the time, when the laser is switched off and h is the penetration depth of the laser. Thereby, according to [Reinelt, 1994], the temperature distribution in the boundary layer of a surface element leaving the heated patch is assumed to be Gaussian.

To gain equation 4.13 the penetration depth of the system is assumed to not influence the shape of the laser signal. Furthermore, the change in temperature with time is assumed to be the same in all depths because of the linearity of the transport equation. Moreover, constant surface fluxes should not influence the temperature decrease.

The response time τ of the system can be determined by a fitting to the measured and tracked data.

Like described in 4.1.4 the transfer velocity can be determined from the response time with

$$k_{\text{heat}} = \sqrt{\frac{D}{\tau}} \tag{4.14}$$

where D is again the diffusion constant of heat in water. It can be assumed as $D = 0.0014\,\frac{\text{cm}^2}{\text{s}}$ ([Jähne, 2009]).

4.4. Fourier Analysis: Spatial Behaviour

A theoretical investigation of the spatio-temporal system response of an active thermography setup with different laser pattern was conducted by [Haltebourg, 2014]. The results used here are based on a surface renewal model. It assumes that the laser is homogeneous in the direction perpendicular to the wind speed direction. That can be realized by scanning a laser point with a frequency, which is higher than the frame rate of the infrared camera. To describe the parallel lines in wind direction, the laser is assumed to scan over the water surface with a constant velocity and to be only switched on, when the positions of the lines are reached.

In the Fourier space there is a linear spatial decrease of both, the amplitude and the phase after each of the heated lines due to the combination of horizontal surface drift and vertical heat transport. Two parameters β_1 and β_2, describing the slopes of these quantities are defined. β_1 is linked to the behaviour of the phase Φ:

$$\beta_1 = -\frac{\partial \Phi}{\partial x} \tag{4.15}$$

β_2 is directly linked to the slope of the amplitude $\Psi = |\ln\left(c\right)|$:

$$\beta_2 = \frac{\partial \Psi}{\partial x} \tag{4.16}$$

As the solution for the response time τ is rather long the following abbreviations have been defined:

$$B = \omega - \beta_1 u_0 + 2\beta_1 \beta_2 D \tag{4.17}$$

$$F = \frac{1}{2} \frac{\beta_1^2 - \beta_2^2}{\beta_1 \beta_2} \tag{4.18}$$

$$W = B^2 \left(1 + F^2\right) \tag{4.19}$$

$$\phi = \begin{cases} \arctan\left(F^{-1}\right) & \text{for } F \geq 0 \\ -\pi + \arctan\left(F^{-1}\right) & \text{for } F < 0 \end{cases} \tag{4.20}$$

$$Q = \begin{cases} -2\cos\left(\frac{\phi}{3}\right) & \text{for } F \geq 0 \\ -2\cos\left(\frac{\phi}{3} + \frac{2}{3}\pi\right) & \text{for } F < 0 \end{cases} \tag{4.21}$$

All these equations do only need the two measurable parameters for the slopes of phase and amplitude β_1 and β_2 and the velocity of the surface drift u_0. D is the diffusion constant of heat in water. With the help of these abbreviations the response time can be written as:

$$\frac{1}{\tau} = \sqrt{W}Q + (\omega - \beta_1 u_0) F - \beta_2 u_0 \tag{4.22}$$
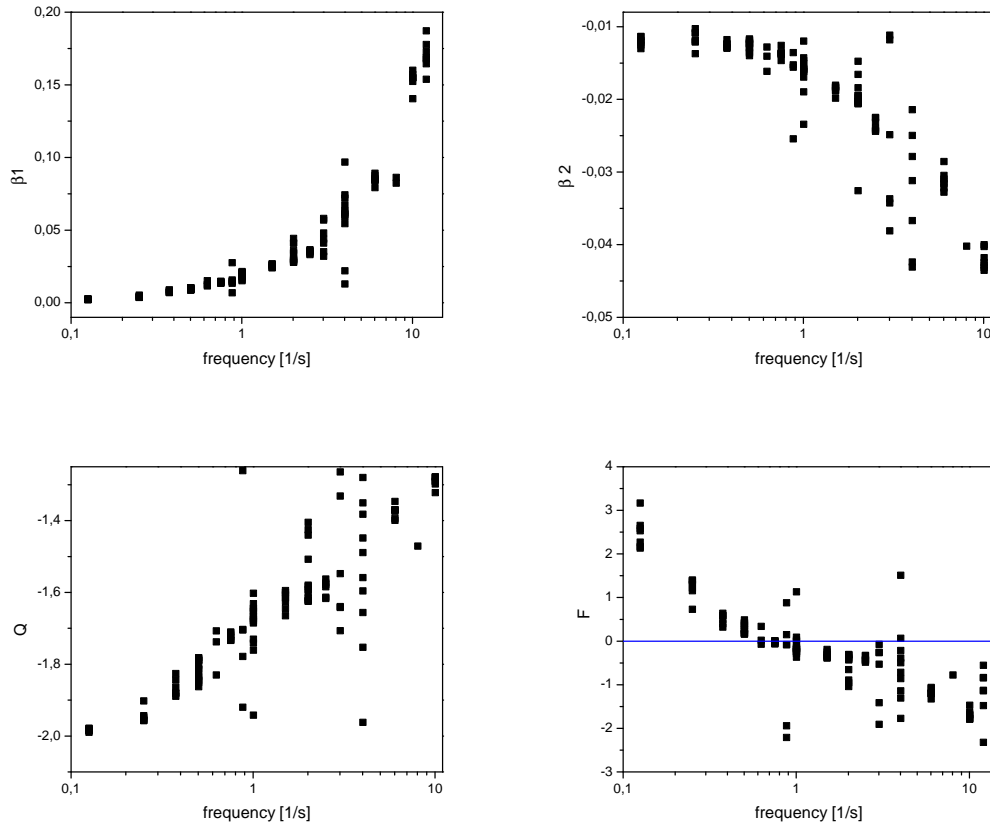
Figure 4.7.: Typical behaviour of the spatial slopes of phase β_1 and amplitude β_2 with frequency and the deduced parameters Q and F.

Figure 4.7 shows the behaviour of the slopes for phase β_1 and amplitude β_2 in respect to the frequency for one exemplary measurement conducted in Marseille in 2012. The resulting decay time can be determined for each of these points, which correspond to different laser on/off frequencies and their overtones, and will not depend on the frequency any more. If the velocity of the surface drift can not be determined separately it is nevertheless possible to approximately

determine the transfer rates from the behaviour of the parameters. The parameter F intersects the x-axis (which is shown as a blue line in figure 4.7) at the frequency which is the inverse of the response time of the system: $\omega \approx \frac{1}{\tau}$. Then the transfer rate can be determined from the response time τ, as described in section 4.1.4:

$$k_{\text{heat}} = \sqrt{\frac{D}{\tau}}. \tag{4.23}$$

4.5. Inconsistencies of Former Results

A lot of different thermographic measurements to determine heat transfer rates were conducted with contradictory results. They were conducted under different conditions and analysed with different methods. The following compilation does not claim to be exhaustive, but shows a selection, presenting the different findings.

Studies, indicating that heat can be used as a proxy tracer for the transfer of low soluble gases, were conducted by different authors: [Jähne et al., 1989] and [Libner, 1987] used the amplitude damping method (see section 4.1) to gain heat transfer rates under laboratory conditions. Therefore, a large area was heated by an infrared heating element. The scaled heat transfer rates are in good comparison with measured gas transfer rates, determined in the same facility. Nevertheless, the heat transfer rates are slightly higher. The mean deviation between measured heat and gas transfer rates was 5%. This difference can be explained by the comparison of a local measurement of heat transfer in a linear wind wave flume with integrated measurements of gas transfer.

[Haußecker and Jähne, 1995] used field data measured with the active controlled flux technique. The measured and scaled heat transfer rates are in good accordance to the empirical wind speed parametrisations for CO_2.

Furthermore, [Schimpf et al., 2004] combined field and laboratory measurements. Despite a huge scatter, he found a good agreement between the laboratory and field measurements of scaled heat transfer and direct gas transfer measurements. Only under conditions with a high surfactant coverage in the laboratory the passive thermography overestimates the transfer rates as the surface renewal approach underestimates the skin-bulk temperature difference.

There are several studies which are in contradiction to these findings. [Asher et al., 2004] used the active controlled flux technique under field conditions. A heated spot was used to determine heat transfer rates with the decay method (see section 4.3). The fitted curve was gained from the surface renewal model. The heat transfer velocities were scaled to a Schmidt number of 660 with a Schmidt number exponent of $n = \frac{1}{2}$. The resulting transfer rates are found to be a factor of two larger than directly measured transfer rates for CO_2.

Similar conclusions are drawn by [Atmane et al., 2004], who measured the transfer rates of heat (with the decay method) and two low soluble gases simultaneously under laboratory conditions. Between heat and gas transfer a factor of 1.4 - 3 was found. It was inversely proportional to wind speed, where the factor of 3 belongs to a wind speed of 3.8 $\frac{m}{s}$ and the factor of 1.3 to a wind speed of 9.5 $\frac{m}{s}$.

A third example finding a systematically higher heat transfer than gas transfer velocity under laboratory conditions is the work of [Zappa et al., 2004]. He found, that the measured heat transfer rates, scaled to Schmidt number 600, overestimates the simultaneously measured gas transfer rates by a factor 2-3.

In all these studies, different possible explanations are given for the significant differences between heat and gas transfer velocities. One possible reason is the Schmidt number exponent which is assumed as $n = \frac{1}{2}$. Especially for low wind speed it could be higher (up to $\frac{2}{3}$), causing the scaled transfer velocity to become smaller. As the more likely reason, the authors assume, that the penetration model describes the processes in a better way than the surface renewal model. Than, a Schmidt number scaling would only be possible for low soluble gases, whose mass boundary layer is thinner than the viscous boundary layer. This assumption is confirmed by [Jessup et al., 2009]. There simultaneous measurements of the surface temperature by radiometry, surface temperature distribution with an infrared camera and temperature profiles with depth were conducted under laboratory conditions. These measurements indicate that a significant fraction of the surface renewal events are only partial renewals, which do not reach all the way up to the surface.

These very different findings demonstrate, that it is still doubtful, if measured heat transfer velocities can be scaled to the transfer rates of low soluble gases. Therefore, more studies, using simultaneous measurements of heat and gas transfer, are necessary. Thereby, care must be taken for the Schmidt number exponents, influencing the scaling. As all the measurements finding a significant deviation between heat and gas transfer velocities, are measured by active thermography and analysed with the decay method, further studies comparing the different possible analysis methods (see chapter 4) are necessary, too.

5. Measurements

This chapter is divided in three parts. First the instruments which were used for the measurements are presented. The second part describes the two wind wave tanks, where measurements were conducted. It also explains the chosen conditions for the measurements. In the third section the conducted field measurements are described.

5.1. Used Instruments

In this section a short overview over the used instruments is given. Detailed technical data of the used cameras and lasers are shown in appendix A.1.

5.1.1. Infrared Cameras

All used cameras are cooled arrays of semiconductor detectors. Incident radiation releases charge carriers due to the internal photoelectric effect. In an applied electrical field they create a photocurrent, which is measured. To decrease the noise, the cameras are cooled to $77\,\mathrm{K}$ with an internal Sterling cooler. The measured intensity can directly be related to a temperature. The cameras are sensitive at wavelengths of $\lambda = 3 - 5\,\mu\mathrm{m}$. The properties of the heat radiation in this regime are described in section 2.1.2. The noise equivalent temperature difference (NEΔT), which is a characteristic for the performance of an infrared camera, was less than NEΔT $= 20\,\mathrm{mK}$. This corresponds to the lowest possible temperature resolution.

To avoid reflections of the cooled sensor itself in the image, the camera was never mounted perpendicular to the water surface, but with an angle of $10 - 20°$ to the vertical.

For the measurements described in this chapter, two different cameras where used: a *CMT256* from *Thermosensorik*, Erlangen, Germany and a *Velox 237k* from *IRcam*, Erlangen, Germany. There are lenses for the cameras with three different focal lengths of $f = 28\,\mathrm{mm}$, $f = 50\,\mathrm{mm}$ and $f = 100\,\mathrm{mm}$. All lenses are made of SiGe and can be used for both cameras. A more detailed description of the technical data is given in appendix A.1.

For most of the measurements the integration time was set to $2.5\,\mathrm{ms}$. Only for the measurements in Marseille an integration time of $1.5\,\mathrm{ms}$ was chosen, to reach higher frame rates.

All cameras have been calibrated with a blackbody, which is described in section 5.1.3, before each measurement campaign. To determine the spatial resolution at the water surfaces chessboards consisting of two different materials (alternating plastic and metal parts) were placed on the water surface in the begin of each measurement campaign. For the ship measurements a swimming target with lines of highly reflecting foils with a distance of $10\,\mathrm{cm}$ between each other was used.

5.1.2. Framegrabber

For the *Thermosensorik CMT 256* a *PLDA XSYS* framegrabber with highspeed attachment from *plda*, Aix-en-Provence, France, is used. The system enables to apply external voltages to three

input channels. This signals are saved in the first three pixels of each images. For the conducted measurements the laser on off signal, the scanner position in wind direction and additionally for the field measurements, the wind speed measured by the wind monitor were saved.

For the *IRcam Velox 237k* a *MicroEnable IV VD-4* framegrabber from *Silicon Software GmbH*, Mannheim, Germany, was used. It provides a camera link interface for the communication with the camera. It allows for real-time preprocessing during the data acquisition, which can be configured by programming the onbord FPGA.

For the conducted measurements the temperature calibration was implemented. Furthermore, it was possible to reduce the data volume from 14 bit to 8 bit. Therefore, the minimal temperature of a short sequences, which was acquired at the begin of the measurement, was determined and subtracted as an offset. As a second step the temperature range was selected, either from the temperatures occurring in this sequences or as an input parameter. This temperature range was divided in 256 steps (according to an eight bit resolution). The saved data contained therefore the increase of temperature in respect to the subtracted minimum with a resolution, which depends on the chosen temperature range.

For the conducted measurements a temperature range of 8.192 K was chosen. That leads to a temperature resolution of 32 mK per temperature step. This is less than twice the camera noise ($2 \cdot NE\Delta T = 40\,\text{mK}$). Therefore, the quantisation does not lead to a loss of information ([Jähne, 2012]).

5.1.3. Blackbody

For calibrating the infrared cameras a *2006G* blackbody from the manufacturer *Santa Barbara Infrared, Inc.* (Santa Barbara, USA) was used. Its temperature can be adjusted between $0°\text{C}$ and $60°\text{C}$ in steps of $0.001°\text{C}$ with an accuracy of $\pm0.01°\text{C}$. It has a emissivity of $\epsilon = 0.985 \pm 0.15$ and emits radiation with wavelengths of $2 - 14\,\mu\text{m}$.

To calibrate the cameras the whole expected temperature range was regarded in $0.25°C$ steps. To minimize the noise for each temperature 100 images were recorded and averaged. [Haußecker, 1996] showed that the lense of the infrared camera can be set to infinity for the calibration. A quadratic polynomial fit links the temperature T to the measured grey values G:

$$T = a + bG + cG^2 \tag{5.1}$$

This fit was conducted for every pixel separately to balance inhomogeneities of the sensor. This polynomial depends on the integration time of the camera, therefore the same integration time was chosen for both, the calibration and the measurements. To eliminate inaccuracies, the calibrations were conducted with the same lenses as the measurements and under the same conditions (especially the same surrounding temperatures) in the laboratory or directly onboard the research vessel. For the ship measurements a mirror was used to look at the water surface. The blackbody was mounted behind this mirror for the calibration measurements to avoid aberrations.

To retrieve the absolute water temperature, the calibrated value has to be corrected for the emissivity of water, which is $\epsilon = 0.95 - 0.98$. Since the analysis methods only regard temperature differences, this correction can be neglected. In addition, reflections have to be considered. Reflections of the cooled detector are avoided with the non perpendicular mounting of the camera (see 5.1.1). But reflections from the sky can still occur. If the sky is clear or completely covered, a temperature offset develops, which can be neglected as well, by regarding the difference of two temperatures. If the sky is inhomogeneously covered, reflections can be seen in the

images at positions depending on the slope of the surface. For that reason, the reflections move with the phase velocity of the waves.

5.1.4. Image Acquisition Software

The image acquisition as well as the control of the synchronisation electronics was conducted with the image processing software *Heurisko* from *AEON Verlag & Studio* (Hanau, Germany). Most of the data analysis was done with this software, too.

5.1.5. CO$_2$-Laser

For the conducted measurements two different CO$_2$-lasers were used. Both emit radiation at a wavelength of $\lambda = 10.6\,\mu$m. Due to this wavelength, the laser and its reflections are not directly seen by the used infrared cameras. The lasers are not continuous, but pulsed with $5\,$kHz. The pulse length defines the output power and is aritraryly adjustable. Both lasers are from the manufacturer *Synrad Inc*, Mukilteo, USA. For laboratory measurements in the Aeolotron a *Evolution 125*, for all other measurement a *firestar f200* is used. Technical details of both laser types are given in A.1.

To present the laser system from overheated, when they reach their high output power they are water cooled. Therefore, a *LT 4* or a *LT 5* chiller from *Deltatherm*, Much, Germany was used. Both lasers can be used with both chillers.

The *firestar f200* was used with an additional shutter box *SBf100* from *AuRa Tech GmbH*, Völkermarkt, Austria. It does not only enable to control the laser, including shutter for safety, laser power, laser on/off, electronically, but it enables to couple a visible beam of a laser diode into the light path. This diode was used for focussing of the laser optics.

Right after the laser outlet, the beam has a rectangular shape, with a diameter of $3.5\,$mm or $4.5\,$mm. Approximately after $1\,$m it changes to a Gaussian shape.

A two-dimensional scanner is used to deposit the heat to the water surface in different patterns. To prevent the scanner from damage, the laser beam is widened from $3\,$mm to $8\,$mm by a Keplerian telescope. For the measurements with a heated area instead of a pattern, the second lens of the telescope is replaced by a lens expanding the laser beam to a line perpendicular to the wind speed. All used optical elements are made of zinc selenide.

Although all used optical elements had coatings which are optimized for the lasers wavelengths, they absorb a small fraction of the lasers energy. For measurements where the deposed energy has to be known, the laser power was measured behind the optics.

5.1.6. Scanner

All used scanners are two dimensional galvanometer scanner. For the field instrument (which was also used for the laboratory measurements in Marseille) a *Micro Max 671* from *Cambridge Technology, Inc*, Cambridge, USA is used. For the Aeolotron measurements before 2012 a scanner from *GSI Lumonics*, Billerica, USA was used. Because one of the galvanometers was broken, in 2012 it was replaced by a *Hurry Scan II* from *ScanLab AG*, Puchheim, Germany for later measurements. All scanners are controlled by an analogue voltage delivered by self-built electronics or by a function generator. The mirrors are anti reflex coated with a coating which is optimized for the laser wavelength of $10.6\,\mu$m.

5.1.7. Synchronization of the ACFT

For the ACFT measurements, infrared camera, CO_2-laser and scanner have to be synchronized. Therefore, home-made electronics are used. There are different electronics for the different infrared cameras and lasers. For measurements with the *Thermosensorik CMT 256* an external clock gives a signal, which is divided in the frequencies for camera, laser and scanner. The scanner in wind direction can only be used with a sawtooth signal to heat an area.

For measurements with the *IRcam Velox 237k* the scanner signal is created with a function generator, which is triggered by the camera signal. Therefore, the scanning signal in both directions is arbitrary. The electronic is only necessary to regulate the laser, which is triggered by the camera signal, too.

5.1.8. Instruments to Measure the Ambient Parameters in the Aeolotron

In the Aeolotron the reference wind speed was measured by an anemometer (Greisinger STS 020) which is installed 10 cm under the ceiling, what means approximately 1.3 m above the water surface in the center of the flume.

Air and water temperature at several positions as well as the temperature of the incoming air were measured by PT-100 temperature sensors.

The humidity was monitored by four *HydroClip 2* humidity sensors from *rotronic messgeräte GmbH*, Ettlingen, Germany. Two were installed in the air space of the Aeolotron, one in the incoming and one in the outgoing air. They additionally measure the temperature and calculate the dewpoint at this positions.

The friction velocity was measured by [Bopp, 2011] with the momentum balance method described in section 3.2.2. It was not measured simultaneously with the heat and gas transfer measurements, but under identical conditions.

5.1.9. Wind Monitor

For the field measurements a wind monitor was installed on top of the ACFT measurement instrument. It was a wind monitor *JR-MA*, model 04106 from *young*, Traverse city, Michigan, USA. It can measure wind speeds from $0 - 60 \frac{m}{s}$ with a four blade helicoid propeller and the wind direction in $360°$ with a balanced vane. As the instrument was installed in front of the vessel's superstructures, the wind field was influenced. Therefore, for comparison the wind measurements conducted by the ships systems were used. They measured the wind speed at the vessel's mast directly in ten meters height.

5.2. Laboratory Measurements

5.2.1. Heidelberg Aeolotron

The Aeolotron in Heidelberg is an annular wind-wave facility, which was first described in [Jähne et al., 1999]. Since that time construction work has beenn carried out, including a new wind generator and changes in the air flushing system.

The Aeolotron has a diameter of $10\,\mathrm{m}$. The flume has a width of about $60\,\mathrm{cm}$ and a height of about $2.4\,\mathrm{m}$. For the conducted measurements the water column was of $1\,\mathrm{m}$ height. Therefore, the water volume amounts to about $18\,\mathrm{m}^2$ and the air volume to about $24.4\,\mathrm{m}^2$. All described measurements were conducted with deionized water.
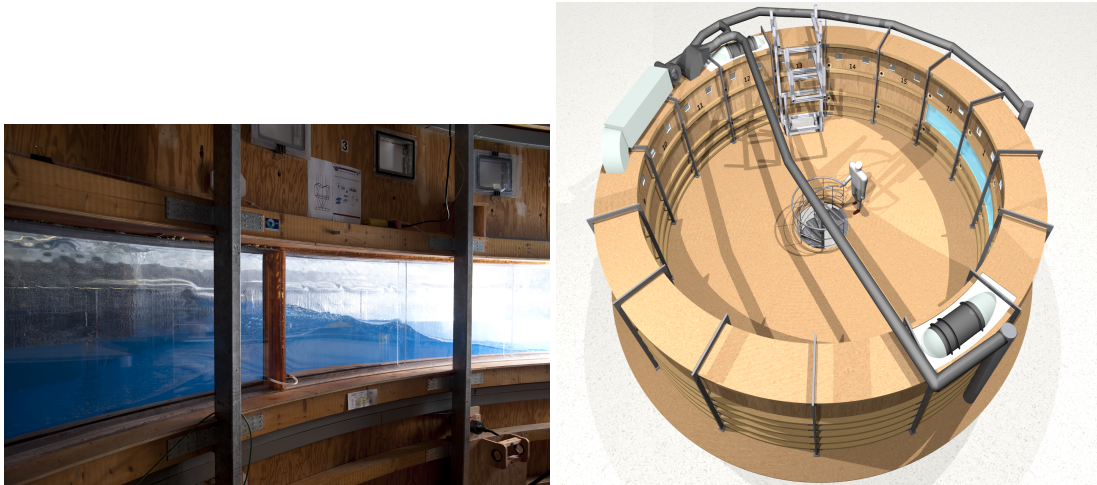
Figure 5.1.: The Heidelberg Aeolotron: left side: Look into the flume, right side: rendered view of the facility (taken from [Krall, 2013])

The annular shape of the flume leads to a quasi endless fetch, meaning that the wind can smear over the water surface for an unlimited period of time, whereby a stationary wave field develops. Therefore, the conditions in the facility are more similar to ocean conditions than in linear facilities. This is an advantage for the comparison between laboratory and field measurements. The drawback of this geometry is that the water body itself is set in motion and inertial forces occurs. Figure 5.1 shows a photograph of the view into the flume of the facility on the left side and a schematic of the facility on the right side.

Two axial ventilators generate wind with wind speeds up to $11\,\frac{\mathrm{m}}{\mathrm{s}}$.

The whole facility is thermally isolated to reduce heat exchange with the surrounding air. In addition the walls of the air space are covered with an reflective foil to avoid radiative heat transfer out of the facility. Different isolated windows enable image forming measurements.

It is possible to close the air space of the facility completely or to flush it with fresh air during the measurement. With closed air space, the facility has still some small leaks. There is a counter currency pump installed in the facility, but it was not used during the conducted experiments.

Ambient parameters like wind speed, water and air temperature and humidity at different positions of the facility can be observed.

Wind Speed in the Aeolotron

Due to the centrifugal force there is no logarithmic wind profile in circular wind wave tanks. This fact does not influence the transfer processes, but it complicates the comparison with measurements conducted in other facilities or in the field ([Jähne, 1980]).

The wind speed in the Aeolotron is measured in the center of the flume approximately $1.3\,\mathrm{m}$ over the water surface. To compare the Aeolotron measurements with any other measurements this reference wind speed u_{ref} has to be converted to a wind speed in ten meter height u_{10}.

[Nielsen, 2004] found a quadratic relationship between the measured reference wind speed and the water sided friction velocity:

$$u_{*\mathrm{w}} = 0.0271 u_{\mathrm{ref}}^2 + 0.0265 u_{\mathrm{ref}} + 0.0732 \qquad (5.2)$$

After the changes of the wind generation [Bopp, 2011] found the same relationship between friction velocity and reference wind speed.

It is transformed to the air sided friction velocity using equation 2.77. The drag coefficient can be calculated:

$$C_{\mathrm{d}} = \frac{u_{*\mathrm{a}}^2}{u_{10}^2} \tag{5.3}$$

For open ocean conditions [Smith and Banke, 1975] found, that using the drag coefficient the wind speed in ten meters height can be calculated:

$$10^3 C_{\mathrm{d}} = 0.63 + 0.66 u_{10} \tag{5.4}$$

[Krall, 2013] combines these equations to

$$u_{10}^3 + \frac{105}{11} u_{10} - \frac{50}{33} u_{*\mathrm{a}}^2 = 0 \tag{5.5}$$

which can be solved numerically for each measured friction velocity (see [Krall, 2013]).

Heat and Gas Exchange Measurements 2010

In spring 2010, heat and gas exchange measurements were conducted in cooperation with the research group of Jonathan Williams, Max Planck Institute for Chemistry, Mainz. Measurements were conducted at seven different wind speeds and were each repeated two or three times. Table 5.1 shows these different conditions for the conducted measurements. The air space was closed during each individual condition. Therefore, no latent heat flux occurred. The measurement time varied between the different conditions, from more than three hours for the lowest wind speed down to 30 minutes for the highest wind speed. Inbetween the wind speed conditions the facility was flushed with fresh air to lower the air-side concentration. Therefore, the fluxes from water to air are increased. The measurements were conducted with pure water. The water surface was skimmed at the beginning of every measurement day to avoid surface contaminations.

$u_{ref}\ \left[\frac{m}{s}\right]$	1.5	2	2.75	3.65	4.85	6.5	8.65
$u_{10}\ \left[\frac{m}{s}\right]$	1.71	2.43	3.27	4.81	7.05	10.6	15.0
26.04.2010		x		x		x	
28.04.2010	x	x	x	x	x	x	x
30.04.2010	x	x	x	x	x	x	x

Table 5.1.: Wind speeds used for Aeolotron heat and gas exchange measurements 2010.

For the heat exchange measurements the ACFT measurement instrument (see chapter 3.1.1) was mounted on the roof of the Aeolotron. During this campaign the *Thermosensorik CMT256* infrared camera with a 50 mm lens was used. With increasing turbulence (which corresponds to a higher wind speed in this experiment) the response time of the system decreases. For that reason the frame rate of the infrared camera was increased with wind speed. The used frame rates are shown in table 5.2. For each condition five sequences with one laser on/off cycle and two sequences with 2, 4, 8, 16 and 32 laser on/off cycles were conducted. If the measurement time was long enough also two sequences with 64 and 128 cycles were grabbed. The data were analysed with the amplitude damping method (see section 4.1).

For the comparison between heat and gas transfer, N_2O was used as a reference gas. It was measured during evasion measurements with an Fourier-Transformation-Infrared-Spectrometer

$u_{ref}\left[\frac{\mathrm{m}}{\mathrm{s}}\right]$		1.5		2	2.75	3.65	4.85	6.5	8.65	
26.04.2012	Framerate [Hz]		25			200		800		
28.04.2012	Framerate [Hz]		25	25	50	200	400	800	800	
30.04.2012	Framerate [Hz]		25	25	50	200	400	800	800	

Table 5.2.: Frame rates of the infrared camera chosen for the different measurement conditions in 2010.

(FTIR) by Kerstin Krall in the same way as the measurements described in [Krall, 2013]. The transfer rates were determined and provided only for the last measurement day with a mass balance approach (see section 3.1.3) by Christine Kräuter.

Mean squared slope measurements were conducted by Roland Rocholz with an colour imaging slope gauge.

Heat and Gas Exchange Measurements 2011

For the heat and gas exchange measurements in spring 2011 the same conditions as for the measurements in 2010 were chosen. They were again conducted in cooperation with the research group of Jonathan Williams, Max Planck Institute for Chemistry, Mainz.

$u_{ref}\left[\frac{\mathrm{m}}{\mathrm{s}}\right]$	0.75	1.5	2	2.75	3.65	4.85	6.5	7.51	8.65
$u_{10}\left[\frac{\mathrm{m}}{\mathrm{s}}\right]$	1.15	1.71	2.43	3.27	4.81	7.05	10.6	13.2	15.0
18.02.2011	x	x	x	x	x	x	x		x
22.02.2011	x	x	x	x	x	x	x		x
24.02.2011	x	x	x	x	x	x	x	x	
01.03.2011	x	x	x	x	x	x	x		x
03.03.2011		x	x	x	x	x	x		x
08.03.2011		x	x	x	x	x	x		x
10.03.2011		x	x	x	x	x	x		x

Table 5.3.: Wind speeds used for Aeolotron heat and gas exchange measurements in 2011.

Table 5.3 shows the wind speed conditions under which the measurements were conducted. Therein u_{ref} is the reference wind speed, measured in the Aeolotron and u_{10} is the wind speed approximated to the wind speed in ten meters height (see section 5.2.1). For the measurements on 03.03., 08.03. and 10.03 a soluble surfactant, Triton-X, was added in two different concentrations. For the measurement on March, 3rd, 0.6 g, for the measurement on March, 8th and on March, 10th, 3 g Triton X-100 were used. Like during the measurements in 2010, for the days without an additional surfactant, the water was skimmed in the beginning of each measurement day, avoiding contaminations with surface films. The measuring conditions were also the same as in the year before: The different wind speed conditions were measured one after another, starting with the lowest wind speed. The measurement time of each varied with the conditions from 4.5 h for the lowest wind speed down to 30 min for the highest wind speed, guaranteeing, that the gas concentrations in the air could reach an equilibrium state. Between each condition, the air space was opened to flush out the gases. The wind speed was changed after half of that time, meaning 15 minutes after each condition.

The gas measurements for N_2O were again conducted by Kerstin Krall with FTIR spectroscopy during evasion measurements. [Krall, 2013] contains a more detailed description of the gas measurements of this measurement campaign and its data analysis and results. To gain

the Schmidt number exponents she additionally conducted transfer measurements for C_2HF_5. The Schmidt number exponent was than determined from the ratio of the transfer rates for both gases, as described in section 2.2.7.

Heat exchange measurements were conducted simultaneously to the gas transfer measurements with the same instrument like in 2010. Due to a technical defect the synchronisation electronic of the laser and scanning system failed and the laser signal was only forced in one line to the water surface. As the laser was supposed to be scanned over an area, the laser power was rather high. Therefore, a stable layering can not be excluded.

Mean squared slope measurements were conducted by Roland Rocholz with an colour imaging slope gauge. Friction velocities were determined after the campaign under the same conditions by [Bopp, 2011].

Heat and Gas Exchange Measurements with Surfactants 2013

A third Aeolotron campaign was conducted in spring 2013 in cooperation with Klaus Schneider-Zapp, School of Marine Science and Technology, University of Newcastle, United Kingdom. The aim of this campaign was to investigate the influence of natural occurring surfactants on the air-sea gas exchange. The wind conditions were the same as in the measurements in 2010 and 2011 and are shown in table 5.4. The measuring process was the same as for the former measurements, described in the previous sections. In difference to the other measurements during the flushing periods the wind was switched off for a short while to enable surfactant sampling.

| $u_{ref}\left[\frac{m}{s}\right]$ | 1.5 | 2 | 2.75 | 3.65 | 4.85 | 6.5 | 8.65 |
$u_{10}\left[\frac{m}{s}\right]$	1.71	2.43	3.27	4.81	7.05	10.6	15.0
30.04.2013	x	x	x	x	x	x	x
03.05.2013	x	x	x	x	x	x	x
08.05.2013	x	x	x	x	x	x	x
10.05.2013	x	x	x	x	x	x	x

Table 5.4.: Wind speeds used for Aeolotron heat and gas exchange measurements 2013.

For the first two measurement days the soluble surfactant dextran was added with a concentration of $1\frac{mg}{l}$ and $2\frac{mg}{l}$, corresponding to a total amount of $18\,g$ and $36\,g$ respectively. At the third and fourth day additional to the dextran ($18\,g$), palmitic acid ($7.2\,mg$), phosphatidylglycerol ($36\,mg$) and mono-galactosyl-diacylglycerol ($95\,mg$) were added.

For the heat transfer measurements the *IRcam Velox 237k* with a 50 mm lens was used. In contradiction to the measurements in 2010 and 2011, the laser was not widened, but scanned in both directions. By applying a step function to the scanner in wind direction and a sawtooth signal to the one perpendicular to the wind direction, eight parallel lines were created perpendicular to the wind direction. The scanner was synchronized with the camera in a way that in every image one line was heated. As before the framerate was adjusted depending on the wind speed condition. With higher turbulence (and therefore with higher wind speed) the heat is transported faster from the water surface into the bulk. To avoid stable stratification, the water was not heated more the $0.5\,K$. For that reason, the laser power was set to a quite low value at the beginning of each measurement and increased with increasing wind speed. Frame rates and laser power for all measured conditions are given in table 5.5. The data were evaluated by the investigation of the spatial behaviour of the Fourier transformation (see section 4.4) and by the decay curve method (see section 4.3).

$u_{ref} \left[\frac{m}{s}\right]$		1.5	2	2.75	3.65	4.85	6.5	8.65
30.04.2013	Framerate [Hz]	24	24	48	48	72	96	120
30.04.2013	Laser Power [%]	50	60	60	60	70	80	95
03.05.2013	Framerate [Hz]	24	24	48	56	72	96	120
03.05.2013	Laser Power [%]	40	45	50	70	80	90	95
08.05.2013	Framerate [Hz]	24	24	48	56	72	96	120
08.05.2013	Laser Power [%]	40	40	45	60	70	80	95
10.05.2013	Framerate [Hz]	24	24	48	56	72	96	120
10.05.2013	Laser Power [%]	40	40	45	60	70	80	95

Table 5.5.: Framerates of the infrared camera and laser power used for Aeolotron measurements 2013.

Simultaneous gas exchange measurements for N_2O and C_2HF_5 were conducted by Kerstin Krall. She used FTIR spectroscopy to measure the concentration and a mass balance method to determine transfer rates in evasion measurements. The N_2O measurements were used for comparison of heat and gas transfer measurements. A combination of both gases was used to determine the Schmidt number exponents, see [Krall, 2013].

Mean squared slope measurements were conducted by Daniel Kiefhaber and Svenja Reith with an high speed imaging slope gauge (see section 3.2.1 and [Kiefhaber et al., 2014]). Friction velocities were measured by Maximilian Bopp [Bopp, 2014].

5.2.2. Marseille Phytheas
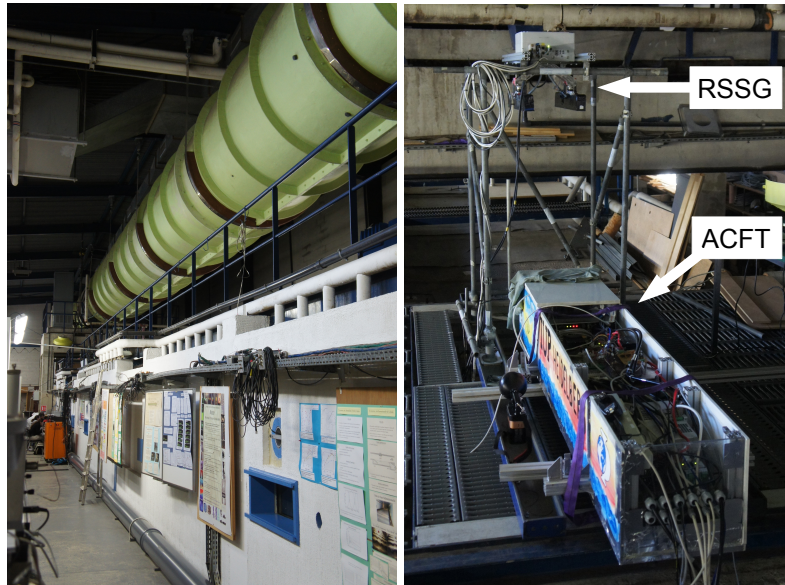
Figure 5.2.: Images of the wind-wave tank Phytheas (left) and the ACFT and RSSG instruments mounted on top of the flume (right).

The Marseille wind-wave facility Phytheas is located at the Mediterranean Institute of Oceanography in Marseille-Luminy, France. It was first described by [Coantic and Bonmarin, 1975]. It is a linear wind-wave tank with a length of $40\,\mathrm{m}$. The measurement section is located at a fetch

of 27 m. The water basin has a wide of 2.6 m and a filling level of about 0.7 m. The overlying air space has a width of 3.2 m and a height of 1.5 m. The air is recirculated.

Wind with a speed of $0 - 13 \frac{m}{s}$ is created by an axial fan. Additional gravity waves can be produced by a mechanical wave maker. At the end of the flume a wave absorbing beach is installed.

Figure 5.2 shows images of the wind wave facility (left) and the installed measuring instruments, ACFT and RSSG (see section 3.1.1 and 3.2.1) on top of the flume (right).

Heat and Wave Measurements 2012
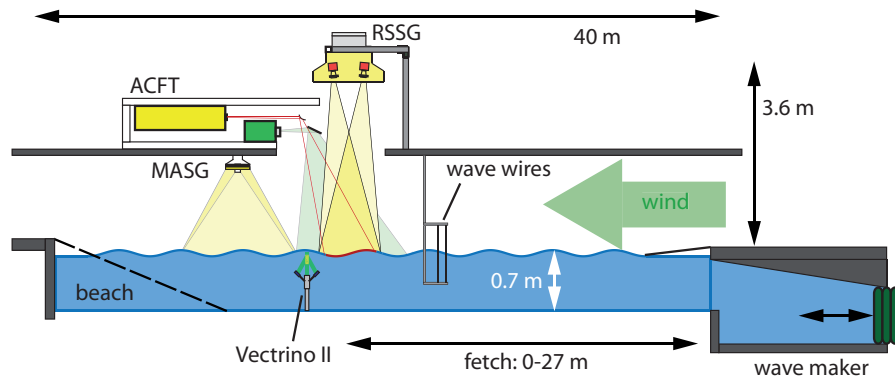
Figure 5.3.: Schematic of the wind wave facility Phytheas with all instruments installed during the measurements in 2012 - taken from [Kiefhaber, 2014].

In September 2012 a two week experiment was conducted in the Marseille facility. For this measurements the ACFT field instrument with the *IRcam Velox 237k* infrared camera with the 28 mm lens was used. Besides the ACFT, a reflective stereo slope gage, RSSG, was measuring mean squared slope at the same patch. Furthermore, an additional system for the mean squared slope measurements, the MASG was installed. First results of the wave statistic measurements are given in [Kiefhaber, 2014]. As the instrument was installed at a fixed position the fetch was varied by covering parts of the water surface with bubble wrap. Measurements were conducted at fetches of 2.2, 4.6, 9.4 and 27 m. For each fetch six wind speeds (2.5, 3, 4, 5, 8 and $10 \frac{m}{s}$) have been used. The water surface was skimmed, when the fetch was varied to eliminate contaminations, which were inserted into the flume during spreading the bubble wrap. But the effect of surfactants are not as crucial as in the Aeolotron, as the wind blows contaminations to the end of the linear flume. The data were evaluated by the investigation of the spatial behaviour of the Fourier transformation (see section 4.4) and by the decay curve methode (section 4.3).

The wind speed was measured with a pitot tube. Due to the linear shape of the flume a logarithmic wind profile develops. Therefore, the measured wind speed can be scaled to the one in ten meters height using this logarithmic wind profile (see section 2.3.1). Next to the RSSG, wave statistics, measured with a wave wire, were provided by Guillemette Caulliez, Mediterranean Institute of Oceanography, Marseille-Luminy. She furthermore provided mean square slopes, which were measured in earlier campaigns under similar conditions. A Nortek Vectrino II profiling velocimeter (operated by Christopher Zappa and Sophia Brumer, Columbia University's Lamont-Doherty Earth Observatory, New York, USA) measured water-sided turbulence. This turbulence data are still under evaluation.

Figure 5.3 shows a schematic of the wind wave tank with all instruments, installed during this measurement campaign.

5.3. Field Measurements
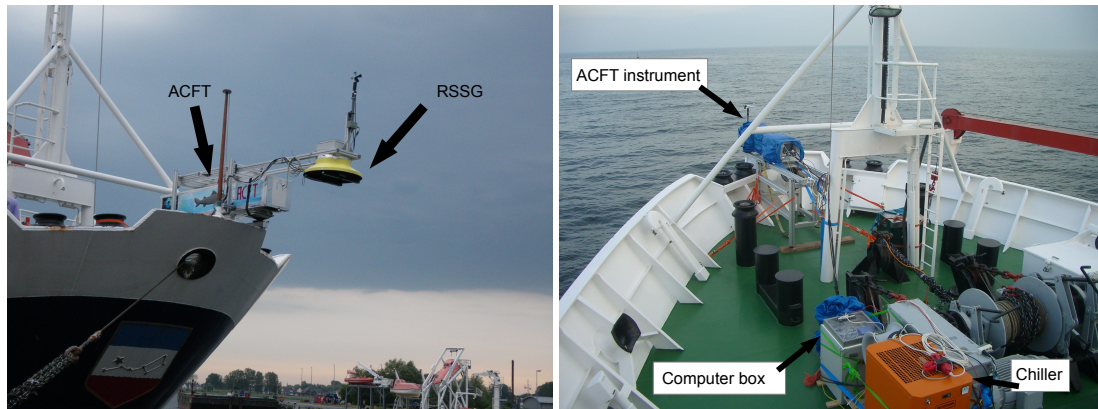
Figure 5.4.: ACFT and supplies mounted on board *FS Alkor*.

For field measurements the ACFT measurement instrument (see section 3.1.1), including the infrared camera, laser, scanner, optics and synchronization electronics, was installed in a watertight box, with an closable opening window for the measurements. Therein the camera is looking over a mirror to the water surface with an angle of $15 - 20°$. The box was mounted on two slide rails on an aluminium cradle on the bow of different research vessels. It could be locked at a position onboard for transit and moved and locked over the ocean in front of the vessel for the measurements. The computer, operating the system, was installed in a second watertight box close to the cradle. Figure 5.4 shows the ACFT instrument and the RSSG mounted onboard of *FS Alkor* and the installation of the ACFT supplies on deck.

The RSSG (reflective stereo slope gauge) is an instrument to measure wave statistics and described in section 3.2.1. It was installed on top of the ACFT instrument in a way that it is looking perpendicular to the water surface at the same position as the ACFT.

The measurements were conducted only at stations, where the ship kept its position with the bow pointing into the wind direction. Although the ship was not driving at these stations, it drifted with the currency or the wind. In-between the measurements, during transit times the opening window was closed and the air in the water tight box was dried with silica gel to protect the optics and electronics of the high humidity.

In the framework of this thesis three cruises took place in the Baltic Sea on two different research vessels. Figure 5.5 shows the tracks of all three cruises drawn into a map of the Baltic Sea. This section describes the details of these conducted measurements.

5.3.1. FS Alkor

Two measurement campaigns were conducted onboard the German research vessel *FS Alkor* in cooperation with the Institut für Ostseeforschung, Warnemünde. Therefore, two different measurement campaigns took place in the Baltic Sea.

Alkor336

The cruise 'ALKOR336' in the Baltic Sea in took place from April 25th, 2009 until March 7th, 2009. The first stations were conducted in the neighbourhood of the research platform *FINO2*, than some more on the way to and in the Gotland Sea. On the way back to Rostock all stations
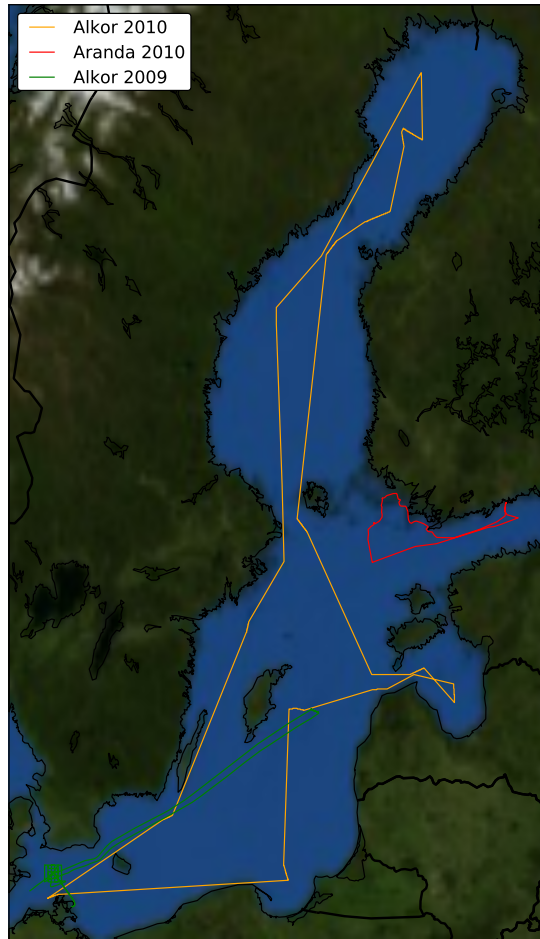
Figure 5.5.: Map of the Baltic Sea with the cruise tracks for all three field measurement campaigns.

had to be cancelled because of the stormy weather conditions. All together measurements were conducted at nine stations with varying weather conditions. The wind speed ranged from $2\,\frac{m}{s}$ up to $13\,\frac{m}{s}$. The air temperature varied from $6°$ C to $11°$ C and the water temperature was between $6°$ C and $10°$ C. Measurements were conducted at day and night time and both, under cloudy and clear sky conditions. The detailed data for wind speed, temperature and humidity were delivered by the ships measurement systems.

During this cruise the *Thermosensorik CMT256* infrared camera was used with a 50 mm lens. The laser beam was expanded to a line. By scanning this line a heated area at the water surface was created. Two different types of sequences were conducted. For the first type the laser was running for the whole measurement time. Images were grabbed with an frequency of 800 Hz. For the second type the laser was switched on and off during the measurement. The laser on/off frequency was chosen that 2, 4, 8, 16, 32, 64, 128 and 256 cycles fitted in one sequence, respectively. The infrared camera frame rate was 400 Hz. The laser output power was set to 75%, resulting in 150 W. The results shown in section 6.1.2 are obtained from the measurements with this second data type.

First results of the 'ALKOR336' cruise are already shown in [Schimpf et al., 2011].

Alkor356

The second cruise 'ALKOR356' onboard *FS Alkor* took place from June, 30th until July 13th, 2010. During the whole cruise the weather conditions were sunny and rather calm with wind speeds between $1.5 \frac{m}{s}$ and $8.3 \frac{m}{s}$. The water temperature varied between $12°$ C and $20°$ C depending on the geographical position and the air temperature varied between $13°$ C and $23°$ C depending of the position and the daytime. The detailed data for wind speeds, temperature and humidity were delivered by the ships measurement systems.

Heat exchange measurements were conducted at 16 different stations all over the Baltic Sea at night and day. Therefore, again the *Thermosensorik CMT256* infrared camera was used with a 50 mm lens. The frame rate was 400 Hz. The laser was widened to a line and scanned to heat an area. The laser power was set to 95 %. The laser was switched on and off with frequencies, which were chosen in a way that 2, 4, 8, 16, 32, 64, 128 and 256 cycles fitted in one sequence, respectively.

5.3.2. RV Aranda

Another campaign in the Baltic Sea was conducted in cooperation with the *Finish Meteorological Institute* onboard the finish research vessel *RV Aranda* during the cruise 'CO2_WAVE10_CTD 10/2010'. The cruise took place from September 14th till September 19th, 2010. The original cruise plan had to be changed because of stormy weather conditions. Therefore, most stations were conducted very close to the shore, inbetween the coast and some islands on two different positions. This measurements were fetch limited. Only the last station was conducted offshore under open ocean conditions. Altogether eight stations have been conducted. The wind speeds were in the range from $9 \frac{m}{s}$ until $15 \frac{m}{s}$. The air temperature was in the range of $10°$ C - $15°$ C and the water temperature was between $13°$ C and $16°$ C. The detailed data for wind speeds, temperature and humidity were delivered by the ships measurement systems.

Like at the both other cruises, the *Thermosensorik CMT256* camera with a 50 mm lens was used. Again sequences with 1, 2, 4, 8, 16, 32, 64, 128 laser on/off cycles were grabbed with a frame rate of 400 Hz. The laser was again widened to a line and scanned in wind direction. The laser power was set to 95%.

6. Results

For the analysis of the infrared images several methods, are available as described in chapter 4. In previous studies, measuring the heat transfer across the water surface, the amplitude damping method was found to be very reliable. The measured transfer velocities of heat were found to be in good agreement with gas exchange measurements conducted in the same facility [Libner, 1987] or with empiric parametrisations [Popp, 2006]. To continue these works, thermographic measurements of heat exchange, analysed with the amplitude damping method, were conducted simultaneously with mass balance methods to determine the transfer rates of nitrous oxide in two laboratory experiments. The results of these measurements, confirming the previous works, are shown in section 6.1.1. One advantage of the thermographic measurements in comparison to other methods is the usability, both in the laboratory as well as in the field. In section 6.1.2 the first successful application of the amplitude damping method to field data, conducted at three campaigns in the Baltic Sea, will be presented.

Although these sections show, that the amplitude damping is a reliable method to determine heat transfer rates, it has one drawback: the integration time of one measurement is in the order of $20 - 30\,\text{min}$. Environmental conditions, such as wind speed, rain or surfactant coverage, can change within this time frame. To increase the physical understanding of the individual factors influencing the air-sea heat and gas exchange, a higher time resolution is desirable. For that reason, two more laboratory measurements, allowing to test two faster analysis methods are presented in section 6.2. Finally this chapter terminates with a summary of the found advantages and drawbacks of the different analysis methods in section 6.3.

6.1. Results of the Amplitude Damping Method

In this section heat transfer velocities, determined with the amplitude damping method will be shown. First in section 6.1.1 heat transfer rates obtained from two laboratory campaigns in the Aeolotron are shown and compared to gas transfer velocities. Using the same analysis method, results of three field campaigns at the Baltic Sea with different wind speed conditions are shown in 6.1.2. Afterwards, in section 6.1.2 laboratory and field data are compared.

6.1.1. Laboratory Measurements

As described above previous studies found good agreement between heat transfer velocities, determined with the amplitude damping method and gas transfer rates. These studies compared the heat transfer rates to gas transfer rates, measured under the same conditions in the same facility [Libner, 1987] or to to empiric parametrisations [Popp, 2006]. Due to inconsistencies of former thermographic measurements (see 4.5), one aim of this study is to confirm the applicability of the amplitude damping method, using simultaneous heat and gas transfer measurements under laboatory conditions. Therefore, two measurement campaigns were conducted in the Heidelberg Aeolotron in 2010 and 2011.

Aeolotron 2010

In 2010 simultaneous measurements of heat and gas transfer measurements were conducted. With the help of the amplitude damping method, heat transfer velocities can be determined. The damping curves and the corresponding fit curves for all conditions are shown in the appendix A.2.
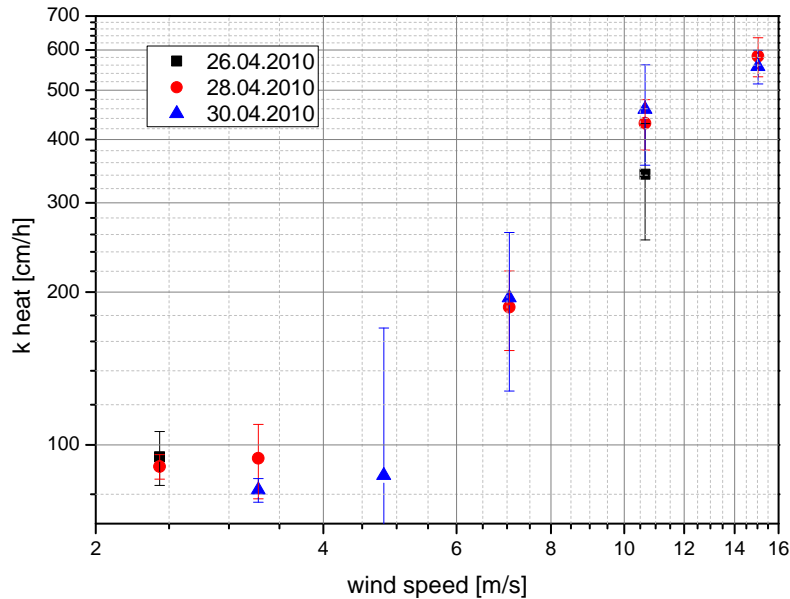
Figure 6.1.: Heat transfer rates measured in the Aeolotron in 2010 plotted against the wind speed in ten meters height.

Figure 6.1 shows the measured heat transfer rates plotted against the wind speed in ten meters height (see section 5.2.1). As expected they show an increase with wind speed. The three repetitions agree in the range of the errors.

These measurements enable a direct comparison of the measured transfer rates of heat and nitrous oxide (N_2O). As no Schmidt number exponents were determined during these measurements, those determined from the measurements in 2011, which were conducted under identical conditions, were used for the Schmidt number scaling. The Schmidt number used for heat was $Sc_{\text{heat}} = 7.2$, corresponding to a water temperature of $19°C$ and the measured transfer rates were scaled to Schmidt number $Sc = 600$.

Gas transfer rates are available only for the last of the three measuring days (30.05.2010). They were determined by Christine Kräuter (unpublished data) with a mass balance approach. The values are given in appendix A.4.1. Figure 6.2 shows the comparison of the simultaneous heat and the gas transfer measurements. The blue line show the values where heat and gas transfer rates are equal. The comparison shows a very good agreement between the measured heat and gas transfer velocities within the error margins. That indicates that transfer rates measured for heat can be converted into those of gases like CO_2 or N_2O by Schmidt number scaling, if the correct Schmidt number exponents are known. Therefore, the previous studies are confirmed by these measurements. While the possibility of scaling heat transfer velocities to those of gases is proven for the Aeolotron measurements, a lot of care has to be used when generalising that
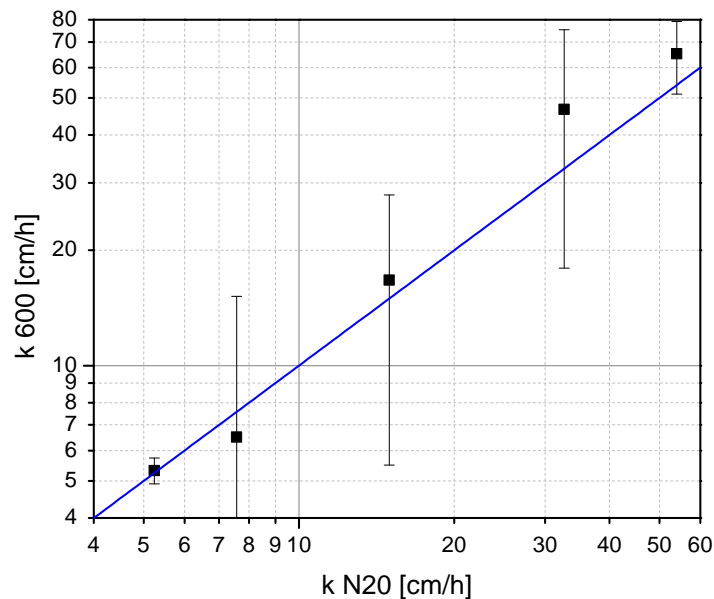
Figure 6.2.: Comparison of the scaled heat transfer rates (k 600) to the simultaneously measured transfer rates of N_2O for the Aeolotron measurements conducted on 30.04.2010.

to all measurements in other facilities or under open ocean conditions. The heat transfer rates are determined locally at one fixed location in the Aeolotron, while the gas transfer rates are integrated over the whole facility. As the Aeolotron has a virtually unlimited fetch and measurements were conducted when the wave field was in equilibrium this effect should be rather small. Nevertheless, inhomogeneities in the wind field, for example caused by the wind generators or by built-in measurement devices, could cause slightly different processes at different positions of within wind wave facility.

An ongoing study by [Bopp, 2014] looks more closely into the wind field in the Aeolotron. Once it is investigated in more detail, a final judgement on the inhomogeneities and their influence on global and local techniques can be made.

Aeolotron 2011

In 2011 measurements were conducted under the same conditions as in 2010. Because of technical problems due to a malfunction of the electronics synchronising infrared camera, laser and scanner, heat transfer rates could not be determined (see section 5.2.1).

However, the environmental conditions, like wind speed, were exactly the same as for the heat transfer velocities measured in 2010, which were analysed with the robust amplitude damping method. For that reason the heat transfer rates measured in 2010 can also be compared to the gas transfer rates for N_2O measured in 2011. Schmidt number exponents were determined from this measurement for N_2O and the simultaneous measured C_2HF_5 transfer rates by Kerstin Krall [Krall, 2013]. They show a smooth transition from $n = 0.663$, corresponding to a smooth surface, for the lowest wind speed to $n = 0.48$, corresponding to a wavy surface, for the highest wind speed. Figure 6.3 shows the measured Schmidt number exponents, averaged over all measurement days without surfactants in 2011.
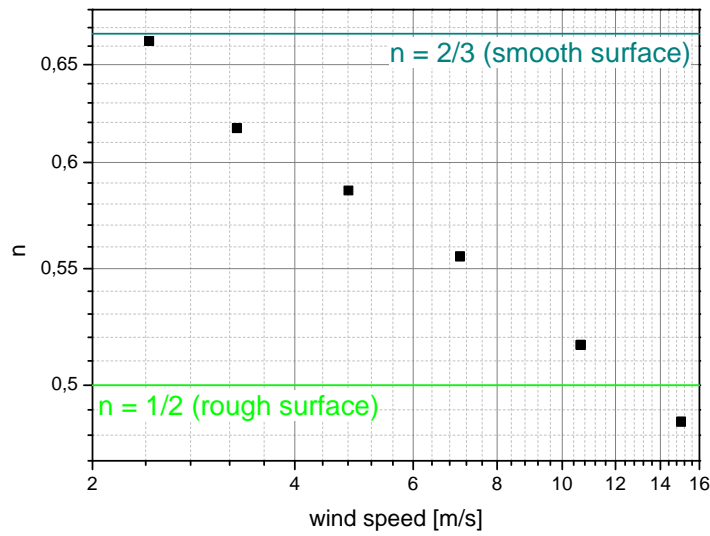
Figure 6.3.: Measured Schmidt number exponents, averaged over all measurement days without surfactant for the measurements conducted in the Aeolotron in 2011 - values taken from [Krall, 2013].
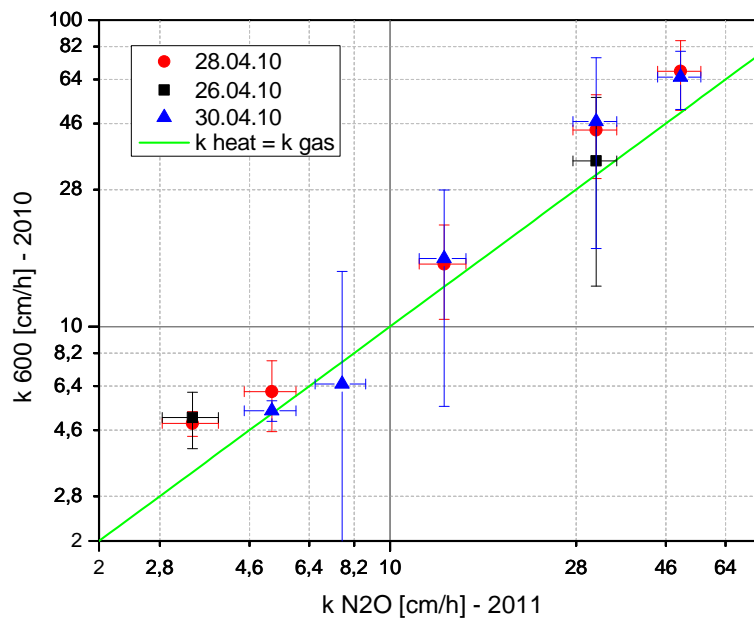
Figure 6.4.: Comparison of the scaled heat transfer rates (k 600) measured in 2010 and the gas transfer rates for N_2O measured in 2011.

By scaling one transfer rate with an erroneously assumed Schmidt number exponent of $n = \frac{1}{2}$ for a rough surface, instead of $n = \frac{2}{3}$ for a flat surface, the resulting gas transfer velocity differs by a factor of two. Using equation 2.48 the ratio of the different scaled heat transfer rates are

described by

$$\frac{k_{\frac{1}{2}}}{k_{\frac{2}{3}}} = \frac{\left(\frac{Sc_1}{Sc_2}\right)^{-\frac{1}{2}}}{\left(\frac{Sc_1}{Sc_2}\right)^{-\frac{2}{3}}} = 2.099 \tag{6.1}$$

This illustrates the sensitivity of the Schmidt number scaling is to the Schmidt number exponents. Therefore, unknown Schmidt number exponents are a significant source of error when comparing heat and gas transfer measurements.

The measured heat transfer rates from 2010 were scaled to Schmidt number 600 with this measured Schmidt number exponents from 2011. Figure 6.4 shows the comparison between these scaled heat transfer rates and the gas transfer velocities from 2011. The green line shows the values where the heat and gas transfer velocities coincide. The transfer rates from both measurement campaigns are in good agreement. This illustrates the good reproducibility of the laboratory measurements of gas transfer rates.

6.1.2. Field Measurements

The last section proved that the amplitude damping analysis is a very robust method to determine heat transfer velocities and that the resulting heat transfer rates can be reliably scaled to the one for gases. Therefore, this method was applied to field data for the first time.
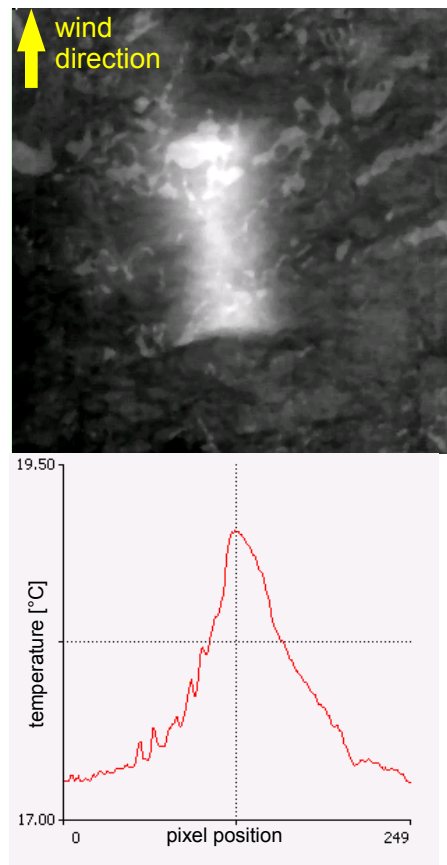
Figure 6.5.: Example for an infrared image recorded in the Baltic Sea and temperature profile through the heated area.

For field measurements, the use of the amplitude damping method has one additional advantage. In general, under field conditions reflections (for example from the sky or from the ship itself) can never be eliminated. These reflections overlay the measured temperatures. As the camera is installed at an oblique angle, it does not face the water surface perpendicular, the reflections are only detected at certain pixel positions, depending on the slope of the water surface. Therefore, the reflections seem to move with the waves. This effect would perturb the analysis with help of the ΔT or the decay curve method. For analyses in the Fourier domain, this effect can be neglected as it occurs at typical wave frequencies which are different from the analysed laser on/off or scanner frequency.

Figure 6.5 shows one exemplary infrared image of the water surface after $1.7\,\mathrm{s}$ of heating, recorded in the Baltic Sea. The above-mentioned reflections are distributed over the whole image. The heated area can is visible in the middle of the image. The broadening of the laser perpendicular to the wind speed (horizontal in the image) depicts the Gaussian profile of the laser beam.

To determine heat transfer velocities under ocean conditions, three cruises were conducted in the Baltic Sea. All measured damping curves as well as the corresponding fit curves are shown in Appendix A.2. Furthermore, the values of the resulting heat transfer rates are given in the same section.

Alkor 2009

The measurements conducted onboard *FS Alkor* in 2009 span a wide range of wind speeds from $u_{10} = 5 - 13\,\frac{\mathrm{m}}{\mathrm{s}}$, but 75% of the measurements were conducted in a medium wind speed range between $u_{10} = 6 - 9\,\frac{\mathrm{m}}{\mathrm{s}}$.

There are no direct gas transfer measurements available for comparison. Therefore, the results can only be compared to the empiric gas transfer parametrisations described in section 2.2.9. The obtained heat transfer velocities were scaled to those for carbon dioxide by Schmidt number scaling (see section 2.2.7) with a Schmidt number exponent of $n = \frac{1}{2}$, as a wavy surface can be assumed for all the measurements. The Schmidt number for heat was $Sc = 10 - 11$, corresponding to water temperatures of $5.5 - 8.5°C$. The shown error bars are the sum of the error of the fit and the standard deviation from five measurements, conducted at one station. The measured and scaled heat transfer rates are shown in figure 6.6 in dependency of the wind speed in ten meters height u_{10}. They fit well to the empiric parametrisations (section 2.2.9), which are shown in same figure. This is one more indication that the transition from heat to gas transfer velocities with Schmidt number scaling is possible. Furthermore, it confirms again the robust determination of heat transfer velocities with the amplitude damping method. Therefore, it confirms the findings of the laboratory studies in the Aeolotron that heat can be used as a proxy tracer for air-sea gas exchange measurements.

The results of this cruise show clearly, that the technical requirements are given to deploy the ACFT measuring instrument under ocean conditions in a way, that enables an amplitude damping analysis. Furthermore, the comparison with the empiric parametrisations shows, that the instrument not only allows a determination of heat transfer rates, but also to scale them to the transfer velocity of water-side controlled tracers, like for example CO_2, He or SF_6. Therefore, the system can be used to study small-scale air-sea interaction processes, both in the laboratory and on the open ocean.
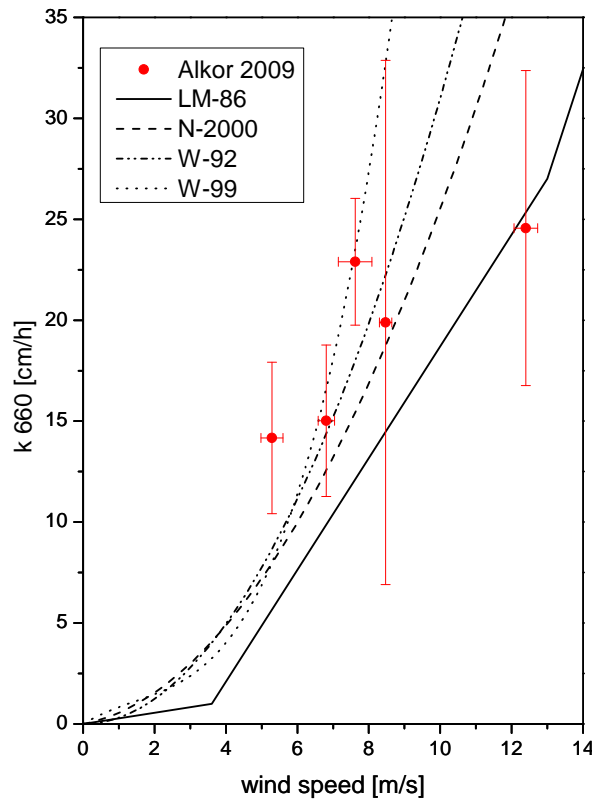
Figure 6.6.: Scaled heat transfer velocity, measured during the cruise 'ALKOR336' in comparison with empiric gas transfer parametrisations (see section 2.2.9) - re-evaluated after [Schimpf et al., 2011].

Alkor 2010

During the cruise onboard *FS Alkor* in summer 2010 very calm conditions with extremely low wind speeds prevailed. At low wind speeds, the system requires a long time to reach the thermal equilibrium as the response time increases quadratically with increasing wind speed ($\tau \propto u_{10}^2$). In contradiction the surface drift velocity, which moves the water from the heated area does only increase linearly with increasing wind speed ($v_{\mathrm{drift}} \propto u_{10}$). Therefore, the time needed to reach thermal equilibrium is decreasing with increasing wind speed. For field measurements the ship will never stay exactly at one position, but will drift with the current or the wind or a combination of both. Therefore, the time a water parcel stays in the heated patch is limited by the fact that the ship and therefore the infrared camera is moving compared to the water surface. For that reason it is questionable if the thermal equilibrium was reached at this low wind speeds.

To quantify this effect the maximum time a water parcel can stay in the heated patch was estimated. Therefore, the images taken when the laser was switched off were used to track the movement of the heated patch. Out of this data an apparent surface drift velocity, describing the actual surface drift relative to the movement of the ship, is calculated. With this velocity, the maximum time a water parcels stays in the heated area is calculated: $t_{\max} = \frac{x_{\mathrm{heated}}}{v_{\mathrm{app}}}$, where x_{heated} is the length of the heated area and v_{app} is the apparent velocity between ship and water surface. Response times, which are larger than this estimated residence time can not
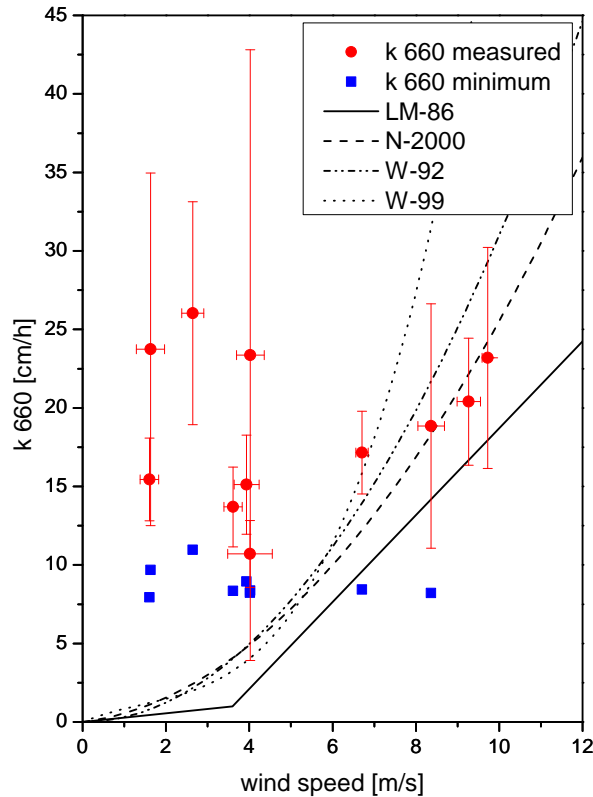
Figure 6.7.: Scaled heat transfer rates measured during the cruise *Alkor356* onboard *FS Alkor* in the Baltic Sea in 2010 (red) in comparison with the empiric parametrisations (black), see section 2.2.9. The blue dots are the lower limit for the resolvable transfer rates due to the ship movement.

be measured. Therefore, an upper limit for the response time, resulting in a lower limit for the resolvable transfer rate, is given.

Figure 6.7 shows the measured heat transfer rates, which are scaled to a Schmidt number of $Sc = 660$, corresponding to carbon dioxide in salt water at $20°C$. The Schmidt number of heat was $Sc = 6.99 - 8.23$, corresponding to a water temperature of $14.5 - 20°C$. For comparison the empiric parametrisations described in section 2.2.9 are also shown. The measured transfer rates are much higher than the values predicted by the parametrisations. The lower limit of the transfer rates, which can be resolved by the system are included in the figure as blue dots. All measured transfer rates are larger than this limit. Except for the values at wind speeds higher than $u_{10} = 5 \frac{m}{s}$, where the measured transfer rates are in good agreement with the parametrisations, the transfer velocities, predicted by the empiric parametrisations, are significantly lower than the resolvable values. Therefore, it is not surprising, that the measured transfer velocities are much higher than the empiric parametrisations. These measurements illustrate a limitation of the active controlled flux technique: reliable measurements are available only when a patch of the water surface can be heated for a time which is longer than the response time of the system. Especially at low wind speeds and for measurements from moving platforms this effect has to be taken into account.

Aranda 2010

The measurements conducted onboard *RV Aranda* took part at high wind speeds only. Most of the transfer rates were measured at the same position with a limited fetch. In addition a few measurements were conducted offshore at a slightly lower wind speed. This enables an investigation of the fetch dependency of the transfer rates.
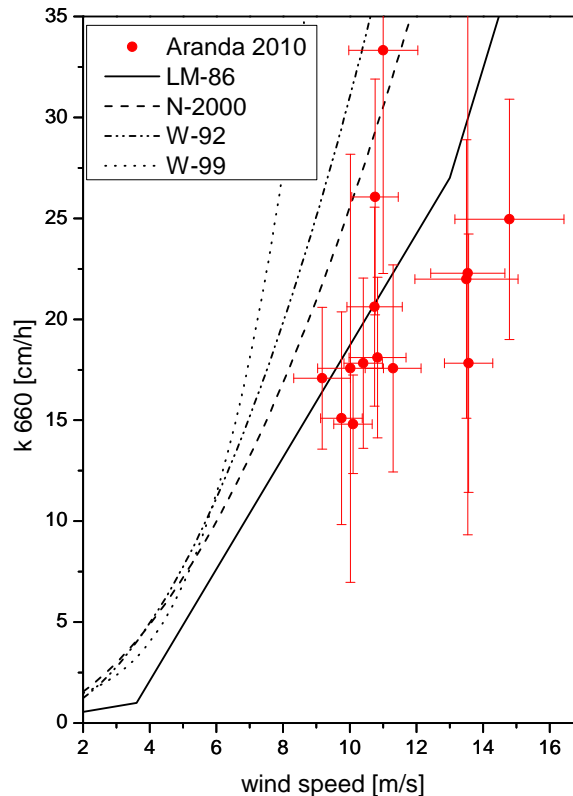
Figure 6.8.: Scaled heat transfer velocity, measured during the cruise 'CO2_WAVE10_CTD 10/2010' on RV Aranda in comparison with empiric gas transfer parametrisations (see section 2.2.9).

Figure 6.8 shows the measured heat transfer velocity scaled to a Schmidt number 660 against the wind speed in comparison to the empiric gas exchange parametrisations (see section 2.2.9). The Schmidt number of heat was $Sc = 10.17$, corresponding to a water temperature of $8°C$. Although the measured values are in the same order of magnitude as the parametrisations, they seem to underestimate the transfer velocity. There are two different possible reasons: First the ACFT measurements do not include bubble mediated gas transfer and second, the measurements are conducted under fetch limited conditions. Both possibilities will be described here:

The measured values of the transfer velocities can be lower than the parametrisations as the active controlled flux technique does not measure the bubble induced gas transfer. At these high wind speeds breaking waves and therefore bubbles occur. They increase the gas exchange for CO_2 (see section 2.3.4). Geochemical tracer or eddy covariance measurements, which are used to generate the empiric parametrisations (see section 2.2.9), include the bubble mediated gas transfer. Therefore, a deviation between the measured transfer rates and the parametrisations

can occur. This effect illustrates the second limitation of the active controlled flux technique: under high wind speed conditions the measured transfer rates are lower than the total transfer, as bubble mediated gas transfer is not included. Although for the direct comparison of heat and gas transfer, this effect is a drawback, for studying the different processes influencing the gas transfer, this effect can be an advantage, as the influence of bubbles can be directly separated from the transfer across the water surface.

The second reason is that most of the Aranda measurements were conducted under fetch limited conditions among islands with rather low wave ages, where the wave field was not in equilibrium with the wind forcing. Therefore, the exchange is expected to be lower than the parametrisations. In that case the deviation between heat transfer measurements and gas transfer parametrisations is a physical effect and not due to the measurement technique. This effect influences both heat and gas transfer measurements. Leaking simultaneous measurements of heat and gas transfer, both effects, bubble induced gas transfer and fetch limitation can not be seperated.

Furthermore, as can be seen in figure 6.8, the data show a big scatter in the measured transfer rates at the same wind speed. As most of the measurements were conducted at the same position and under similar surface and wind conditions, the scatter in the obtained transfer velocities indicates that wind speed is not the best physically parameter to model the transfer velocity. In addition to the wind speed other parameters like wave age or surfactant coverage influence the wave field and therefore the gas exchange. For further field campaigns a combination of the ACFT with measurements of different wave parameters would be desirable to determine the influence of these wave parameters, which could lead towards a physical based gas transfer parametrisation.

Comparison of Different Field Measurements

All field measurements were conducted in the Baltic Sea. As no wave parameters (like for example mean square slope) or friction velocity measurements are available for those campaigns, the only way to link the results with a directly measured parameter is the wind speed in ten metres height.

The results of all three campaigns are in good agreement. Nevertheless, the comparison also emphasizes the above mentioned limitations of the active controlled flux technique. At low wind speeds, the movement of the ship restricts the maximum measurable response time and therefore the minimum resolvable transfer rate, as explained in section 6.1.2.

At high wind speeds the measured transfer rates are slightly underestimated. The reasons were already discussed in section 6.1.2. The most likely explanation is, that the active controlled flux technique is insensitive to bubble mediated gas transfer. Nevertheless, for wind speeds in the range of approximately $5\,\frac{m}{s} - 12\,\frac{m}{s}$, there is a good agreement between the measured heat transfer rates and the empirically predicted transfer rates of carbon dioxide. Therefore, in this wind speed regime the ACFT was found to be a reliable instrument to measure heat transfer rates in the field. Furthermore, it was shown that heat can be used as a proxy tracer for the transfer of weakly soluble gases like carbon dioxide.

6.1.3. Comparison of Laboratory and Field Measurements

For both the laboratory and the field measurements presented in this section, the same measurement and analysis method was used. Thus it is possible to compare them. Heat and gas transfer
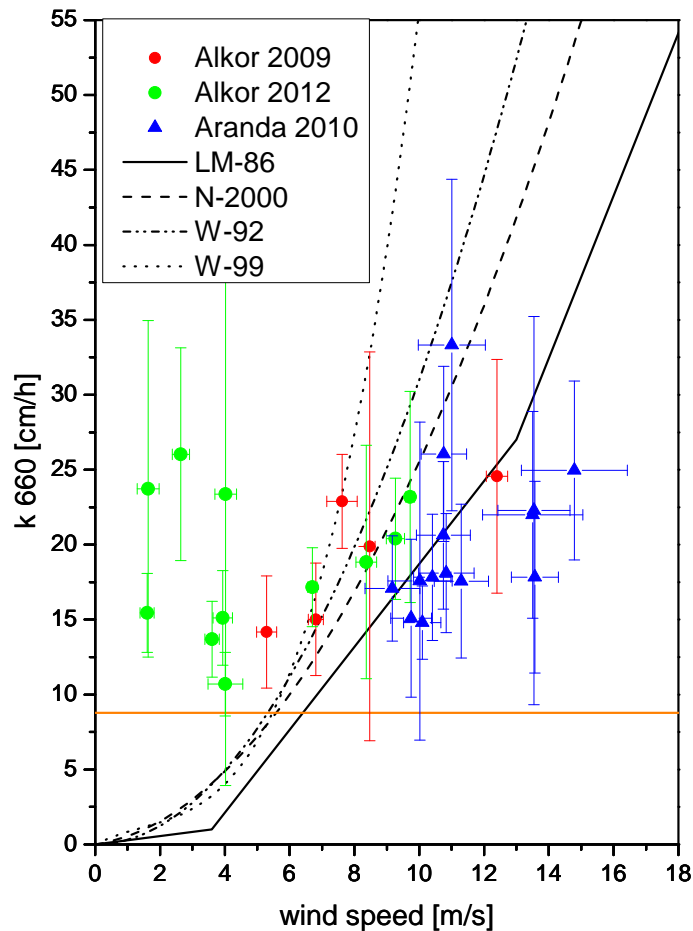
Figure 6.9.: Scaled heat transfer rates for all three cruises conducted in the Baltic Sea compared to the empiric parametrisations of the gas transfer of carbon dioxide (see sectin 2.2.9). The orange line shows the minimum values for the measurements on FS Alkor in 2010. Transfer rates below this line can not be resolved.

measurements in the laboratory were shown to be identical (see sections 6.1.1 and 6.1.1). In addition to the measurements with a clean water surface during the laboratory campaign in the Aeolotron 2011, measurements of the transfer rate of nitrous oxide were conducted with two different concentrations of the surfactant Triton X-100 in concentrations of $0.033 \frac{mg}{l}$ and $0.167 \frac{mg}{l}$. This allows a further comparison between the surfactant influenced transfer velocities measured in the laboratory to those measured under natural conditions on the open ocean.

Figure 6.10 shows this comparison. As the measurements conducted onboard *FS Alkor* in 2010 did not reach the thermal equilibrium for most of the conditions (see section 6.1.2) this data is not included. The comparison shows that laboratory and field measurements are in agreement. This indicates that laboratory studies are a valuable tool to investigate the air sea gas transfer and the results can be extended to field measurements. Of course the big scatter found in the field data from *RV Aranda* is still present. As no wave parameters or friction velocity were measured during the campaigns in the Baltic Sea, the used wind speed in ten meters height is the only possibility available to compare the laboratory and field data. This once more confirms (like
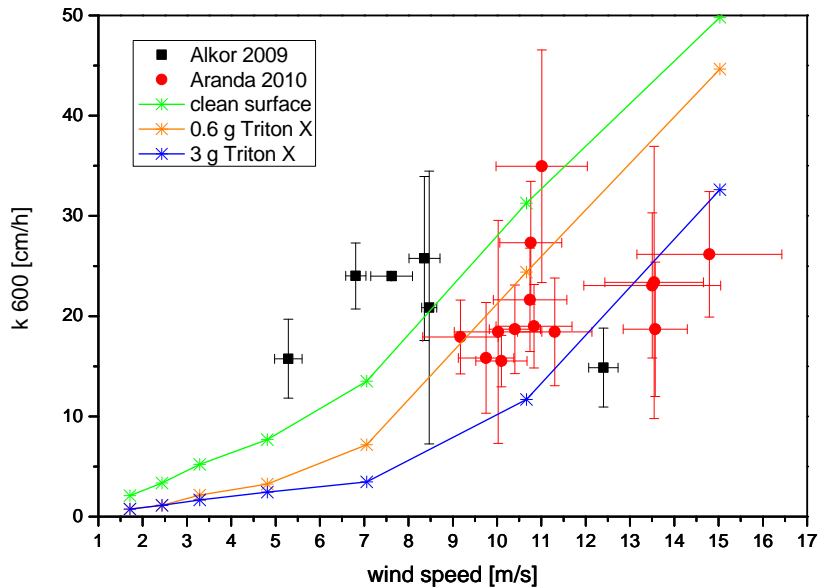
Figure 6.10.: Measured and scaled heat transfer rates from two campaigns in the Baltic Sea in comparison to measured N_2O transfer rates from the Aeolotron campaign in 2011 with different concentrations of the surfactant Triton X-100.

concluded in section 6.1.2) that in addition to the heat exchange measurements, investigations of wave parameters are desirable for future field measurements.

Furthermore, the comparison of the field measurements with the measurements with different surfactant concentrations illustrate the huge influence of surface films on air-sea gas exchange. While the measured heat exchange rates at wind speeds higher than $9\,\frac{m}{s}$ are lower than the gas exchange rates for clean water, they are in agreement with the surfactant covered case. Therefore, surfactants are an additional possible reason for deviations of heat transfer measurements in comparison to the empiric parametrisations for the field measurements. This also clearly indicates that wave and turbulence damping due to surfactant coverage is an important mechanism influencing air-sea gas exchange. To study the effect of surfactants in more detail, an additional measurement campaign with naturally occurring surfactant species was carried out in 2013 in the Aeolotron. Results from this campaign will be presented in 6.2.2.

6.2. Results with Higher Temporal Resolution

The results of the previous section showed, that the amplitude damping is a reliable method to analyse active thermographic measurements. The results are in good agreement with gas transfer measurements and can be used in the laboratory and in the field. Nevertheless, the method still has one major drawback. The integration time is in the order of $20-30\,\text{min}$. Although this resolution is high enough for laboratory measurements, where environmental parameters like wind speed, rain and temperature can be kept constant for the time needed for one measurement, these factors can change within minutes under field conditions. Furthermore, surfactants are not always distributed equally, but patchy at the water surface. The influence of these surfactants cannot be resolved with the temporal resolution of the amplitude damping method. Therefore, for future process studies an analysis method with a higher temporal resolution is desirable. For

that reason, two additional laboratory campaigns with different laser forcing were conducted in Heidelberg and Marseille. The faster analysis methods used are the investigation of the spatial behaviour of amplitude and phase (see section 4.4) and the decay curve method (see section 4.3). In this section the measured heat transfer velocities, determined with both methods, will be presented and compared to gas exchange measurements in the same laboratories.

6.2.1. Marseille 2012

The first of the two measurement campaigns to investigate analysis methods with a higher temporal resolution was conducted in Marseille in 2012. Gas exchange measurements are available from the year 2006 conducted by Kai Degreif (unpublished data). He conducted measurements with several different gases, allowing to determine Schmidt number exponents, too. The results of these measurements are given in appendix A.4.3. To allow a comparison of these gas transfer measurements with the heat transfer velocities, measured in this study, the measurements in 2012 were carried out under the same conditions than the ones in 2006. The heat transfer measurements were conducted by heating eight parallel lines at the water surface. Therefore, the data could be used to test the evaluation with the help of the decay curves and with the investigation of the spatial behaviour of amplitude and phase (see chapter 4).

Decay Curves
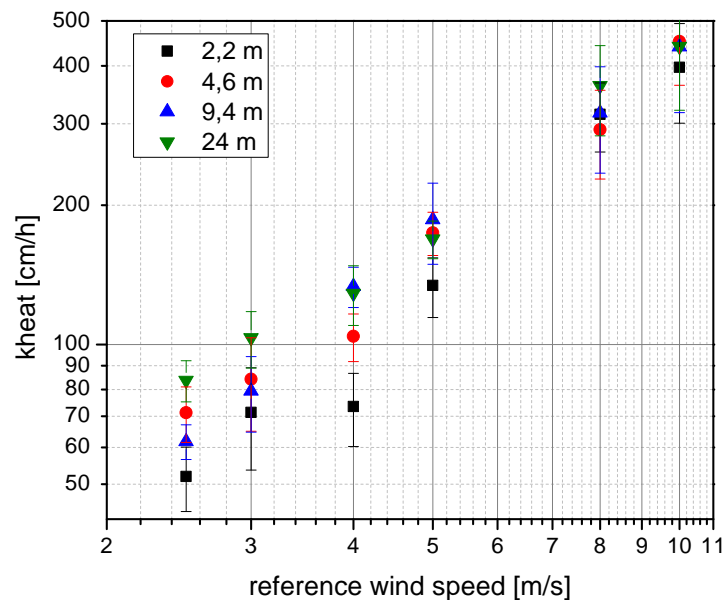
Figure 6.11.: Measured heat transfer velocity, determined with the decay curve method, over wind speed for different fetches, measured in Marseille, September 2012.

The mathematical description of the decay curves introduced in section 4.3 is the result of a numerical simulation by [Reinelt, 1994] and [Haußecker, 1996]. This one dimensional simulation is based on the surface renewal model. However, the formulation in equation 4.13 did not describe the behaviour of the temperature decrease of the laser lines during the measurements conducted in Marseille. As the fit of equation 4.13 to the measured data was not possible, for

the analysis the prefactor was set constant and only the exponential decay was fitted. Out of this fit the response time and then the transfer velocity for heat are calculated using equation 4.10. The results are given in the appendix in A.3.1.

Figure 6.11 shows the resulting heat transfer rates over the reference wind speed measured in the wind wave facility. They increase with wind speed according to the expectation. As described in section 5.2.2 measurements were conducted at six different fetches between 2.2 m and 27 m. For the lower wind speeds, the shortest fetch (2.2 m) is resulting in transfer rates which are only 60% of the transfer rates measured at the same wind speed with the highest fetch. The larger fetches show no clear fetch dependency. For the two conditions with highest wind speeds no fetch dependency is found.

The decay method was used in former studies by several authors with contradictory results (see section 4.5). Therefore, the reliability of the method is tested by comparing the measured heat transfer rates with the gas transfer rates measured in 2006 by Kai Degreif (unpublished data). He measured transfer rates for five different tracers: nitrogen (N_2), helium (He), methane (CH_4), nitrous oxide (N_2O) and dichlorodifluoromethane (F12). Those measurements allowed to calculate Schmidt number exponents from five different gas combinations: N_2 -F12, He - F12, He -N_2O, CH_4 -F12 and He -CH_4. All these calculated Schmidt number exponents show a similar shape with a transition from higher to lower values at medium wind speeds of about $u = 3 \frac{m}{s}$ to about $u = 7 \frac{m}{s}$. But the absolute values differs a lot. For all wind speeds which are lower than the transition regime, the Schmidt number exponent was set to $n = \frac{2}{3}$ and for the wind speed above this regime to $n = \frac{1}{2}$. For the measurement with a wind speed of $u = 5 \frac{m}{s}$ a Schmidt number exponent of $n = 0.543$ according to the measurements of CH_4 and F12 is used, as the absolute values of this combination was closest to the theoretically predicted values of $n = \frac{2}{3}$ and $n = \frac{1}{2}$. For the comparison between heat and gas transfer rates, the measured gas transfer velocities for N_2O were scaled to Schmidt number 7 (corresponding to heat at $20°C$). For the measurements in 2006 the water temperature was between $15.7°C$ and $17°C$, which leads to Schmidt number in the range of 703 - 754.

Figure 6.12 shows this comparison. The heat transfer measurements were conducted at different fetches, the gas transfer measurements with mass balance methods are always integrated over the whole fetch. This complicates the comparison. Therefore, the heat transfer measurements for all four fetches are shown. The comparison does not yield a consistent result: for low and medium wind speeds the two measurements seem to agree, while for the measurements with higher wind speed the transfer rates for heat are significantly higher than the ones for gas transfer.

There are several different explanations for deviations between the different transfer rates, resulting from the analysis with the decay curve method. For the determination of the shape of the decay curve the surface renewal model was used (see section 4.3), therefore the validity of this model has to be assumed. Furthermore, to determine the decay curve the laser line was tracked and the intensity of the centre of mass was regarded over the time. However, the laser line is not only moving with the surface drift, but is also broadened by diffusion, resulting in a decrease of the temperature of the centre of mass. Therefore, the determined response time tends to be underestimated and the transfer rates are overestimated.

Spatial Behaviour of Amplitude and Phase

The second possibility to determine the heat transfer velocity for the measurements in Marseille is the investigation of the behaviour of amplitude and phase. This method results from a solution
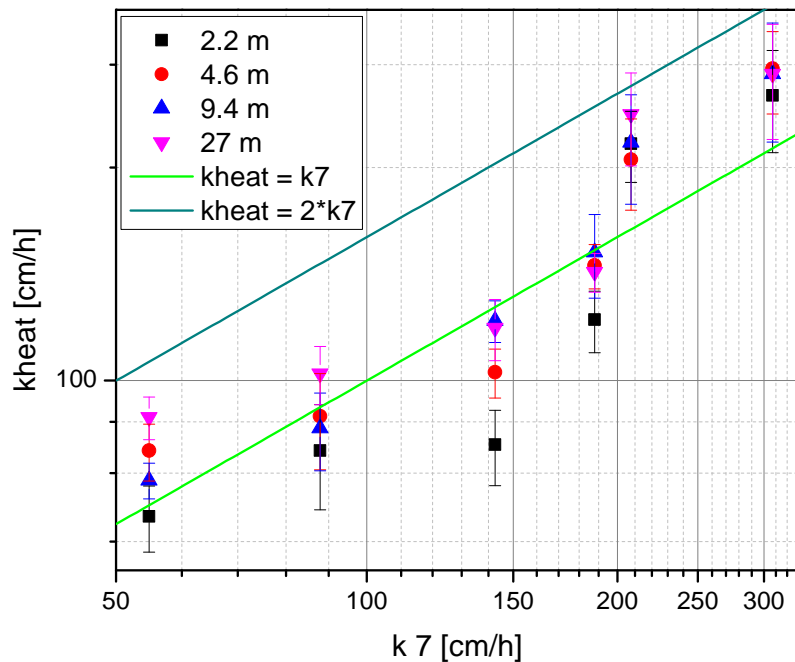
Figure 6.12.: Measured heat transfer velocities in comparison with the scaled transfer velocities of nitrous oxide. The lines show where the both transfer rates coincide and where the heat transfer is twice as large as the measured gas transfer.

of the differential equation describing heat exchange for the surface renewal model under the impact of surface drift (see section 4.4 or [Haltebourg, 2014]).

The spatial behaviour of amplitude and phase in wind direction is shown in figure 6.13 for one typical sequence with a wind speed of $3\,\frac{m}{s}$ at a fetch of $4.6\,m$. The red dots illustrate the positions of the heated lines. A closer look into this plot shows that the signal needs a relaxation distance behind the heated line before turning into the part with a linear behaviour, which is marked in yellow. Therefore, the ranges, where amplitude and phase are linearly decreasing is very short. The slopes of this decrease are the main parameters of this analysis method. They have to be determined from maximum ten values. Therefore, the accuracy of this analysis method can be improved a lot in further measurements if the distance between the heated lines is enlarged.

The second parameter influencing the heat transfer velocity is the surface drift, which is measured in an additional processing step from the infrared images. It is determined from the shift of the heated lines in the infrared images with time. This movement is a superposition of the surface drift and the wave movement. The waves furthermore lift and lower the water surface. The infrared camera is not looking perpendicular to the water surface, but with an angle in the order of $20°$ to minimize the reflections of the cooled detector of the infrared camera itself. Therefore, the change in water hight results in an apparent movement of the laser line. This effect adulterates the measured surface drift velocities. Figure 6.14 illustrates this effect. The blue lines are the water surface at two different water heights. The red points are the laser spots which are are situated at the same position at the water surface. As the camera is mounted tilted to the water surface with an opening angle α, the pixel positions x_1 and x_2 differ with the water height. To minimize the effect the velocity was averaged over all lines and over the whole measure-
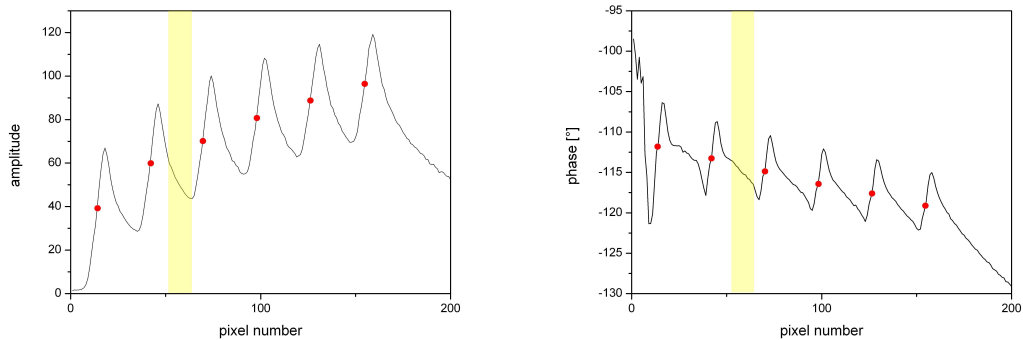
Figure 6.13.: Spatial distribution of amplitude and phase in the Fourier domain for one typical sequence. The red dots mark the position of the laser lines. The yellow area shows one example for a regime taken for the data analysis.
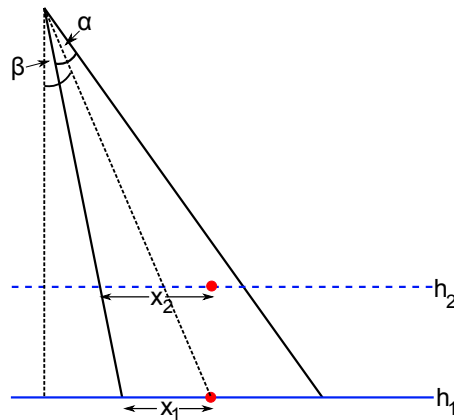
Figure 6.14.: Apparent position of the laser in the infrared image depending on the water height. In this example the laser is seen in the middle of the image at a water height h_1 and far outside of the middle at water heigth h_2.

ment time of one sequence. This results in an inaccuracy in the allocation of surface drift and measured slopes. For future measurements combined thermography and height measurements to correct this effect are planned. It will first be implemented in the Aeolotron where a height measurement is already available. For the calibration of the apparent movement with the height a very high accuracy is necessary. Later on a height measurement could be implemented into the field measurement instrument, too. This height effect does change the spatial behaviour of amplitude and phase, too. With the infrared images corrected for the height the accuracy of the slopes and therefore of the whole measurement will be improved, too.

Although it was the first time this method was used and the analysis provides possible improvements for future measurements, heat transfer velocities were determined. The results are given in the appendix A.3.1. Figure 6.11 shows the gained heat transfer velocities over the wind speed. Although they show, like expected, an increase with the wind speed, they show no fetch dependency. However this is not surprising as this analysis method leads to large uncertainties in the determined transfer rates. The error bars correspond to the standard deviation of the single values. The expected fetch dependency, as found in earlier studies, for example by [Jähne et al., 1989], is supposed to be less than the errors of the measured heat transfer rates.

Figure 6.16 compares the measured heat transfer rates to the N_2O transfer rates, described in the first part of this section. The green line shows, where heat and scaled gas transfer velocities
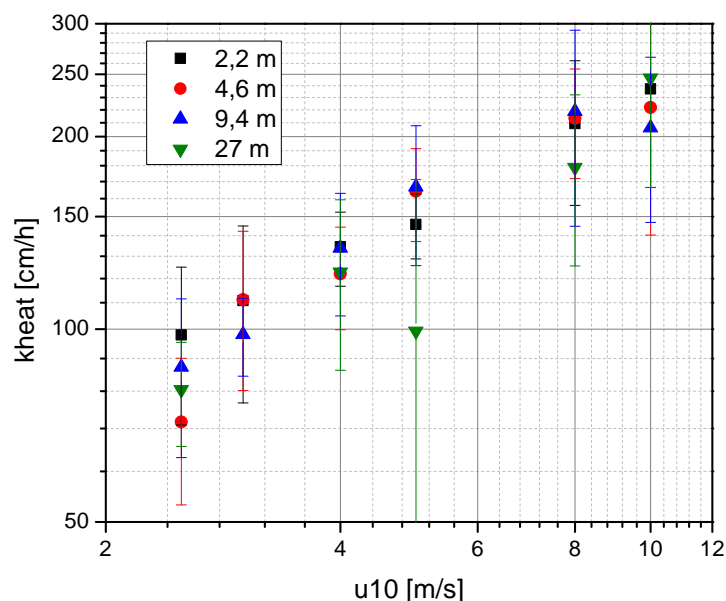
Figure 6.15.: Measured heat transfer velocity, determined by the investigation of the spatial behaviour of amplitude and phase over wind speed for different fetches, measured in Marseille, September 2012.

are identical. The data seems to be in good agreement at medium wind speeds. Nevertheless, the heat exchange measurements seem to overestimate the gas transfer rates for lower wind speeds and to underestimate them at the highest wind speed.

The reliability of this analysis methods is still uncertain. The analysis method is based on the surface renewal model. Therefore, this model has to be assumed as correctly descrining the physical processes regulating heat exchange. A sensitivity study will be done in [Haltebourg, 2014].

Comparison of Both Analysis Methods

A comparison of both analysis methods is shown in figure 6.17 for all measured conditions. The blue line shows the coincidence of both analysis methods. For medium wind speeds both analysis methods agree. At low wind speeds, the analysis of the spatial behaviour of amplitude and phase seem to slightly overestimate the transfer rates in comparison to the decay curve method. Nevertheless, in this region there is a lot of scatter in the measured data, showing that more precise measurements, optimized for the analysis method with the help of the spatial behaviour is necessary to compare the data. At high wind speeds, it behaves the other way around: the transfer rates analysed with the decay curves are considerably higher than the one determined with the spatial behaviour of amplitude and phase in the Fourier space. This could be due to the above-mentioned uncertainties for the decay method. Nevertheless, it is unclear how precise the method to investigate the spatial behaviour of amplitude and phase estimates the transfer rates at higher wind speeds.

Altogether the results do not suffice to judge the reliability of the evaluation methods. Both analysis methods showed partly coincidence with and partly deviations from the directly measured gas transfer rates. Possible reasons for the deviations are already given in the previous
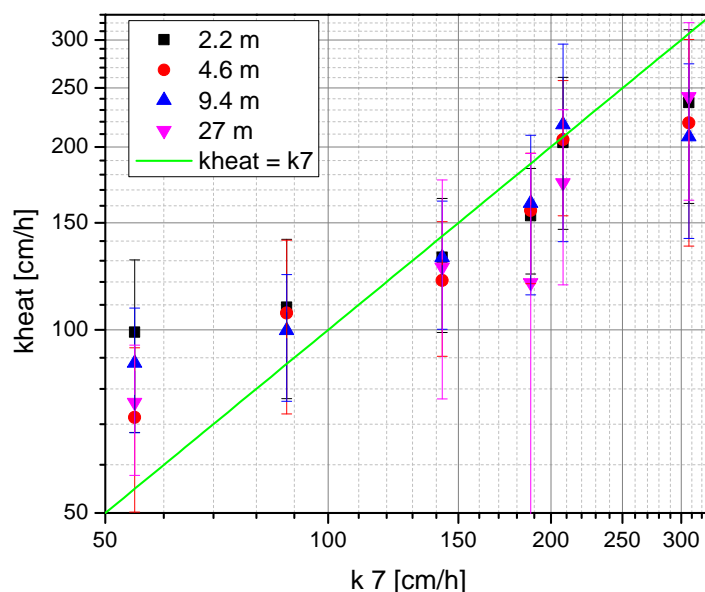
Figure 6.16.: Heat transfer velocity (k heat) determined with the help of the spatial behaviour of amplitude and phase in comparison to the measured N_2O transfer velocities, which are scaled to a Schmidt number of 7 (k7) measured in Marseille.

parts of this section. To improve the understanding of the behaviour of these analysis methods, more studies are necessary.

6.2.2. Aeolotron 2013

The aim of the measurements in 2013 was to investigate the influence of natural surface films on the air sea gas exchange. Furthermore, they provide another possibility for a direct comparison between heat and gas transfer rates, as both were measured simultaneously. Like for the measurements in Marseille in 2012, the laser pattern consisted of eight parallel lines perpendicular to the wind speed. Again two different analysis methods of the thermographic data were used: the spatial behaviour of amplitude and phase in the Fourier domain and the decay curves.

Transfer rates for nitrous oxide and Schmidt number exponents were measured by Kerstin Krall using the same methods as for the Aeolotron measurements in 2010 and 2011, described in section 5.2.1. The data are still under evaluation, but preliminary, unpublished gas transfer velocities and Schmidt number exponents can be used to compare the measured heat and gas transfer rates.

Decay Curves

The analysis using the decay curves was conducted in the same way as described in section 6.2.1.

The left side 6.18 shows the gained heat transfer rates over the reference wind speed. On the first and second measuring days one dextran was used as a surfactant, for the other days, the whole mixture of surfactants was inserted (see section 5.2.1). Therefore, a significant difference between the transfer velocities measured on these two days is expected, especially for low wind
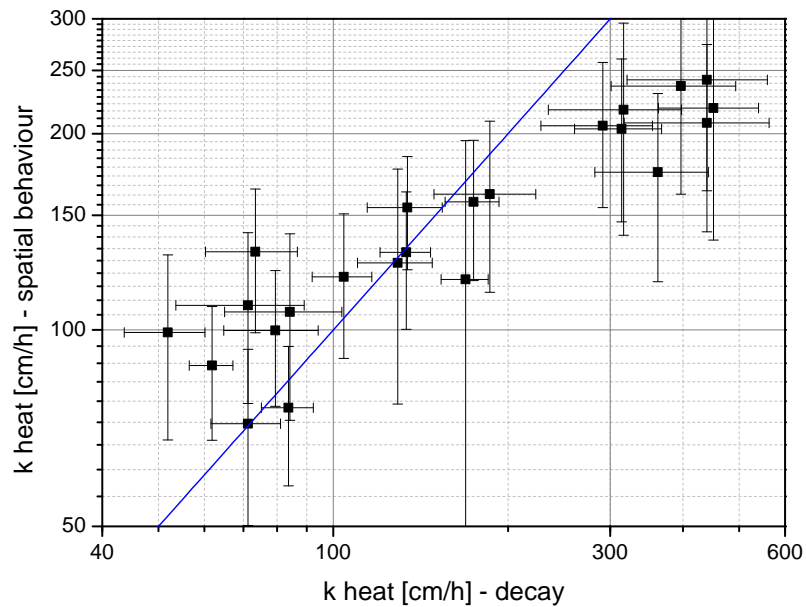
Figure 6.17.: Comparison of the heat transfer rates determined with two different analysis methods (decay curves and spatial behaviour of amplitude and phase) for the measurements in Marseille 2012.

speeds. However, the heat transfer velocities show this dependency only at medium wind speeds. In contradiction the measured gas transfer rates (provided by Kerstin Krall, preliminary data) show the expected behaviour for the low and medium wind speeds. Only for high wind speeds, when the film was disrupted, the measured transfer velocities coincide for all four days. This indicates that this analysis method overestimates the heat transfer rates at low wind speeds. To investigate the reliability of the method a comparison with directly measured gas transfer rates is done. The preliminary results for the transfer velocities are scaled to Schmidt number $Sc = 7$ with the Schmidt number exponents determined from the gas measurements.

Figure 6.19 shows this comparison. The two lines show where the heat and gas transfer rates coincide and where the heat transfer velocity is twice as high as the gas transfer velocity. For these measurements the heat transfer rates clearly overestimate the simultaneously measured gas transfer velocities by approximately a factor of two. One possible reason, which was already described in section 6.2.1, is that the detection of the centre of mass neglects the influence of the diffusion on the response time and leads to overestimated transfer rates. Nevertheless, [Asher et al., 2004] estimated the increase of the heat transfer velocity due to the diffusion as lower than 20%. Therefore, this process can not explain the total deviation.

Furthermore, the decay method assumes the surface renewal model is correctly describing the underlying physical processes. The function resulting from the simulation based on this model and assuming a Gaussian shaped laser profile (equation 4.13) did not explain the measured data and equation 4.13 could not be fitted to the measured curves. Therefore, the underlying processes influencing the temporal decrease of the temperature as well as the assumptions used to determine the shape of the decay curves have to be investigated in future studies.
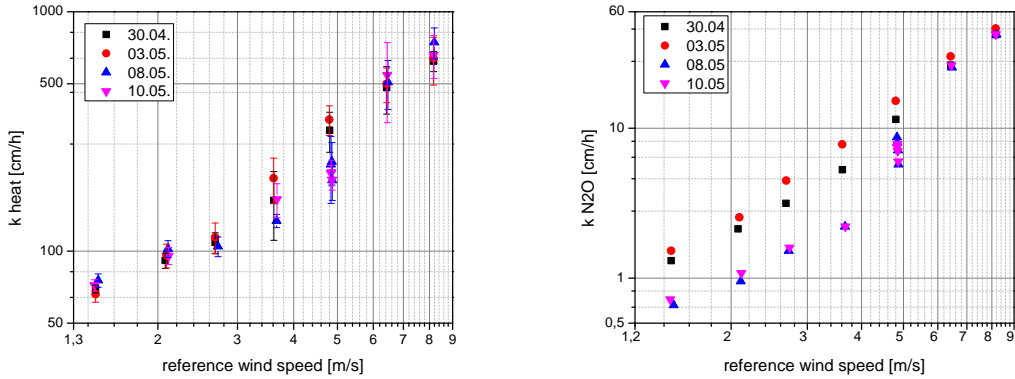
Figure 6.18.: Measured transfer velocity of heat (left) and nitrous oxide (right) over the wind speed for the measurements in the Aeolotron in 2013. The different measurement days correspond to different types and concentrations of surfactants.

Spatial Behaviour of Amplitude and Phase

When the measurements in the Aeolotron in 2013 were conducted the data analysis of the measurements in Marseille in 2012 was not completed. Therefore, the recommendations to improve the measurements for the analysis with the investigation of the spatial behaviour of amplitude and phase, given in section 6.2.1 were not implemented and the measurements were conducted in the same way as in Marseille. Therefore, the above described sources of errors are still present and the recommendations should still be considered for future measurements.

The numerical values of the calculated transfer velocities can be found in the appendix A.3.2. Figure 6.20 shows the comparison of the obtained heat transfer velocities with the preliminary gas transfer rates of N$_2$O, scaled to Schmidt number $Sc = 7$. There are still uncertainties for each measured data point. Nevertheless, it can clearly be seen, that the heat transfer rates overestimate the gas transfer rates for nearly all conditions. Only for wind speeds higher than $u_{10} = 10 \frac{m}{s}$ the values are in coincidence with the gas transfer rates within the range of the errors. For medium wind speeds in the range of $u_{10} = 4 - 10 \frac{m}{s}$ the deviation is close to the factor two. A more precise factor can not be given due to the big uncertainties in the estimation of the heat transfer rates. For the surfactant covered conditions at lower wind speeds, the heat transfer rates overestimate the gas transfer about significantly more than a factor of two.

Although the sensibility study of this analysis method is still outstanding, the method does not seem to work reliable at lower and medium wind speeds. One possible explanation is that for a surfactant covered surface the surface renewal model maybe does not hold any more. At higher wind speeds the influence of surfactants on the heat exchange processes diminishes due to the upcoming of waves breaking the water surface, rupturing the surface film. Further studies are necessary to validate this assumption and to verify the limitations of this analysis method based on the surface renewal model. This future study will help to understand the underlying turbulent processes in the thermal boundary layer. Although the reason of the deviations at lower wind speeds is not fully understood yet, the behaviour of both methods compared to each other is the same as for the measurements in the Marseille wind wave facility.
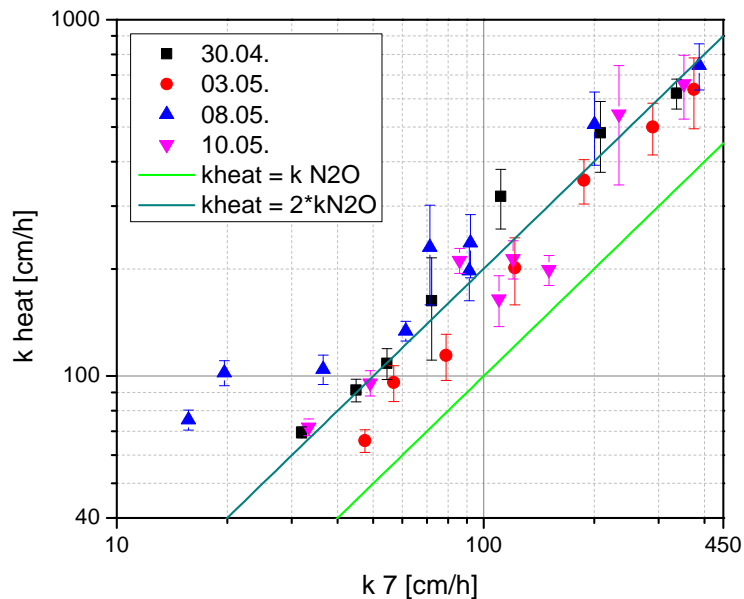
Figure 6.19.: Measured heat transfer velocities determined with the decay curve method in comparison with measured and scaled transfer rates for N_2O - preliminary data provided by Kerstin Krall.

Comparison of Both Analysis Methods
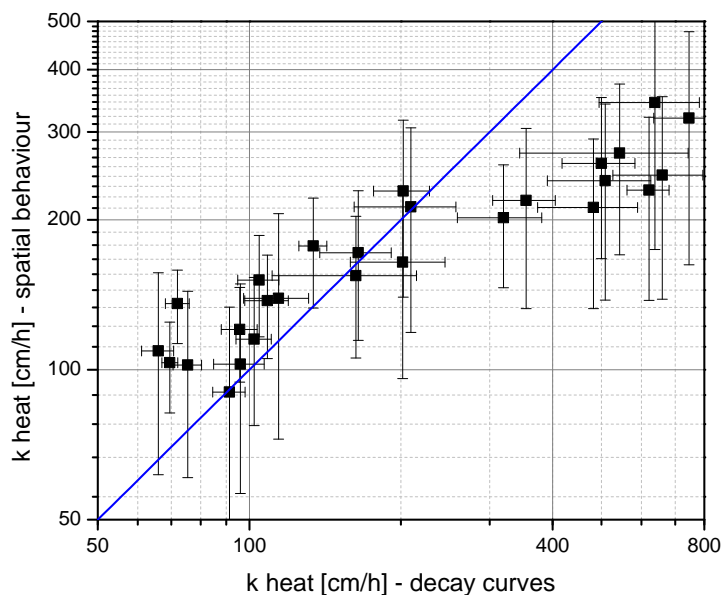
Figure 6.21.: Comparison of the heat transfer rates determined with two different analysis methods for the measurements in the Aeolotron in 2013.
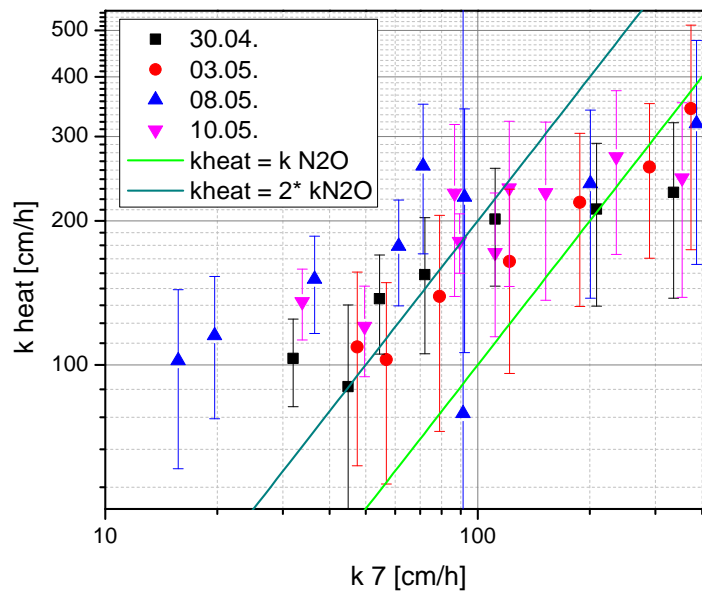
Figure 6.20.: Measured heat transfer velocities determined by the investigation of the spatial behaviour of amplitude and phase in comparison with measured and scaled transfer rates for N_2O - preliminary data provided by Kerstin Krall.

Although both analysis methods show disagreements between the measured heat and (preliminary) gas transfer rates, a comparison between both methods is shown in figure 6.21. For low transfer velocities, corresponding to low wind speeds the transfer rates determined by the investigation of the spatial behaviour of amplitude and phase are significantly larger than the one determined with the decay method. This behaviour turns at medium transfer rates, corresponding to medium wind speeds, while for higher transfer velocities at higher wind speeds the decay curve analysis leads to higher heat transfer velocities.

6.2.3. Comparison of the Measurements

The wind-wave facilities in Marseille and Heidelberg are describe in section 5.2. Due to the fact that the Heidelberg Aeolotron is an annular and the Marseille Phytheas a liner facility, the measurements conducted in both facilities differ in the fetch dependency and the wind speeds in ten meters height. Two analysis methods were used to evaluate the data from the measurements in Marseille and the Aeolotron measurements 2013, the investigation of the spatial behaviour of amplitude and phase and the decay curve method. As described in section 6.2 both methods show deviations compared to directly measured and scaled gas transfer velocities. Furthermore the two analysis methods do not lead to identical results.

To investigate whether or not the shape of the different wind-wave facilities has an influence on the inequality between both analysis methods, figure 6.22 show a comparison between both analysis methods for both facilities. The green line illustrates where both analysis methods lead to the same result. Apparently the difference between the analysis method coincides for both facilities. Both measurements show the same behaviour. From this can be concluded that the shape of the flume does not influence the difference found between the two analysis methods. Furthermore it eliminates sources form mistakes, for example in calibration, which was remade
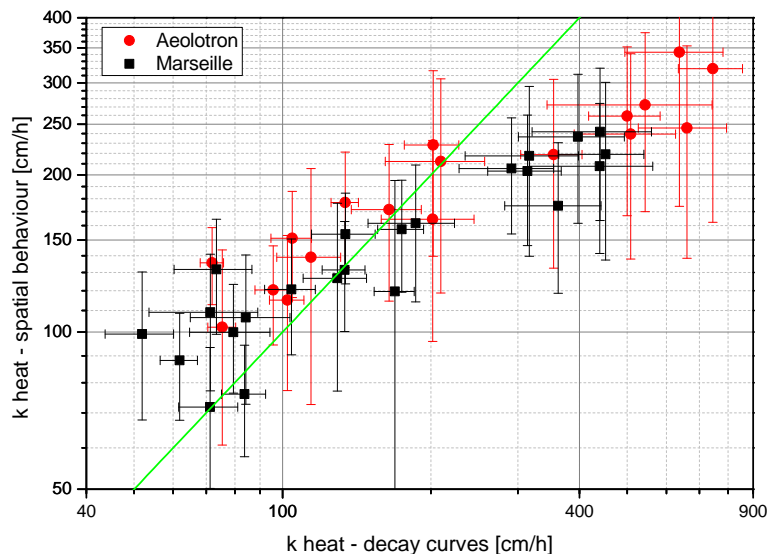
Figure 6.22.: Comparison of the heat transfer rates determined with the investigation of the spatial behaviour of amplitude and phase and with the decay curve method for the measurements in Marseille in 2012 and in the Aeolotron in 2013.

for each campaign or during the measurements, which could create a deviation. Therefore a systematic deviation can be assumed. Most likely the reason will be found in the different analysis methods themselves and need to be investigated in future studies. It is possible that the assumptions about the physics of the exchange process made in the development of these analysis methods are not valid or are oversimplifying the processes.

To investigate the influence of different parameters on the the air-sea interaction a comparison between both facilities is shown. As the deviation between the heat transfer rates and the directly measured gas transfer rates are smaller for the decay curve method (about a factor of two) than for the analysis of the spatial behaviour of amplitude and phase, only the results obtained with the decay curve method are shown here. For a direct comparison of the heat transfer rates, measured in the different facilities three different parameters are available: the wind speed in ten meters height u_{10}, the friction velocity u_* and the mean square slope σ^2. For the measurements conducted in Marseille all three parameters are provided by Guillemette Caulliez, Mediterranean Institute of Oceanography, Marseille-Luminy. A detailed description of the properties of wave field in this flume is for example given in [Caulliez and Guérin, 2012]. The values are given for fetches, which are close to the one used during the measurements in 2012 (2 m, 4 m, 9 m and 26.2 m). As the differences to the fetches used in the measurements compared to the given ones are in the same order as the dimensions of the measurements area no significant error is made. The used values are given in the appendix A.3.1. For the measurements conducted in Heidelberg u_{10} was calculated as described in section 5.2.1, u_* was provided by Maximilian Bopp and σ^2 by Daniel Kiefhaber and Svenja Reith. However, all these data from the Aeolotron measurements are still under processing and therefore are only preliminary results. Figure 6.23 shows the heat transfer rates measured in Marseille and Heidelberg against three different parameters. Under the assumption that the errors in the analysis method do influence both measurements in the same way the behaviour of the heat transfer rates with these different parameters can be investigated.
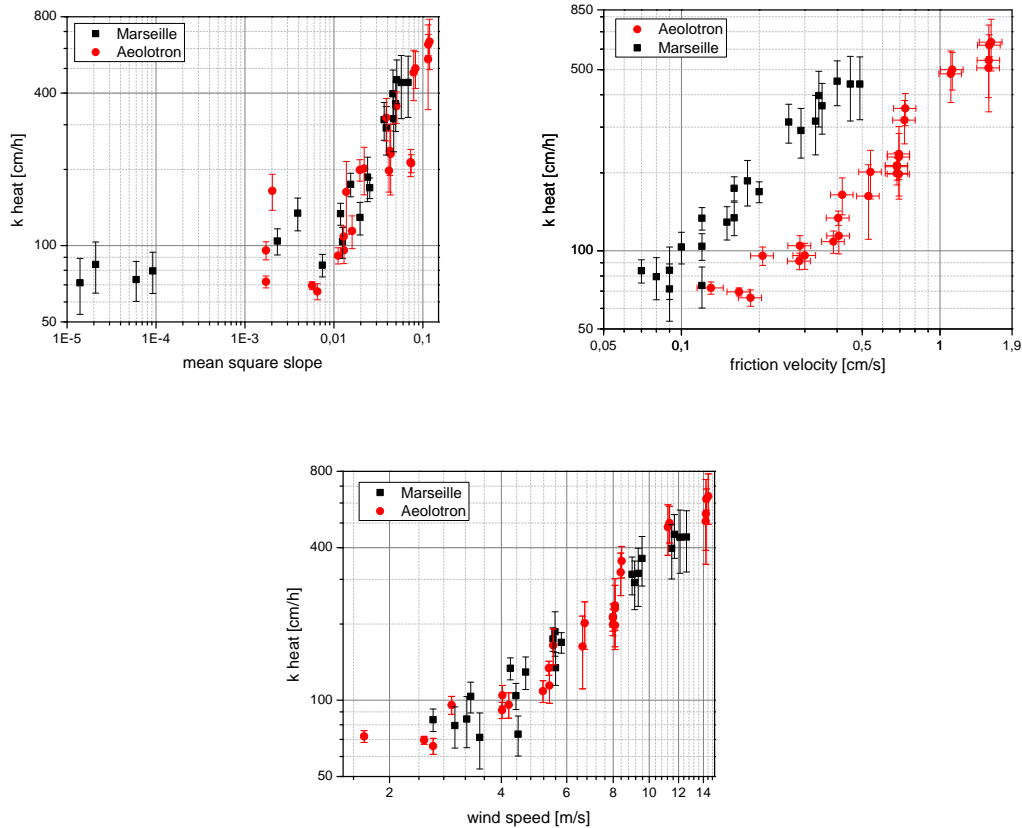
Figure 6.23.: Heat transfer rates determined with the decay curve method for the measurements conducted in Marseille in 2012 and in Heidelberg in 2013 against the wind speed in ten meters height, the friction velocities and the mean square slope.

The parametrisation of the transfer velocities with the mean square slope is in good accordance for both facilities. Using the friction velocity as parameter the measurements differ significantly between the different wind-wave tanks. A possible reason is the different geometric shapes of the wind-wave flumes, as the shape influences currents and turbulences. Another possible reason are the surfactants used in the Aeolotron measurements, which are maybe not influencing the friction velocity, but the near-surface turbulence and waves.

The wind speed for the Aeolotron measurements is calculated with the help of the drag coefficient (see section 5.2.1) out of the friction velocity. It is not clear why the measurements conducted in the different facilities are in good accordance when they are parametrised with the wind speed instead of the friction velocity. A possible reason is, that the calculation of the wind speed is erroneous as the injected surfactant alter the drag coefficient. This effect could balance the deviation found in the comparison with the friction velocity by chance.

6.3. Comparison of Different Analysis Methods

As in earlier discussions (see section 4.5) the results shown in the last sections were obtained by different analysis methods. This section will summarize the advantages and drawbacks of all these analysis methods.

ΔT Although no results, gained with the ΔT method were shown, it is the most direct way to determine heat transfer rates. However, the ΔT method (see section 4.2) is the only analysis method where the heat flux density, provided by the laser, has to be known. While the laser power can be measured quite easily, it is difficult to distribute it equally over the heated area. If it is not equally distributed, the exact distribution has to be known to assign the correct local flux density to the locally measured temperature increase. For this analysis method, measurements with a heated area are used. To create the heated area the Gaussian shaped laser beam is widened to a line perpendicular to the wind speed and scanned in wind direction. This line still has a Gaussian shape and the heat is unequally distributed. By analysing the scanning signal in the Fourier domain the spatial distribution of the flux density can be estimated. The red line in figure 6.24 shows the results of this analysis for one exemplary infrared sequence conducted in the Aeolotron. In addition the resulting temperature difference ΔT is shown in black. The temperature distribution is broadened due to diffusion. Furthermore, the whole distribution is slightly shifted due to surface drift.
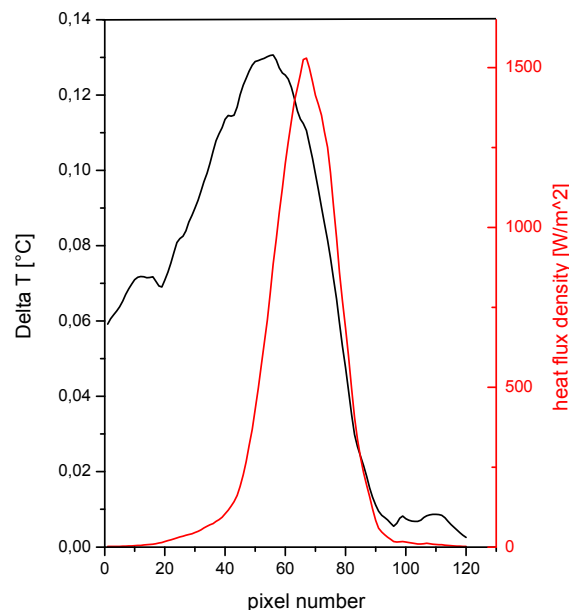
Figure 6.24.: Determined heat flux and measured temperature difference for one exemplary measurement in the Aeolotron.

In addition the absolute temperature difference between heated and unheated areas have to be measured. Therefore, an absolute temperature calibration including the emission of water as well as the influence of reflections of the sky and of the surrounding temperature is necessary (see section 5.1.3).

With the technical preconditions in this work, it was not possible to use the ΔT method to get a reliable determination of the transfer rates. To improve the evaluation it would be necessary to have a laser with a rectangular beam shape for each distance between laser and water surface or to have a scanner, which is fast enough to scan the whole area. As the scanner must be able to resist very high laser power with a diameter of some millimetres, currently no scanning system, which is fast enough, is available.

Amplitude Damping   The amplitude damping method (see section 4.1) is a very robust way to determine transfer rates without the need of any knowledge about laser power or the size of the heated area. However, the size of the heated patch must be big enough to reach a temperature

equilibrium (see section 4.2). The analysis of the frequency dependent signals in the Fourier domain reduces the influence of disturbances like the noise of the camera or reflections, as they are typically not occurring with the frequencies the measurement system is using.

To determine the response time of the system, measurements with different frequencies have to be conducted. Because of this different forcing frequencies, the measurement time is in the order of 20 to 30 minutes. This time resolution is sufficient to determine transfer rates under laboratory conditions and under the encountered field conditions. However, if there are surfactants, which are not equally distributed, but patchy and for a detailed study of the mechanisms influencing air sea gas exchange, this temporal resolution is too low. The spatial resolution is in the order of 15 cm. Although the transfer rates could be determined model independent, a surface renewal approach was chosen for the data analysis, but as described in section 4.1 the difference between the different model assumptions is very small and can not be resolved by the actual accuracy of the measurements.

Decay Curves For the analysis with the help of the decay curves (see 4.3) it is important that the frame rate of the infrared camera is quite high to obtain enough images until the heated patch is cooled down to the water temperature. Additionally the measuring time has to be significantly longer than the response time of the system. Otherwise all decay curves have the same shape (see [Haußecker, 1996]). Furthermore, the shape of the fitted decay curve depends on the gas exchange model assumption. Typically a surface renewal approach is used. A high temporal resolution in the order of 10 s can be reached for this method. The spatial resolution is in the order of 10 cm.

The measurements conducted in Marseille in 2012 and in Heidelberg in 2013, that were evaluated with the decay curve method show no reliable agreement with directly measured gas transfer rates for N_2O. One possible reason is, that the horizontal diffusion is not included in equation 4.13. To be able to rely on the method the underlying turbulent processes and therefore the shape of the decay curves have to be known.

Fourier Analysis: Spatial Behaviour The determination of transfer rates from the spatial behaviour of amplitude and phase in the Fourier space assumes the surface renewal model (see section 4.4). Therefore, no distinction between the different gas transfer models can be made. The temporal resolution is high as only one image sequence with an integration time of about 10 s is necessary to determine a transfer rate. Furthermore, as the analysis is done in the Fourier domain, reflections, as for example from the camera itself or from the sky or the ship, are unproblematic.

This method was tested for the first time in this work. Some recommendations for further measurements with this method can be given: the heated lines should have larger distances and the height of the water surface should be measured and corrected for. However, these first tests did not result in a reliable estimation of the heat transfer velocity in comparison to directly measured gas transfer rates. Further investigations of the turbulent processes influencing the air-sea gas exchange are necessary to use this evaluation method to analyse thermographic measurements reliably.

7. Conclusion and Outlook

Since the last decade, the usability of heat as a proxy tracer for gas transport across the air-sea interface was under discussion. By joined measurements in the Aeolotron wind-wave facility this thesis found a good agreement between the scaled heat transfer rates and the directly measured gas transfer rates for nitrous oxide (see section 6.1.1). The measurements presented in this thesis are in good accordance with the early measurements by [Libner, 1987] and [Jähne et al., 1989], which were investigated with the same analysis methods. Figure 7.1 shows a comparison of the measured heat and gas transfer rates for this early measurements and the data measured in the Aeolotron in 2010.
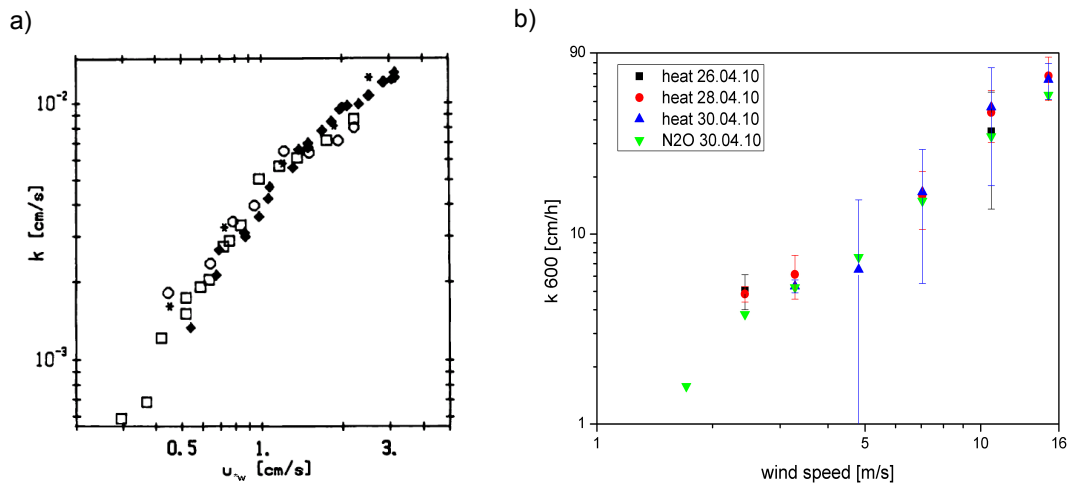
Figure 7.1.: Comparison of heat and gas transfer velocities. a) early data from [Jähne et al., 1989], oxygen (solid diamand) compared with heat (all other sysmbols) transfer rates. b) nitrous oxide (green) compared with heat transfer rates (all other colours) measured in the Aeolotron in 2010.

Additionally this measurements showed that the Schmidt number exponent n is an important factor for the scaling. In laboratory measurements previous works showed that a smooth transition from $n = \frac{2}{3}$ for a smooth surface to $n = \frac{1}{2}$ for a rough surface exists (see for example [Jähne, 1980], [Nielsen, 2004] or [Richter and Jähne, 2011]). The comparison between heat and gas transfer rates is very sensitive to this Schmidt number exponents. It was shown that an improper choice of the Schmidt number exponent can alter the resulting transfer rates by up to a factor of two.

For field studies measured Schmidt number exponents are very rare. Due to this lack of data, except for very low wind speeds or high surfactant coverage under most field conditions a rough surface is commonly assumed. As no measured Schmidt number exponents are available, for the conducted measurements in the Baltic Sea a Schmidt number exponent of $n = \frac{1}{2}$ was also assumed. The scaled heat transfer rates measured in the Baltic Sea show a very good agreement with empiric wind speed parametrisations for the transfer of carbon dioxide (see section 6.1.2).

But the results show also the limitations of the active controlled flux technique used to measure heat transfer rates. As the measurements were conducted onboard moving ships, the heated patch could only be recorded with the infrared camera for a specific time until it moved out of the field of view. When this time is shorter than the response time of the heat transfer process, a determination of the transfer velocity is not possible (see section 6.1.2).

For very high wind speeds, bubble mediated gas transfer influences the transfer of carbon dioxide (and other, especially low soluble gases). The ACFT does not detect the bubble mediated gas transfer (see section 6.1.2). For that reason, in the presence of bubbles the scaled heat transfer rates are lower than the empiric gas transfer parametrisations. This can be used in further studies to determine the contribution of bubbles to the total gas transfer velocity by combined heat and gas transfer measurements. For medium wind speed regimes and for most laboratory conditions the comparing measurements show, that heat, can be used as a proxy tracer for gas transfer, provided that the data is analysed with a suitable analysis method. Furthermore in the framework of this thesis, the active controlled flux technique with an amplitude damping analysis was successfully deployed under field conditions during three ship cruises in the Baltic Sea for the first time. The obtained heat transfer rates measured at the same location show a big scatter at identical wind speeds (see section 6.1.2). This indicated that in addition to the wind speed other parameters influence the air-sea gas exchange.

This shows, that the active thermography is a valuable tool to investigate the small-scale air-sea transport processes, as it has a high spatial and temporal resolution in comparison to other field measurement techniques and can be used both, in the laboratory and in the field (see section 6.3). The amplitude damping analysis was shown to be a robust method to determine heat transfer rates under a wide range of different conditions in laboratory and field. It is insensitive to noise and reflection at the water surface as the analysis is conducted in the Fourier space, as only the forcing frequencies are analysed. However the temporal resolution is 20-30 minutes, what is rather long for thermographic measurements. Although this resolution is sufficient for many applications, for a detailed process study, a temporal resolution in the order of the response time of the system of some seconds would be desirable.

Therefore three faster analysis methods were tested in addition to the amplitude damping method:

- ΔT-Method

- Decay Curves

- Analysis of the Spatial Behaviour of Amplitude and Phase in the Fourier Domain

The ΔT method was found to be most demanding, as an absolute temperature calibration is necessary. For field measurements additional corrections for the reflections of the sky are essential. Furthermore high technical requirements exist as the laser irradiation has to be equally distributed across the heated patch.

The decay curve method as well as the investigation of the spatial behaviour of amplitude and phase are based on the surface renewal model. They were tested on data obtained during two campaigns in Heidelberg and Marseille. In comparison between directly measured gas transfer rates and scaled heat transfer rates deviations were found. As the results of the two quite different facilities are in good agreement, this cannot be due to erroneous measurements but rather to deficits of the applied method itself. First, a surface renewal model with a Schmidt number exponent n= 1/2 is the base of the decay curve method. The measured Schmidt number

exponents show, however, a transition from 2/3 to 1/2. Second, the underlying model is one-dimensional in vertical direction, assuming horizontal homogeneity. This neglects the effects of horizontal molecular and turbulent diffusion and the effects of the shear flow in the heat boundary layer.

Nevertheless, for the investigation of the spatial behaviour of amplitude and phase, the measurements led to recommendations for future measurements, which will improve the data analysis: Larger distances between the heated lines will improve the determination of the slopes of amplitude and phase. Furthermore, combined wave height measurements will improve the determination of the surface drift velocity. A more detailed study of the underlying turbulent processes is required as well as the development of an analysis method with less restrictive assumptions.

Another type of future measurements are worthwhile, as the combined measurements in the Aeolotron compared a local method (ACFT) with a footprint of $50 \times 50\,\text{cm}$ with a global method (mass balance), integrating over the whole facility. Due to the annular shape, the fetch is virtually unlimited and the wave field reaches an equilibrium. Therefore the uncertainties introduced when comparing local and global measurements should be rather small. Nevertheless the wind generators or built-in measurement devices can affect the wind field locally (see [Bopp, 2014]). To achieve these further measurements a method, which measures gas exchange rates locally is necessary.
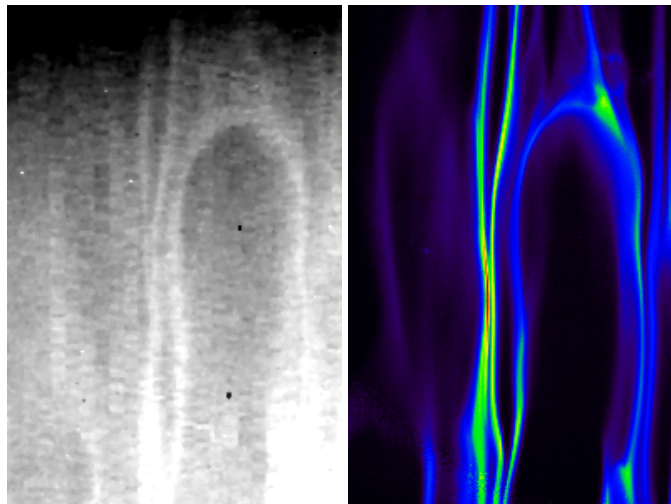
Figure 7.2.: Simultaneous grabbed infrared image and visualization of the boundary layer thickness at a wind speed of about $2\,\frac{\text{m}}{\text{s}}$ in a small test wind wave facility in Heidelberg - images provided by Christine Kräuter.

A two-dimensional resolved measurement technique of the boundary layer thickness with a footprint comparable to that of the ACFT is under construction in the Aeolotron by Christine Kräuter, [Kräuter et al., 2013]. This method enables a two dimensional visualisation of the gas exchange of ammonia.

Passive infrared images taken from the water surface show a typical pattern, determined by turbulent eddies penetrating the boundary layer. To enable a scaling of measured heat and gas transfer velocities, the turbulent processes disturbing the boundary layer have to be identical, despite of the difference of two orders of magnitude in the boundary layer thickness. Therefore the observed structures in the infrared image and the imaging of the gas exchange structures have to be identical..

Figure 7.2 shows an image obtained with this method in comparison with a simultaneously acquired infrared image of the same patch of about $7 \times 4\,\mathrm{cm}$ of the water surface. The images were conducted in a small test wind wave facility in Heidelberg at a wind speed of about $u_{10} = 2\,\frac{\mathrm{m}}{\mathrm{s}}$. Although the lower resolution and the inaccurate calibration of the infrared camera leads to disturbances in the infrared images, same surface structures are found in both images. This indicates that heat and gas transfer are, despite the large difference in molecular diffusivities, governed by the same mechanisms. This was doubted by some previous work (see section 4.5). This finding is another strong indication that it is possible to infer gas transfer rates from heat transfer measurements by active thermography, provided the Schmidt number exponent is known.

Systematic measurements, using an infrared camera with a higher resolution are planned. This measurements will be the first combined local and simultaneously measurement of wind induced heat and gas transfer and will investigate the scaling between both.

The continuation and refinement of the methods explored in this thesis, as well as the combination with local gas exchange measurements will improve the physical understanding and aid in developing a physics-based model of gas transfer.

Bibliography

W. E. Asher, A. T. Jessup, and M. A. Atmane. Oceanic application of the active controlled flux technique for measuring air-sea transfer velocities of heat and gases. *J. Geophys. Res.*, 109: C08S12, 2004. doi: 10.1029/2003JC001862.

M. A. Atmane, W. Asher, and A. T. Jessup. On the use of the active infrared technique to infer heat and gas transfer velocities at the air-water free surface. *J. Geophys. Res.*, 109:C08S14, 2004. doi: doi:10.1029/2003JC001805.

M. Aubinet, T. Vesala, and D. Papale. *Eddy Covariance: A Practical Guide to Measurement and Data Analysis*. Springer Atmospheric Sciences. Springer, 2012. ISBN 9789400723504. URL http://books.google.de/books?id=8a2bIJER5ZwC.

M. L. Banner and O. M. Phillips. On the incipient breaking of small-scale waves. *Journal of Fluid Mechanics*, 65:647–656, 1974.

M. Bopp. Messung der Schubspannungsgeschwindigkeit am Heidelberger Aeolotron mittels der Impulsbilanzmethode. Bachelor thesis, Institut für Umweltphysik, Fakultät für Physik und Astronomie, Univ. Heidelberg, 2011.

M. Bopp. Luft- und wasserseitige Strömungsverhältnisse im ringförmigen Heidelberger Wind/Wellen-Kanal (Aeolotron). Master's thesis, Institut für Umweltphysik, Fakultät für Physik und Astronomie, Univ. Heidelberg, 2014.

G. Caulliez and C.-A. Guérin. Higher-order statistical analysis of short wind wave fields. *J. Geophys. Res.*, 117(C6):C06002–, June 2012. ISSN 0148-0227. URL http://dx.doi.org/10.1029/2011JC007854.

P. Ciais, C. Sabine, G. Bala, L. Bopp, V. Brovkin, J. Canadell, A. Chhabra, R. DeFries, J. Galloway, M. Heimann, C. Jones, C. L. Quéré, R. Myneni, S. Piao, and P. Thornton. *Climate Change 2013: The Physical Science Basis. Contribution of Working Group I to the Fifth Assessment Report of the Intergovernmental Panel on Climate Change*, chapter Carbon and Other Biogeochemical Cycles. Cambridge University Press, Cambridge, United Kingdom and New York, NY, USA, 2013.

M. Coantic. A model of gas transfer across air–water interfaces with capillary waves. *Journal of Geophysical Research*, 91:3925–3943, 1986. doi: 10.1029/JC091iC03p03925.

M. Coantic and P. Bonmarin. The air-sea interaction simulation facility at the Institut de Mecanique Statistique de la Turbulence. *Atmospheric Technology*, (7):72–79, 1975.

B. Ćosović and V. Vojvodić. Voltammetric analysis of surface active substances in natural seawater. *Electroanalysis*, 10(6):429–434, 1998. ISSN 1521-4109. doi: 10.1002/(SICI)1521-4109(199805)10:6<429::AID-ELAN429>3.0.CO;2-7. URL http://dx.doi.org/10.1002/(SICI)1521-4109(199805)10:6<429::AID-ELAN429>3.0.CO;2-7.

P. V. Danckwerts. Significance of a liquid-film coefficients in gas absorption. *Ind. Eng. Chem.*, 43:1460–1467, 1951. doi: 10.1021/ie50498a055.

E. L. Deacon. Gas transfer to and across an air-water interface. *Tellus*, 29:363–374, 1977. doi: 10.1111/j.2153-3490.1977.tb00746.x.

E. L. Dereniak and G. D. Boreman. *Infrared Detectors and Systems.* Wiley-Interscience, 1996.

H. D. Downing and D. Williams. Optical constants of water in the infrared. *Journal of Geophysical Research*, 80(12):1656–1661, 1975.

Erdmann. *Experimentalphysik 4: Hydromechanik, Wärme.* Springer, 2011.

C. W. Fairall, E. F. Bradley, J. S. Godfrey, G. A. Wick, and J. B. Edson. Cool-skin and warm-layer effects on sea surface temperature. *Journal of Geophysical Research*, 101(C1):1295–1308, 1996.

R. A. Feely, C. L. Sabine, K. Lee, W. Berelson, J. Kleypas, V. J. Fabry, and F. J. Millero. Impact of anthropogenic CO2 on the CaCO3 system in the oceans. *Science*, 305(5682):362–366, Jul 2004. doi: 10.1126/science.1097329.

N. M. Frew. The role of organic films in air-sea gas exchange. In P. S. Liss and R. A. Duce, editors, *The Sea Surface and Global Change*, pages 121–171. Cambridge University Press, Cambridge,UK, 1997. URL `http://books.google.de/books?hl=en&lr=&id=3yu4XlcFPqUC&oi=fnd&pg=PA121&dq=frew++The+role+of+organic+films+in+air+sea+gas+exchange&ots=cGZ8rnM25u&sig=vUzJrSr9ENPi6nGbEsd7ml1zINM#v=onepage&q&f=false`. 5.

N. M. Frew, J. C. Goldman, M. R. Denett, and A. S. Johnson. Impact of phytoplankton-generated surfactants on air-sea gas-exchange. *Journal of Geophysical Research*, 95(C3):3337–3352, 1990. doi: 10.1029/JC095iC03p03337.

F. Friedl. *Investigating the Transfer of Oxygen at the Wavy Air-Water Interface under Wind-Induced Turbulence.* Dissertation, Institut für Umweltphysik, Fakultät für Physik und Astronomie, Univ. Heidelberg, 2013. URL `http://archiv.ub.uni-heidelberg.de/volltextserver/14582/`.

C. S. Garbe. *Measuring Heat Exchange Processes at the Air–Water Interface from Thermographic Image Sequence Analysis.* Dissertation, IWR, Fakultät für Physik und Astronomie, Univ. Heidelberg, Heidelberg, Germany, 2001. URL `http://www.ub.uni-heidelberg.de/archiv/1875`.

C. S. Garbe, U. Schimpf, and B. Jähne. A surface renewal model to analyze infrared image sequences of the ocean surface for the study of air-sea heat and gas exchange. *Journal of Geophysical Research-Oceans*, 109(C8):1–18, 2004. ISSN 0148-0227. doi: doi:10.1029/2003JC001802.

C. S. Garbe, A. Rutgersson, J. Boutin, B. Delille, C. W. Fairall, N. Gruber, J. Hare, D. Ho, M. Johnson, G. de Leeuw, P. Nightingale, H. Pettersson, J. Piskozub, E. Sahlee, W. Tsai, B. Ward, D. K. Woolf, and C. Zappa. Transfer across the air-sea interface. In P. S. Liss and M. T. Johnson, editors, *Ocean-Atmosphere Interactions of Gases and Particles*, pages 55–112. Springer, 2014. doi: 10.1007/978-3-642-25643-1_2.

B. Gašparović, M. Plavšić, B. Ćosović, and A. Saliot. Organic matter characterization in the sea surface microlayers in the subarctic norwegian fjords region. *Marine Chemistry*, 105(1-2): 1–14, 2007. doi: http://dx.doi.org/10.1016/j.marchem.2006.12.010. URL http://www.sciencedirect.com/science/article/pii/S0304420306002167.

C. Haltebourg. *Spatiotemporal Modelling of Active Thermography*. Dissertation, Institut für Umweltphysik, Fakultät für Physik und Astronomie, Univ. Heidelberg, 2014. in preparation.

P. Harriott. A random eddy modification of the penetration theory. *Chem. Eng. Sci.*, 17:149–154, 1962.

H. Haußecker. *Messung und Simulation von kleinskaligen Austauschvorgängen an der Ozeanoberfläche mittels Thermographie*. Dissertation, IWR, Fakultät für Physik und Astronomie, Univ. Heidelberg, 1996.

H. Haußecker and B. Jähne. In situ measurements of the air-sea gas transfer rate during the MBL/CoOP west coast experiment. In B. Jähne and E. C. Monahan, editors, *Air-Water Gas Transfer - Selected Papers from the Third International Symposium on Air-Water Gas Transfer*, pages 775–784, Heidelberg, 1995. AEON Verlag & Studio Hanau.

A. Herzog. *Imaging of Water-sided Gas-Concentration Fields at a Wind-Driven, Wavy Air-Water Interface*. Dissertation, Institut für Umweltphysik, Fakultät für Physik und Astronomie, Univ. Heidelberg, 2010. URL http://www.ub.uni-heidelberg.de/archiv/11220.

R. Higbie. The rate of absorption of a pure gas into a still liquid during short periods of exposure. *Trans. Am. Inst. Chem. Eng.*, 31:365–389, 1935.

D. T. Ho, R. Wanninkhof, P. Schlosser, D. S. Ullman, D. Hebert, and K. F. Sullivan. Toward a universal relationship between wind speed and gas exchange: Gas transfer velocities measured with 3he/sf6 during the southern ocean gas exchange experiment. *Journal of Geophysical Research*, 116, 2011. doi: 10.1029/2010JC006854.

T. E. Hoover and D. C. Berkshire. Effects of hydration on carbon dioxide exchange across an air-water interface. *J.Geophys.Res.*, 74(2):456–464, 1969.

IPCC. *Climate Change 2007: The Physical Science Basis. Contribution of Working Group I to the Fourth Assessment Report of the Intergovernmental Panel on Climate Change*. Cambridge University Press, Cambridge, United Kingdom and New York, NY, USA, 2007. URL http://www.ipcc.ch/.

A. T. Jessup, W. E. Asher, M. Atmane, K. Phadnis, C. J. Zappa, and M. R. Loewen. Evidence for complete and partial surface renewal at an air-water interface. *Geophys. Res. Lett.*, 36: 1–5, Aug. 2009. doi: 10.1029/2009GL038986.

B. Jähne. *Zur Parametrisierung des Gasaustauschs mit Hilfe von Laborexperimenten*. Dissertation, Institut für Umweltphysik, Fakultät für Physik und Astronomie, Univ. Heidelberg, 1980. URL http://d-nb.info/810123614. IUP D-145.

B. Jähne. *Transfer processes across the free water interface*. Habilitation thesis, Institut für Umweltphysik, Fakultät für Physik und Astronomie, Univ. Heidelberg, 1985. IUP D-200.

B. Jähne. Air-sea gas exchange. In J. H. Steele, K. K. Turekian, and S. A. Thorpe, editors, *Encyclopedia Ocean Sciences*, pages 3434–3444. Elsevier, 2009. doi: 10.1016/B978-012374473-9.00642-1. invited.

B. Jähne. *Digitale Bildverarbeitung und Bildgewinnung*. Springer, Berlin, 2012.

B. Jähne, K. O. Münnich, R. Bösinger, A. Dutzi, W. Huber, and P. Libner. On the parameters influencing air-water gas exchange. *J. Geophys. Res.*, 92:1937–1950, Feb. 1987. doi: 10.1029/JC092iC02p01937.

B. Jähne, P. Libner, R. Fischer, T. Billen, and E. J. Plate. Investigating the transfer process across the free aqueous boundary layer by the controlled flux method. *Tellus*, 41B(2):177–195, 1989. doi: 10.1111/j.1600-0889.1989.tb00135.x.

B. Jähne, H. Haußecker, U. Schimpf, and G. Balschbach. The Heidelberg Aeolotron - a new facility for laboratory investigations of small scale air-sea interaction. In *Poster presented at: The Wind-Driven Air-Sea Interface: Electromagnetic and Acoustic Sensing, Wave Dynamics and Turbulent Fluxes*, Sydney, Australia, 1999.

D. Kiefhaber. Development of a reflective stereo slope gauge for the measurement of ocean surface wave slope statistics. Diplomarbeit, Institut für Umweltphysik, Fakultät für Physik und Astronomie, Univ. Heidelberg, 2010. URL `http://www.ub.uni-heidelberg.de/archiv/12673/`.

D. Kiefhaber. *Optical Measurement of Short Wind Waves - from Laboratory to the Field*. PhD thesis, Institut für Umweltphysik, Fakultät für Physik und Astronomie, Univ. Heidelberg, 2014.

D. Kiefhaber, R. Rocholz, and B. Jähne. Improved optical instrument for the measurement of water wave statistics in the field. In S. Komori, W. McGillis, and R. Kurose, editors, *Gas Transfer at Water Surfaces 2010*, pages 524–534, 2011.

D. Kiefhaber, S. Reith, R. Rocholz, and B. Jähne. High-speed imaging of short wind waves by shape from refraction. *J. Eur. Opt. Soc.-Rapid*, 2014. accepted for publication.

A. S. Kowalski and P. Serrano-Ortiz. On the relationship between the eddy covariance, the turbulent flux, and surface exchange for a trace gas such as CO_2. *Boundary-Layer Meteorology*, 124:129–141, 2007. doi: 10.1007/s10546-007-9171-z.

K. E. Krall. *Laboratory Investigations of Air-Sea Gas Transfer under a Wide Range of Water Surface Conditions*. Dissertation, Institut für Umweltphysik, Fakultät für Physik und Astronomie, Univ. Heidelberg, 2013. URL `http://archiv.ub.uni-heidelberg.de/volltextserver/14392/`.

C. Kräuter. Aufteilung des Transferwiderstands zwischen Luft und Wasser beim Austausch flüchtiger Substanzen mittlerer Löslichkeit zwischen Ozean und Atmosphäre. Diplomarbeit, Institut für Umweltphysik, Fakultät für Physik und Astronomie, Univ. Heidelberg, 2011. URL `http://www.ub.uni-heidelberg.de/archiv/13010`.

C. Kräuter, D. Trofimova, D. Kiefhaber, N. Krah, and B. Jähne. High-resolution 2-d fluorescence imaging of the mass boundary layer at free water surfaces. *Journal of the European Optical Society*, 2013. submitted.

C. Le Quéré, G. P. Peters, R. J. Andres, R. M. Andrew, T. Boden, P. Ciais, P. Friedlingstein, R. A. Houghton, G. Marland, R. Moriarty, S. Sitch, P. Tans, A. Arneth, A. Arvanitis, D. C. E. Bakker, L. Bopp, J. G. Canadell, L. P. Chini, S. C. Doney, A. Harper, I. Harris, J. I. House, A. K. Jain, S. D. Jones, E. Kato, R. F. Keeling, K. Klein Goldewijk, A. Körtzinger, C. Koven, N. Lefèvre, A. Omar, T. Ono, G.-H. Park, B. Pfeil, B. Poulter, M. R. Raupach, P. Regnier, C. Rödenbeck, S. Saito, J. Schwinger, J. Segschneider, B. D. Stocker, B. Tilbrook, S. van Heuven, N. Viovy, R. Wanninkhof, A. Wiltshire, S. Zaehle, and C. Yue. Global carbon budget 2013. *Earth System Science Data Discussions*, 6(2):689–760, 2013. doi: 10.5194/essdd-6-689-2013. URL http://www.earth-syst-sci-data-discuss.net/6/689/2013/. under review.

P. Libner. *Die Konstantflußmethode: Ein neuartiges, schnelles und lokales Meßverfahren zur Untersuchung von Austauschvorgängen an der Luft-Wasser Phasengrenze*. Dissertation, Institut für Umweltphysik, Fakultät für Physik und Astronomie, Univ. Heidelberg, Heidelberg, Germany, 1987. URL http://d-nb.info/881465941.

P. S. Liss. Gas transfer: experiments and geochemical implications. In P. S. Liss and W. G. N. Slinn, editors, *Air-Sea Exchange of Gases and Particles*, number 108 in NATO ASI Series, Series C, Mathematical and Physical Sciences, pages 241–298. Reidel, Dordrecht, 1983.

P. S. Liss and M. T. Johnson, editors. *Ocean-Atmosphere Interactions of Gases and Particles*. Springer, 2014. doi: 10.1007/978-3-642-25643-1. URL http://link.springer.com/book/10.1007/978-3-642-25643-1.

P. S. Liss and L. Merlivat. Air-sea gas exchange rates: Introduction and synthesis. In P. Buat-Menard, editor, *The role of air-sea exchange in geochemical cycling*, pages 113–129. Reidel, Boston, MA, 1986.

P. S. Liss and P. G. Slater. Flux of gases across the air-sea interface. *Nature*, 247:181–184, 1974.

L. Memery and L. Merlivat. Modelling of gas flux through bubbles at the air-water interface. *Tellus B*, 37B(4-5):272–285, 1985. doi: 10.1111/j.1600-0889.1985.tb00075.x.

D. Meschede, editor. *Gerthsen Physik*. Springer Verlag Berlin Heidelberg, 23th edition, 2006. doi: 10.1007/3-540-29973-4. URL http://www.springerlink.com/content/wn8495/.

T. Münsterer. *LIF Investigation of the Mechanisms Controlling Air–Water Mass Transfer at a Free Interface*. Dissertation, Institut für Umweltphysik, Fakultät für Physik und Astronomie, Univ. Heidelberg, 1996.

L. Nagel. Bestimmung der Temperaturdifferenz über die viskose Grenzschicht mit Hilfe des Oberflächenerneuerungsmodells. Diplomarbeit, IWR, Fakultät für Physik und Astronomie, Univ. Heidelberg, 2009.

R. Nielsen. *Gasaustausch - Entwicklung und Ergebnis eines schnellen Massenbilanzverfahrens zur Messung der Austauschparameter*. Dissertation, Institut für Umweltphysik, Fakultät für Physik und Astronomie, Univ. Heidelberg, 2004. URL http://www.ub.uni-heidelberg.de/archiv/5032.

P. Nightingale. Air–sea gas exchange. In C. L. Quéré and E. S. Saltzman, editors, *Surface Ocean- Lower Atmosphere Processes*, pages 69–98. American Geophysical Union, 2009.

P. D. Nightingale, G. Malin, C. S. Law, A. J. Watson, P. S. Liss, M. I. Liddicoat, J. Boutin, and R. C. Upstill-Goddard. In situ evaluation of air-sea gas exchange parameterization using novel conservation and volatile tracers. *Glob. Biogeochem. Cycles*, 14:373–387, 2000. doi: 10.1029/1999GB900091.

R. Patro, I. Leifer, and P. Bowyer. Better bubble process modeling: Improved bubble hydrodynamics parameterization. In M. A. Donelan, W. M. Drennan, E. S. Saltzman, and R. Wanninkhof, editors, *Gas Transfer at Water Surfaces*, volume 127 of *Geophysical Monograph*, pages 315–320, 2002.

C. J. Popp. *Untersuchung von Austauschprozessen an der Wasseroberfläche aus Infrarot-Bildsequenzen mittels frequenzmodulierter Wärmeeinstrahlung*. Dissertation, Institut für Umweltphysik, Fakultät für Physik und Astronomie, Univ. Heidelberg, 2006. URL http://www.ub.uni-heidelberg.de/archiv/6489.

J. A. Quinn and N. C. Otto. Carbon dioxide exchange at the air-sea interface: Flux augmentation by chemical reaction. *J.Geophys.Res.*, 76(6):1539–1549, 1971.

H. Reichardt. Vollständige Darstellung der turbulenten Geschwindigkeitsverteilung in glatten Leitungen. *Zeitschrift für angewandte Mathematik und Mechanik*, 31:208–219, 1951.

S. Reinelt. Bestimmung der Transfergeschwindigkeit mittels CFT mit Wärme als Tracer. Diplomarbeit, Institut für Umweltphysik, Fakultät für Physik und Astronomie, Univ. Heidelberg, 1994.

K. Richter and B. Jähne. A laboratory study of the schmidt number dependency of air-water gas transfer. In S. Komori, W. McGillis, and R. Kurose, editors, *Gas Transfer at Water Surfaces 2010*, pages 322–332, 2011.

R. Rocholz. *Spatiotemporal Measurement of Short Wind-Driven Water Waves*. Dissertation, Institut für Umweltphysik, Fakultät für Physik und Astronomie, Univ. Heidelberg, 2008. URL http://www.ub.uni-heidelberg.de/archiv/8897.

W. Roether and B. Kromer. Optimum application of the radon deficit method to obtain air–sea gas exchange rates. In W. Brutsaert and G. H. Jirka, editors, *Gas transfer at water surfaces*, pages 447–457, Hingham, MA, 1984. Reidel.

E. Sahlee, K. Kahma, H. Pettersson, and W. Drennan. Damping of humidity fluctuations in a closed-path system. In S. Komori, W. McGillis, and R. Kurose, editors, *Gas Transfer at Water Surfaces 2010*, pages 516 – 523, 2011.

P. M. Saunders. The temperature at the ocean-air interface. *Journal of Atmospherical Sciences*, 24(3):269–273, 1967.

U. Schimpf. *Untersuchung des Gasaustausches und der Mikroturbulenz an der Meeresoberfläche mittels Thermographie*. Dissertation, Institut für Umweltphysik, Fakultät für Physik und Astronomie, Univ. Heidelberg, Heidelberg, Germany, 2000.

U. Schimpf, C. Garbe, and B. Jähne. Investigation of transport processes across the sea surface microlayer by infrared imagery. *Journal of Geophysical Research-Oceans*, 109(C8):C08S13, 2004. ISSN 0148-0227. doi: doi:10.1029/2003JC001803.

U. Schimpf, L. Nagel, and B. Jähne. First results of the 2009 sopran active thermography pilot experiment in the baltic sea. In S. Komori, W. McGillis, and R. Kurose, editors, *Gas Transfer at Water Surfaces 2010*, pages 358–367, 2011.

S. D. Smith and E. G. Banke. Variation of the sea surface drag coefficient with wind speed. *Quarterly Journal of the Royal Meteorological Society*, 101:665–673, 1975.

N. Tepić, B. Gašparović, and M. Ahel. Multivariate statistical analysis of the distribution patterns of carbohydrates and surface-active substances in the northern adriatic sea. *Marine Chemistry*, 114:37 – 46, 2009. ISSN 0304-4203. doi: http://dx.doi.org/10.1016/j.marchem. 2009.03.005. URL http://www.sciencedirect.com/science/article/pii/ S0304420309000413.

K. Tsujii. *Surface Activity: Principles, Phenomena and Applications*. Series in polymers, interfaces, and biomaterials. Academic Press Inc, 1998. ISBN 9780127022802. URL http: //books.google.de/books?id=UdNTAAAAMAAJ.

R. Wanninkhof. Relationship between wind speed and gas exchange over the ocean. *J. Geophys. Res.*, 97:7373–7382, 1992. doi: 10.1029/92JC00188.

R. Wanninkhof and W. R. McGillis. A cubic relationship between gas transfer and wind speed. *Geophys. Res. Lett.*, 26:1889–1892, 1999. doi: 10.1029/1999GL900363.

R. Wanninkhof, W. E. Asher, R. Wepperning, C. Hua, P. Schlosser, C. Langdon, and R. Sambrotto. Gas transfer experiment on georges bank using two volatile deliberate tracers. *Journal of Geophysical Research*, 98(C11):20237–20248, 1993.

R. Wanninkhof, W. E. Asher, D. T. Ho, C. Sweeney, and W. R. McGillis. Advances in quantifying air-sea gas exchange and environmental forcing. *Annu. Rev. Mar. Sci.*, 1:213–244, 2009. doi: 10.1146/annurev.marine.010908.163742.

W. G. Whitman. The two-film theory of gas absorption. *Chemical and Metallurgical Engineering*, 29(4):146–148, 1923.

D. Woolf. Bubbles and their role in gas exchange. In P. S. Liss and R. A. Duce, editors, *The sea surface and global change*, chapter 6. Cambridge Univ Press, 1997.

D. Woolf, I. Leifer, P. Nightingale, T. Rhee, P. Bowyer, G. Caulliez, G. de Leeuw, S. Larsen, M. Liddicoat, J. Baker, and M. Andreae. Modelling of bubble-mediated gas transfer: Fundamental principles and a laboratory test. *Journal of Marine Systems*, 66:71–91, 2007. doi: 10.1016/j.jmarsys.2006.02.011.

O. Wurl, L. Miller, and S. Vagle. Production and fate of transparent exopolymer particles in the ocean. *Journal of Geophysical Research*, 116:C00H13, 2011. doi: doi:10.1029/ 2011JC007342.

C. J. Zappa, W. E. Asher, A. T. Jessup, J. Klinke, and S. R. Long. Effect of microscale wave breaking on air-water gas transfer. In E. Saltzman, M. Donelan, W. Drennan, and R. Wanninkhof, editors, *Gas Transfer at Water Surfaces*, volume 127 of *Geophysical Monograph*, pages 23–29. American Geophysical Union, 2002.

C. J. Zappa, W. E. Asher, A. T. Jessup, J. Klinke, and S. R. Long. Microbreaking and the enhancement of air-water transfer velocity. *J. Geophys. Res.*, 109:C08S16, 2004. doi: doi: 10.1029/2003JC001897.

A. Appendix

A.1. Technical Data of the Used Measurement Instruments

This section gives on overview over the technical properties of the different measurement instruments.

A.1.1. Infrared Cameras

For the conducted measurements two different infrared cameras were used. Table A.1 gives an overview over the most important technical properties, which are taken from the manufacturers informations.

manufacturer	Thermosensorik	IRcam
type	CMT 256	Velox 327k
chip	Cadmium-Mercury-Telluride (CMT)	CMT
wave length range $[\mu m]$	3.4 - 5	3.4 - 5.1
number of pixel	256×256	512×640
pixel pitch $[\mu m]$	24	32
maximum framerate [Hz] (full screen)	880	207
maximum framerate [Hz] (partial image)	880	820
integration time [s]	0.05 - 12.75	0.01 - 1.2
NEΔT [mK]	20	20
A/D resolution [bit]	14	14

Table A.1.: Technical data of the used infrared cameras. All data are manufacturer informations.

Table A.2 gives an overview over the available infrared lenses and their properties. Although the lenses were manufactured for the different cameras, they can be used with both cameras.

type	IR M 25	IR M 50	28 mm MWIR	50 mm MWIR	100 mm MWIR
manufacturer	IRcam	IRcam	Thermosenorik	Thermosensorik	Thermosensorik
focal length [mm]	25	50	28	50	100
aperture ratio	F/2	F/2	F/2	F/2	F/2
range [m]	0.1 - ∞	0.1 - ∞	0.1 - ∞	0.5 - ∞	1.5 - ∞

Table A.2.: Technical data of the lenses for the infrared cameras. All lenses can be used for both cameras.

A.1.2. CO$_2$-Laser

The second important part of the ACFT measurement instrument is the CO$_2$-laser. Two different types of lasers have been used. The *Evolution 120* was permanently installed at the Aeolotron and therefore used for the laboratory measurements conducted in Heidelberg (see section 2.2).

All other measurements were conducted with the portable field instrument, where the *Firestar f 200* laser is integrated. Table A.3 gives the technical data of both lasers.

type	Evolution 120	Firestar f 200
manufacturer	Synrad, Inc.	Synrad, Inc.
wavelength $[\mu m]$	12.59	10.2 - 10.7
power output [W]	125	200
power stability [%]	5	6
beam diameter [mm]	4.4	3.5 ± 0.1
beam divergence [mrad]	3.2	4.0 ± 0.2
polarization	linear, vertical	unspecified

Table A.3.: Technical data of the used CO_2-lasers. All data are manufacturer informations.

A.2. Results and Fit Curves of the Amplitude Damping Method

For the measurements in the Aeolotron in 2010 and for all there field measurement campaigns an analysis with the help of the amplitude damping in the Fourier space was conducted (see section 4.1.1). Here all measured damping curves and the associated fit curves are shown. Furthermore the fit values are given.

A.2.1. Laboratory Measurements

During the Aeolotron measurements 2010 heat infrared images were acquired during three different days. Figure A.1, A.2 and A.3 show all measured amplitudes and the fitted damping curves for these measurements.
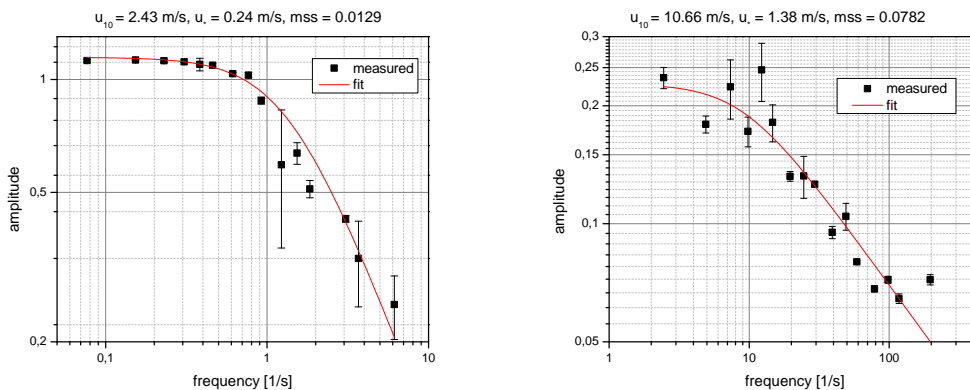
Figure A.1.: Measured amplitude values and fitted damping curves for the measurements conducted in the Aeolotron at 26.04.2010.
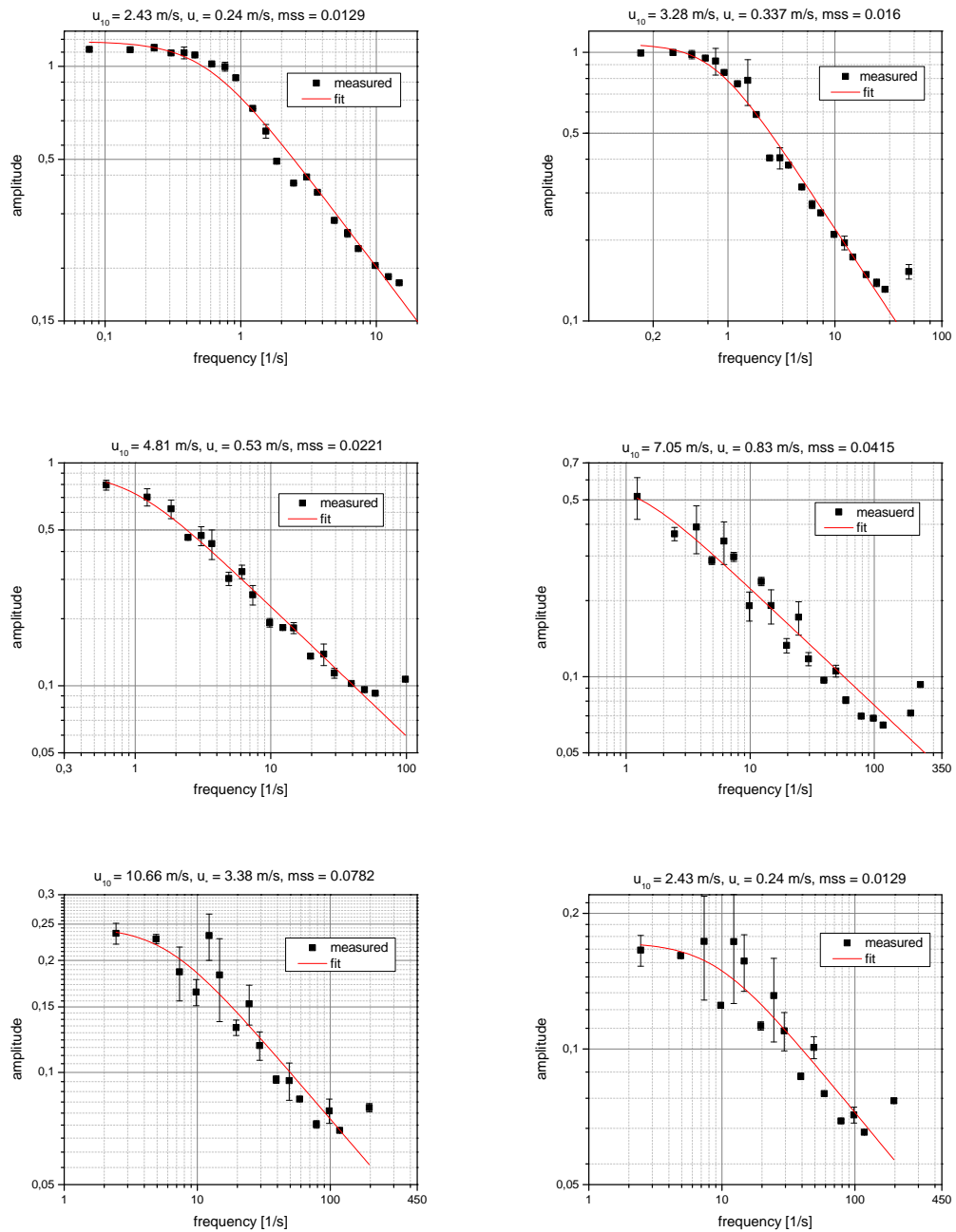
Figure A.2.: Measured amplitude values and fitted damping curves for the measurements conducted in the Aeolotron at 28.04.2010.
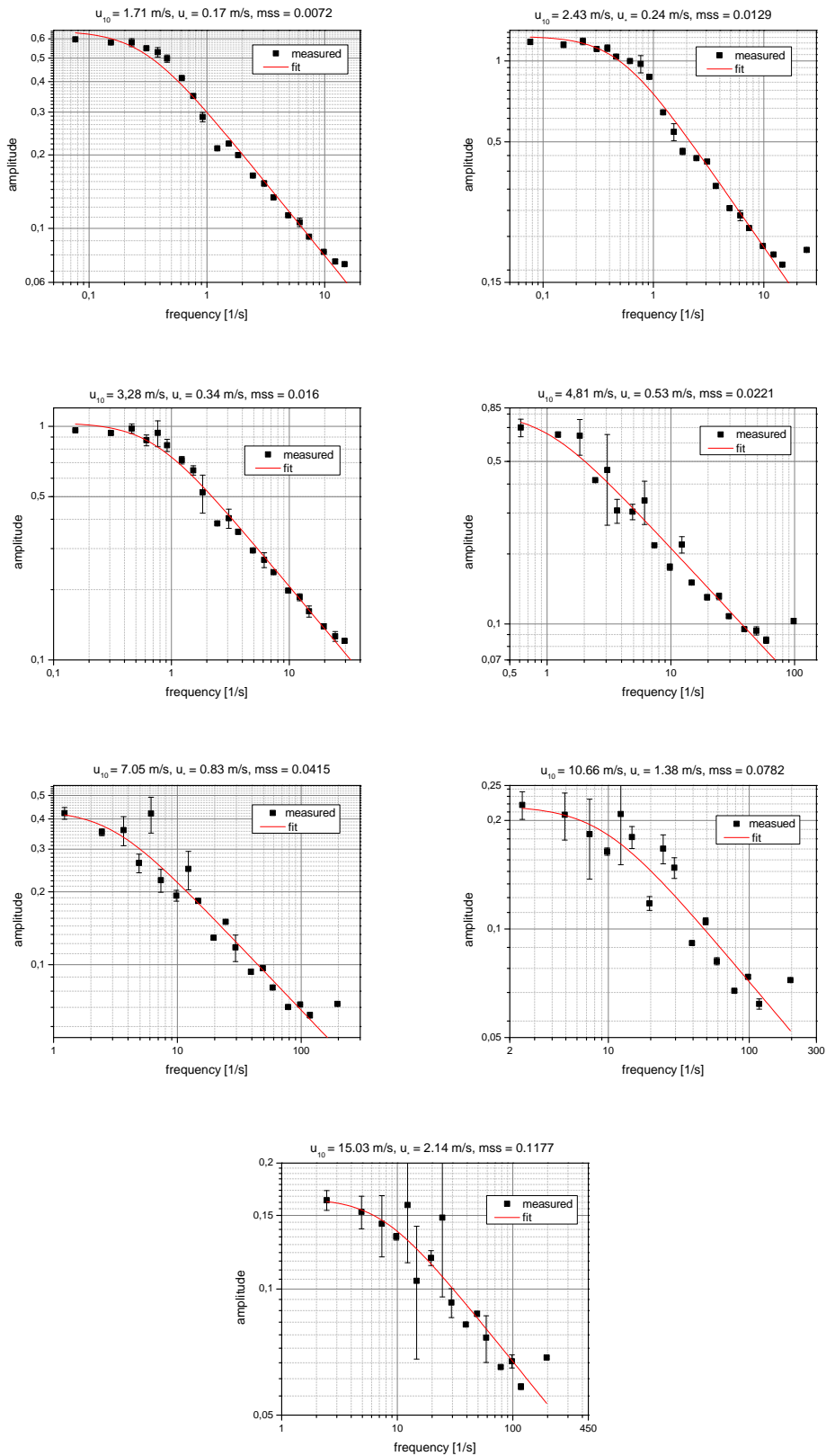
Figure A.3.: Measured amplitude values and fitted damping curves for the measurements conducted in the Aeolotron at 30.04.2010.

Table A.4 gives the fit values for all these curves in dependency of the wind speed u_{10}, the friction velocity u_* and the mean squared slope mss. Out of the response time τ, which is one of the fit parameter, the heat transfer velocity k_{heat} is calculated. It is given in table A.4, too. As the measurements were conducted under nearly constant temperature for all measurements a Schmidt number $Sc = 7.2$ for heat is used fot the scaling to gas transfer rates.

date	u_{10} $[\frac{m}{s}]$	u_* $[\frac{cm}{s}]$	mss	A	τ [s]	k_{heat} $[\frac{cm}{h}]$
26.04.	2.43	0.241	0.0129	1.239 ± 0.098	2.079 ± 0.520	94.74 ± 11.51
26.04.	10.66	1.380	0.0782	0.260 ± 0.068	0.160 ± 0.085	341.55 ± 88.06
28.04.	2.43	0.241	0.0129	1.248 ± 0.050	2.270 ± 0.259	90.67 ± 5.03
28.04.	3.28	0.337	0.0160	1.195 ± 0.175	2.108 ± 0.726	94.08 ± 15.75
28.04.	7.05	0.825	0.0415	0.565 ± 0.096	0.535 ± 0.196	186.85 ± 33.28
28.04.	10.66	1.380	0.0782	0.238 ± 0.028	0.101 ± 0.024	430.15 ± 49.27
28.04.	15.03	2.140	0.1177	0.150 ± 0.013	0.055 ± 0.010	583.12 ± 51.69
30.04.	3.28	0.337	0.0160	1.045 ± 0.058	2.807 ± 0.310	81.54 ± 4.37
30.04.	4.81	0.525	0.0221	1.183 ± 1.146	2.463 ± 4.834	87.05 ± 83.06
30.04.	7.05	0.825	0.0415	0.484 ± 0.173	0.491 ± 0.348	194.97 ± 67.17
30.04.	10.66	1.380	0.0782	0.201 ± 0.045	0.089 ± 0.041	458.57 ± 102.8
30.04.	15.03	2.140	0.1177	0.146 ± 0.010	0.060 ± 0.009	556.95 ± 42.42

Table A.4.: Fit parameters c_0 and τ and calculated heat transfer velocity for the measurements conducted in the Aeolotron in spring 2010.

A.2.2. Field Measurements

All three field measurement campaigns where evaluated with the amplitude damping method (see section 4.1.1). Figures A.4 to A.8 show the measured values and the fitted damping curves for all of the Baltic Sea measurements. The obtained fit values for the amplitude in the equilibrium state c_0 and the response time τ as well as their standard deviations δ and the fit statistic parameter R^2 are given in table A.5 to A.7 in respect to the measured wind speed. The calculated heat transfer velocity k_{heat} (with standard deviation) and the Schmidt numbers which can be used to scale the measured heat transfer rates are shown, too. For the measurements onboard FS Aranda a Schmidtnumber of $Sc = 10.17$ were used. For the measurements conducted onboard FS Alkor in 2010, a minimal resolvable heat transfer rated can be calculated due to the time a patch of the water surface can be imaged because of the movement of the ship (see section 6.1.2). These values are also given in table A.6.

u_{10} $[\frac{\mathrm{m}}{\mathrm{s}}]$	$\delta_{u_{10}}$ $[\frac{\mathrm{m}}{\mathrm{s}}]$	c_0	δ_{c_0}	τ [s]	δ_τ [s]	R^2	Sc	k_{heat} $[\frac{\mathrm{cm}}{\mathrm{h}}]$	$\delta_{k_{\mathrm{heat}}}$ $[\frac{\mathrm{cm}}{\mathrm{h}}]$
8.74	0.17	0.379	0.174	0.701	0.661	0.856	10.4	158.62	74.76
12.4	0.33	0.329	0.066	0.460	0.190	0.922	10.4	195.89	40.44
5.29	0.31	0.853	0.177	1.464	0.682	0.928	11.0	109.78	25.59
6.81	0.23	0.751	0.139	1.281	0.542	0.922	10.8	117.34	24.84
7.62	0.47	0.390	0.036	0.546	0.102	0.959	10.7	179.80	16.83

Table A.5.: Fit parameter c_0 and τ as well as Schmidt numbers Sc and the calculated heat transfer velocities k_{heat} in dependency of the wind speed for the measurements conducted onboard *FS Alkor* in spring 2009. δ gives the standard deviation of the corresponding values.
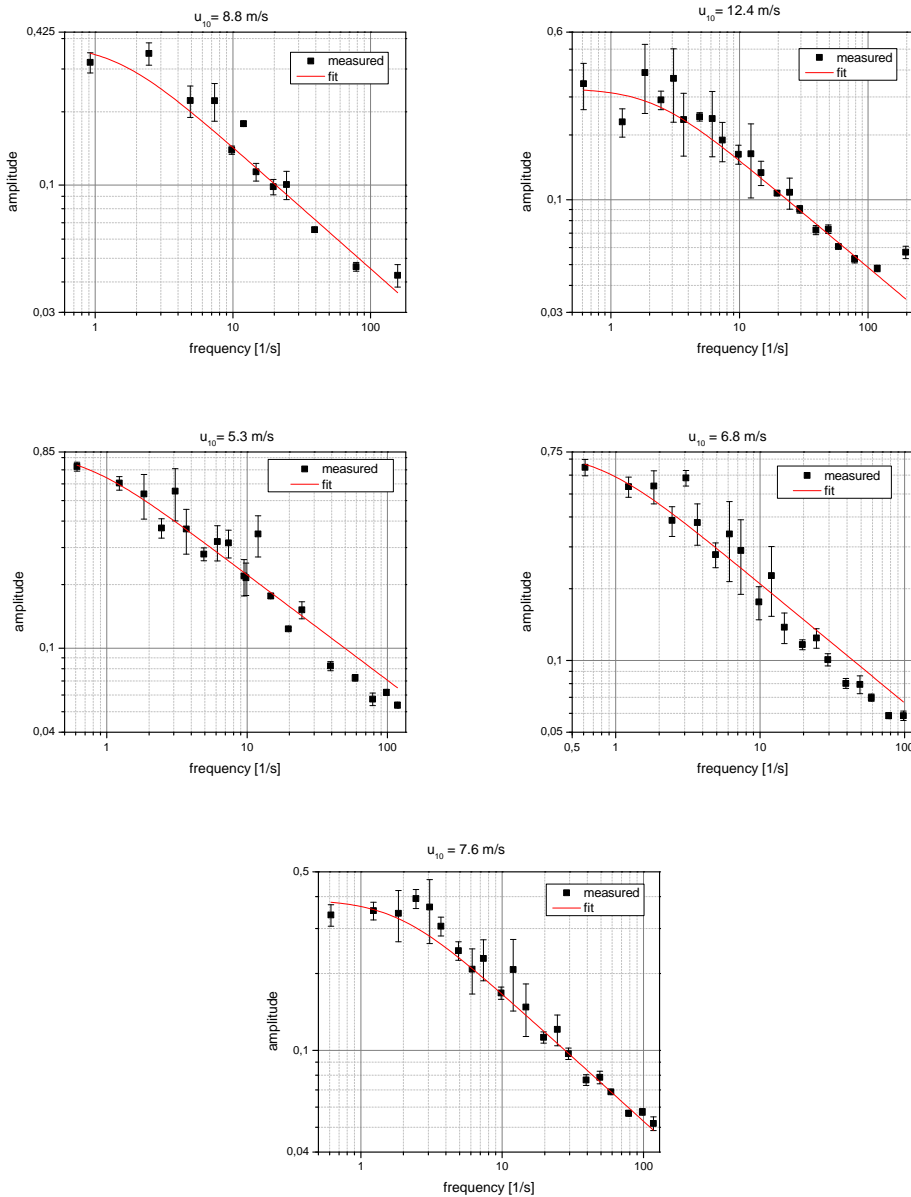
Figure A.4.: Measured amplitude values and fitted damping curves for the measurements conducted onboard *FS Alkor* in spring 2009.
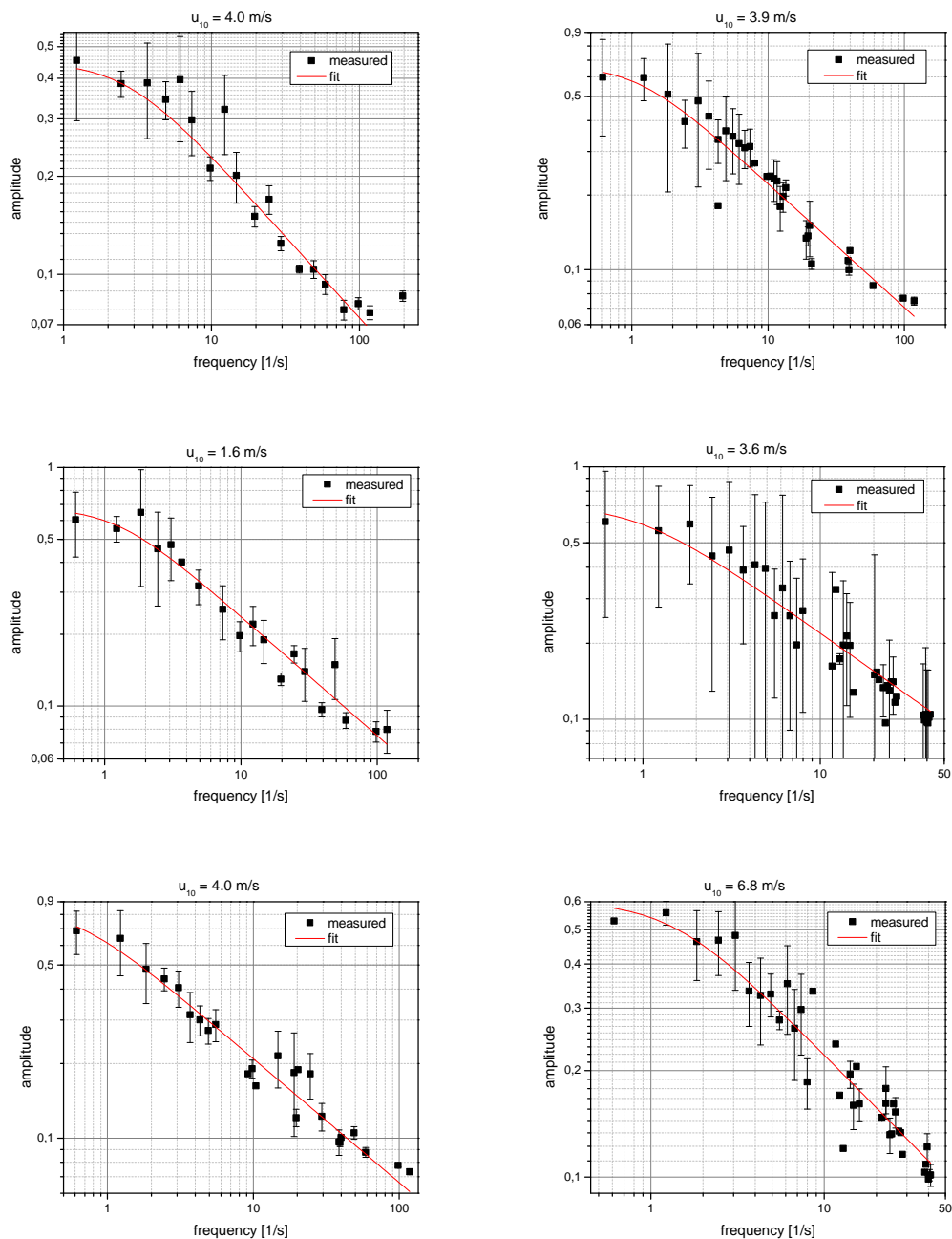
Figure A.5.: Measured amplitude values and fitted damping curves for the measurements conducted onbord *FS Alkor* in summer 2010 - part 1.
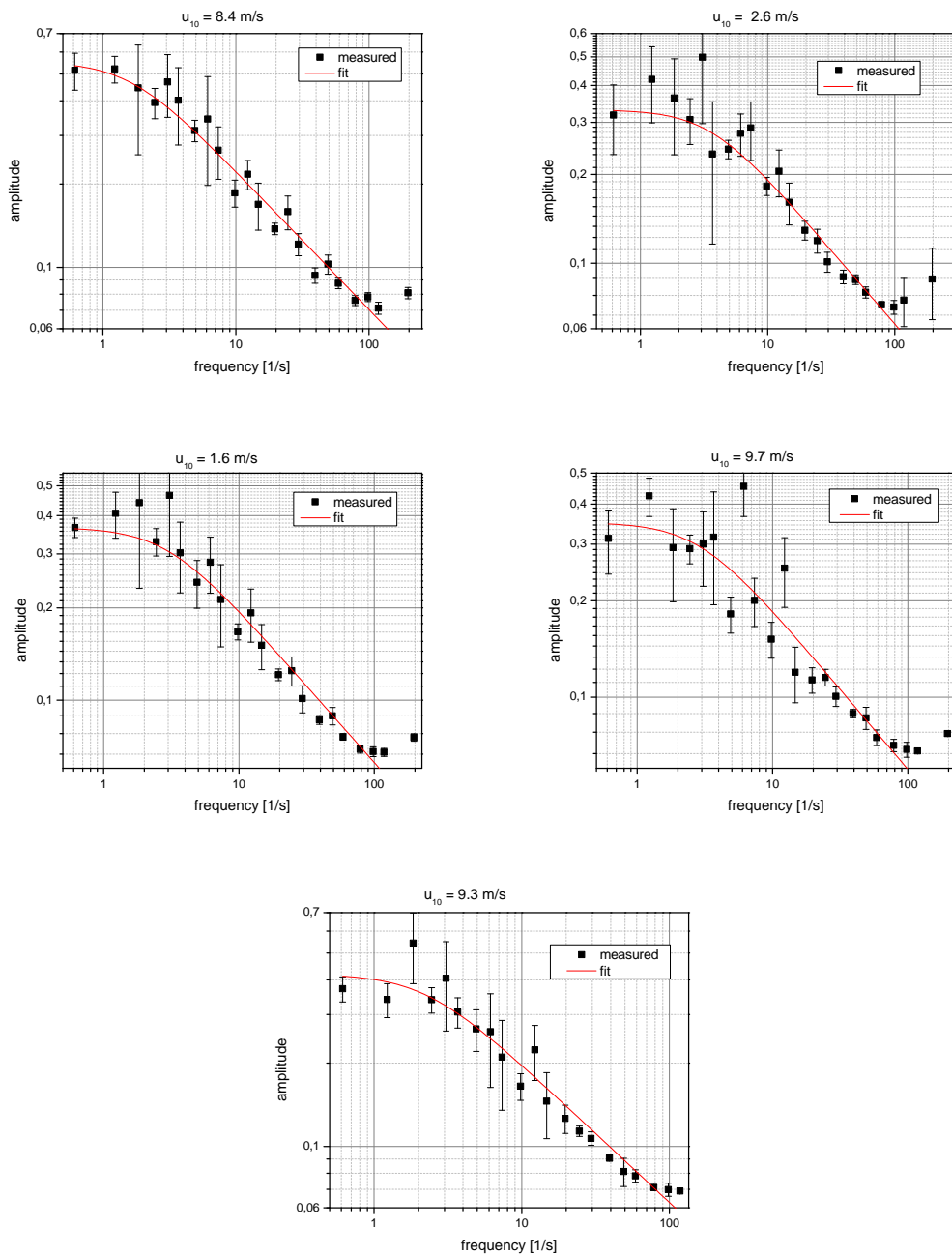
Figure A.6.: Measured amplitude values and fitted damping curves for the measurements conducted onbord *FS Alkor* in summer 2010 - part 2.
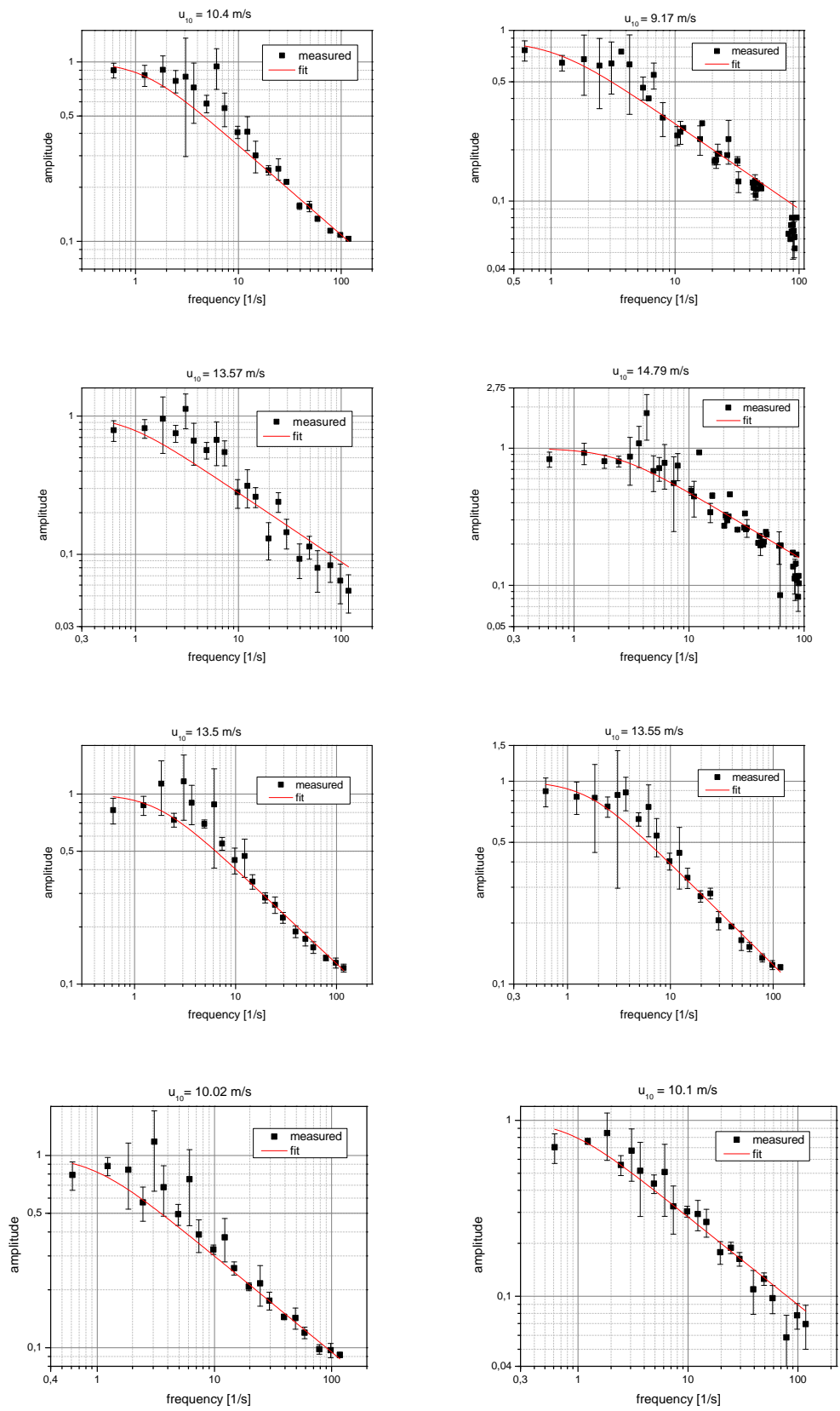
Figure A.7.: Measured amplitude values and fitted damping curves for the measurements conducted onbord *RV Aranda* in autumn 2010 - part 1.
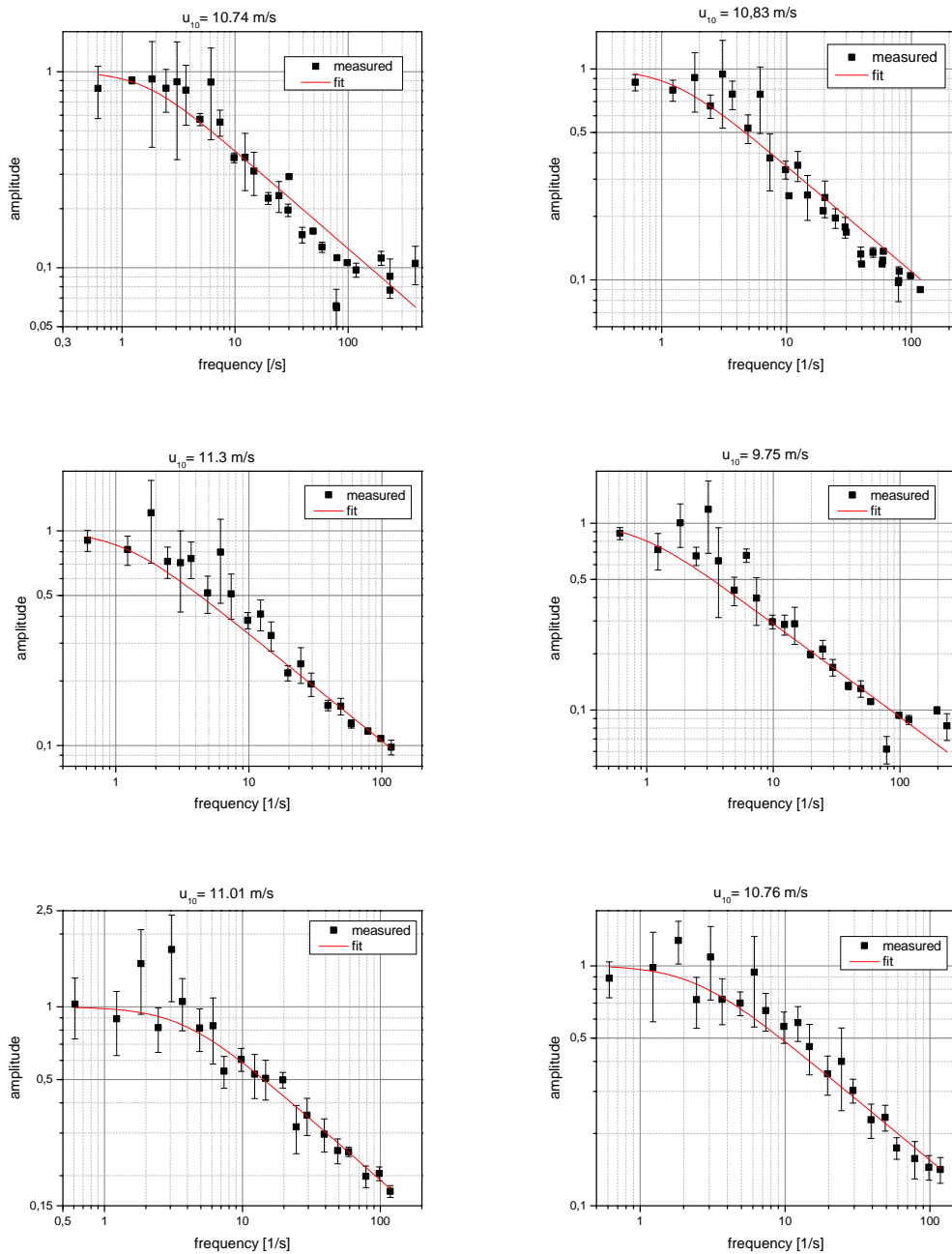
Figure A.8.: Measured amplitude values and fitted damping curves for the measurements conducted onbord *RV Aranda* in autumn 2010 - part 2.

u_{10} $\left[\frac{m}{s}\right]$	$\delta_{u_{10}}$ $\left[\frac{m}{s}\right]$	c_0	δ_{c_0}	τ [s]	δ_τ [s]	R^2	Sc	k_{heat} $\left[\frac{cm}{h}\right]$	$\delta_{k_{\text{heat}}}$ $\left[\frac{cm}{h}\right]$	k_{min} $\left[\frac{cm}{h}\right]$
4.02	0.33	0.449	0.208	0.373	0.355	0.477	7.6	217.38	103.33	77.72
3.94	0.30	0.670	0.089	0.906	0.271	0.892	7.7	139.55	20.88	82.52
1.60	0.22	0.680	0.065	0.818	0.192	0.951	7.3	146.86	17.20	75.43
3.61	0.22	0.708	0.087	1.040	0.281	0.901	7.3	130.22	17.60	79.37
4.02	0.53	0.852	0.126	1.656	0.536	0.954	7.1	103.22	16.70	79.37
6.70	0.15	0.602	0.056	0.736	0.155	0.903	8.1	154.85	16.34	76.05
8.34	0.32	0.554	0.147	0.619	0.338	0.732	8.2	168.75	46.05	73.56
2.64	0.26	0.331	0.046	0.284	0.081	0.920	7.2	249.36	35.73	105.00
1.63	0.34	0.366	0.092	0.341	0.178	0.385	7.2	227.34	59.22	92.76
9.72	0.13	0.351	0.042	0.348	0.116	0.810	7.0	225.29	37.56	-
9.27	0.28	0.420	0.037	0.449	0.104	0.918	7.0	198.20	23.01	-

Table A.6.: Fit parameter c_0 and τ, Schmidt number Sc and calculated heat transfer velocities k_{heat} in dependency of the wind speed for the measurements conducted onbord *FS Alkor* in summer 2010. δ gives the standard deviation of the corresponding values. Furthermore the minimal resolvable heat transfer rates k_{min} are given.

u_{10} $\left[\frac{m}{s}\right]$	$\delta_{u_{10}}$ $\left[\frac{m}{s}\right]$	c_0	δ_{c_0}	τ [s]	δ_τ [s]	R^2	k_{heat} $\left[\frac{cm}{h}\right]$	$\delta_{k_{\text{heat}}}$ $\left[\frac{cm}{h}\right]$
10.40	0.58	0.777	0.137	0.855	0.306	0.955	143.61	25.65
9.17	0.85	0.869	0.124	0.932	0.295	0.889	137.59	21.82
13.57	0.72	0.751	0.171	0.856	0.464	0.829	143.57	38.93
14.79	1.64	0.551	0.071	0.437	0.133	0.789	200.99	30.65
13.50	1.55	0.606	0.124	0.562	0.240	0.883	177.16	37.79
13.55	1.11	0.652	0.251	0.548	0.430	0.677	179.47	70.50
10.02	0.99	0.818	0.369	0.880	0.808	0.697	141.59	64.99
10.10	0.58	0.956	0.116	1.241	0.340	0.974	119.24	16.33
10.74	0.83	0.738	0.101	0.639	0.214	0.883	166.16	27.86
10.83	0.86	0.773	0.109	0.829	0.273	0.888	145.86	24.00
11.30	0.84	0.708	0.155	0.881	0.391	0.840	141.52	31.43
9.75	0.63	0.861	0.244	1.192	0.683	0.816	121.63	34.83
11.01	1.03	0.423	0.074	0.245	0.090	0.861	268.49	49.22
10.76	0.70	0.541	0.069	0.400	0.112	0.908	209.91	29.40

Table A.7.: Fit parameter c_0 and τ and calculated heat transfer velocities k_{heat} in dependency of the wind speed for the measurements conducted onbord *RV Aranda* in autumn 2010. δ gives the standard deviation of the corresponding values.

A.3. Results of the Faster Analysis Methods

A.3.1. Marseille 2012

For the measurements in Marseile in 2012 two different analysis methods were used: the decay curve method and the investigation of the spatial behaviour of amplitude and phase. Table A.8 shows the results of both analysis methods averaged for each measurement condition. The Schmidt number for heat was Sc = 7.

u_{ref} [$\frac{m}{s}$]	fetch [m]	2.2	4.6	9.6	27
2.5	k_d [$\frac{cm}{h}$]	51.88 ± 8.24	71.32 ± 9.79	61.81 ± 5.34	83.77 ± 8.56
	k_s [$\frac{cm}{h}$]	99.11 ± 31.26	71.8 ± 21.65	88.23 ± 20.44	76.03 ± 18.37
3	k_d [$\frac{cm}{h}$]	71.34 ± 17.75	84.23 ± 19.21	79.48 ± 14.3	103.46 ± 14.44
	k_s [$\frac{cm}{h}$]	109.05 ± 31.91	106.6 ± 33.86	99.85 ± 23.48	-
4	k_d [$\frac{cm}{h}$]	73.45 ± 13.24	104.21 ± 12.27	133.66 ± 13.34	129.07 ± 18.98
	k_s [$\frac{cm}{h}$]	131.77 ± 32.78	120.6 ± 30.13	131.55 ± 31.31	126.76 ± 49.73
5	k_d [$\frac{cm}{h}$]	134.18 ± 19.8	174.42 ± 18.61	186.15 ± 37.11	169.05 ± 15.72
	k_s [$\frac{cm}{h}$]	154.05 ± 30.39	157.24 ± 38.12	161.6 ± 47.35	119.58 ± 75.53
8	k_d [$\frac{cm}{h}$]	313.96 ± 53.51	291.16 ± 63.24	316.3 ± 81.69	362.32 ± 80.09
	k_s [$\frac{cm}{h}$]	203.36 ± 56.89	205.66 ± 51.57	217.57 ± 77.82	174.54 ± 55.91
10	k_d [$\frac{cm}{h}$]	396.95 ± 96.16	451.62 ± 88.65	439.9 ± 122.99	440.05 ± 119.53
	k_s [$\frac{cm}{h}$]	236.65 ± 75.13	219.03 ± 81.63	207.79 ± 66.34	241.89 ± 78.4

Table A.8.: Heat transfer rates determined with the decay curve method k_d and with the investigation of the spatial behaviour of amplitude and phase k_s in dependence of the reference wind speed and the fetch for the measurements conducted in Marseille in 2012.

fetch	2.5	3	u_{ref} [$\frac{m}{s}$] 4	5	8	10
2	n.a.	3.50	4.44	5.60	9.00	11.5
4	n.a.	3.23	4.38	5.51	9.14	11.7
9	n.a.	3.00	4.23	5.58	9.34	12.1
26.2	2.62	3.31	4.65	5.80	9.57	12.6

Table A.9.: Wind speed in ten meter height in $\frac{m}{s}$ for the measurement conditions in Marseille, provided by Guillemette Caulliez. Values marked with n.a. are not available.

fetch	2.5	3	u_{ref} [$\frac{m}{s}$] 4	5	8	10
2	n.a.	0.09	0.12	0.16	0.26	0.34
4	n.a.	0.09	0.12	0.16	0.29	0.40
9	n.a.	0.08	0.12	0.18	0.33	0.45
26.2	0.07	0.10	0.15	0.20	0.25	0.49

Table A.10.: Friction velocity in $\frac{m}{s}$ for the measurement conditions in Marseille, provided by Guillemette Caulliez. Values marked with n.a. are not available.

fetch	u_{ref} $[\frac{m}{s}]$					
	2.5	3	4	5	8	10
2	n.a.	0.0014	0.006	0.392	3.67	4.61
4	n.a.	0.0021	0.231	1.54	3.89	5.08
9	n.a.	0.0092	1.19	2.39	4.69	5.72
26.2	0.742	1.25	1.97	2.53	4.95	6.83

Table A.11.: Mean square slope in $[\frac{m}{s}]$ multiplied with 100 for the measurement conducted in Marseille, provided by Guillemette Caulliez. Values marked with n.a. are not available.

Table A.9, A.10 and A.11 give the wind speed in ten meters height, the friction velocity and the mean square slope for conditions, similar to the ones under which the measurements used in this thesis were conducted. This data were used for the comparison between the both wind-wave flumes. The data are provided by Guillemette Caulliez, Mediterranean Institute of Oceanography, Marseille-Luminy, France.

A.3.2. Aeolotron 2013

For the measurements in Heidelberg in 2013 the same analysis methods as for the measurements in Marseille were used: the decay curve method and the investigation of the spatial behaviour of amplitude and phase. Table A.12 shows the results of both analysis methods averaged for each measurement condition. For the measurements on 08.05 and 10.05. at condition five the surfactant ruptured. To take this into account, condition five was divided in three parts.

Condition	1	2	3	4	5	6	7
30.04.	2.48	4.02	5.18	6.62	8.39	11.24	14.26
03.05.	2.62	4.19	5.39	6.71	8.43	11.35	14.42
08.05.	-	-	4.03	5.37	8.09	11.11	14.2
10.05.	1.71	2.94	4.20	5.52	7.99	11.19	14.22

Table A.13.: Wind speed in ten meter height in $\frac{m}{s}$ for the measurement conditions in Heidelberg in 2013, provided by Kerstin Krall.

Condition	30.04.	03.05.	08.05.	10.05.
1	0.167 ± 0.017	0.185 ± 0.019	-	0.130 ± 0.015
2	0.286 ± 0.029	0.300 ± 0.030	-	0.206 ± 0.021
3	0.387 ± 0.039	0.406 ± 0.041	0.287 ± 0.029	0.301 ± 0.030
4	0.529 ± 0.053	0.534 ± 0.054	0.404 ± 0.041	0.419 ± 0.042
5	0.729 ± 0.073	0.734 ± 0.073	0.694 ± 0.069	0.382 ± 0.068
6	1.101 ± 0.110	1.116 ± 0.112	1.082 ± 0.108	1.069 ± 0.109
7	1.552 ± 0.156	1.578 ± 0.158	1.543 ± 0.155	1.546 ± 0.155

Table A.14.: Water-side friction velocity in $\frac{cm}{s}$ for the measurement conditions in Heidelberg in 2013, provided by Maximilian Bopp.

	date	30.04.	03.05.	08.05.	10.05.
1	$k_d \left[\frac{cm}{h}\right]$	69.54 ± 2.50	65.94 ± 4.82	75.44 ± 4.91	72.00 ± 3.91
	$k_s \left[\frac{cm}{h}\right]$	103.22 ± 21.40	109.02 ± 47.45	102.18 ± 41.46	135.65 ± 22.85
2	$k_d \left[\frac{cm}{h}\right]$	91.35 ± 6.73	95.94 ± 11.04	102.27 ± 8.22	95.72 ± 7.83
	$k_s \left[\frac{cm}{h}\right]$	90.12 ± 43.42	102.55 ± 46.13	115.18 ± 37.94	120.34 ± 25.87
3	$k_d \left[\frac{cm}{h}\right]$	108.62 ± 10.76	114.22 ± 16.86	104.61 ± 9.87	-
	$k_s \left[\frac{cm}{h}\right]$	137.56 ± 32.24	139.10 ± 66.5	151.18 ± 34.76	184.19 ± 25.66
4	$k_d \left[\frac{cm}{h}\right]$	162.82 ± 51.94	201.50 ± 42.92	133.93 ± 8.50	164.48 ± 26.65
	$k_s \left[\frac{cm}{h}\right]$	154.35 ± 48.35	164.44 ± 68.48	177.01 ± 44.10	171.62 ± 57.06
5-1	$k_d \left[\frac{cm}{h}\right]$	319.55 ± 60.93	354.30 ± 50.42	197.61 ± 34.86	198.97 ± 19.21
	$k_s \left[\frac{cm}{h}\right]$	201.85 ± 55.75	218.74 ± 86.20	79.16 ± 25.96	229.19 ± 92.68
5-2	$k_d \left[\frac{cm}{h}\right]$	ns	ns	236.42 ± 47.53	213.44 ± 26.27
	$k_s \left[\frac{cm}{h}\right]$	ns	ns	224.44 ± 118.36	234.48 ± 88.65
5-3	$k_d \left[\frac{cm}{h}\right]$	ns	ns	230.03 ± 71.68	211.28 ± 17.09
	$k_s \left[\frac{cm}{h}\right]$	ns	ns	260.73 ± 89.91	228.54 ± 89.43
6	$k_d \left[\frac{cm}{h}\right]$	481.72 ± 108.23	499.98 ± 82.70	508.29 ± 118.03	543.51 ± 199.70
	$k_s \left[\frac{cm}{h}\right]$	211.54 ± 78.90	259.29 ± 92.27	239.54 ± 101.61	272.22 ± 102.08
7	$k_d \left[\frac{cm}{h}\right]$	621.61 ± 59.68	638.02 ± 143.68	745.59 ± 110.63	660.54 ± 134.04
	$k_s \left[\frac{cm}{h}\right]$	229.36 ± 91.56	343.54 ± 169.35	319.61 ± 157.32	24.84 ± 107.36

Table A.12.: Heat transfer rates determined with the decay curve method k_d and with the investigation of the spatial behaviour of amplitude and phase k_s in dependence of the reference wind speed and the fetch for the measurements conducted in Heidelberg in 2013. For the measurements on 30.04. and 03.05 the surfactant did not rupture. Therefore condition five was not splited (ns).

Condition	1	2	3	4	5	6	7
30.04.	0.006	0.011	0.013	0.014	0.039	0.079	0.115
03.05.	0.007	0.013	0.016	0.022	0.05	0.083	0.119
10.05.	0.002	0.002	0.0024	0.002	0.02	0.08	0.114

Table A.15.: Mean square slope in $\frac{m}{s}$ for the measurements conducted in Heidelberg in 2013, provided by Daniel Kiefhaber and Svenja Reith.

Table A.13, A.14 and A.15 give the wind speed in ten meters height, the friction velocity and the mean square slope for conditions under which the measurements were conducted.

A.4. Results of the Gas Exchange Measurements

The gas exchange measurements conducted by co-workers have been used for comparison with the measured heat transfer velocity. The used values are given in this chapter.

A.4.1. Aeolotron 2010

The gas exchange measurements in the Aeolotron in 2010 were conducted by Kerstin Krall and analysed with an mass balance approach by Christine Kräuter. The resulting transfer rates (unpublished data) for the measurements on 30.04.2010 are given in table A.16.

u_{ref} [$\frac{m}{s}$]	2.00	2.75	3.65	4.85	6.50	8.65
u_{10} [$\frac{m}{s}$]	2.43	3.27	4.81	7.05	10.6	15.0
k_{N_2O} [$\frac{cm}{h}$]	3.787	5.243	7.567	14.970	32.675	53.996

Table A.16.: Transfer velocities for nitrous oxide (k_{N_2O}) in dependency of the reference wind speed and the wind speed in ten meters height measured in the Aeolotron 2010.

A.4.2. Aeolotron 2011

The gas transfer measurements for nitrous oxide in the Aeolotron in 2011 were conducted and analysed by [Krall, 2013]. As heat transfer rates are not available for the same year, but conducted under the same conditions in 2010, for comparison the gas transfer rates were averaged over all measuring days without surfactants. Table A.17 shows this values as well as the determined Schmidt number exponents.

u_{ref} [$\frac{m}{s}$]	1.5	2.0	2.75	3.65	4.85	6.5	8.65
u_{10} [$\frac{m}{s}$]	1.71	2.43	3.27	4.81	7.05	10.6	15.0
k_{N_2O} [$\frac{cm}{h}$]	3.135	4.351	5.278	7.085	19.162	44.177	64.822
δ_k [$\frac{cm}{h}$]	0.810	0.787	1.734	7.702	16.831	15.116	21.262
n	0.673	0.661	0.617	0.586	0.556	0.517	0.485

Table A.17.: Transfer velocities for nitrous oxide (k_{N_2O}) and Schmidt number exponents n in dependency of the reference wind speed and the wind speed in ten meters height, measured in the Aeolotron in 2011 - averaged values from Krall [2013]. The given δ are the standard deviations for the averaging transfer velocities.

A.4.3. Marseille 2012

Gas transfer measurements were conducted in 2006 by Kai Degreif (unpublished data) under the same conditions as the heat transfer measurements conducted in 2012. Table A.18 gives the measured transfer rate for nitrous oxide in dependency of the wind speed. The transfer rates were determined with an mass balance method, integrating over the whole facility. The water temperature changed during the measurements, therefore different Schmidt numbers for nitrous oxide have to be assumed for the different conditions. They are also given in the table.

u_{10} $[\frac{m}{s}]$	2.5	3	4	5	8	10
k_{N_2O} $[\frac{cm}{h}]$	2.536	4.010	6.528	10.144	20.343	29.754
Sc	703.3	718.5	714.7	754.4	730.3	746.3

Table A.18.: Transfer velocities for nitrous oxide (k_{N_2O}) in dependency of the wind speed in ten meters height, measured in Marseille in 2006.

A.4.4. Aeolotron 2013

The gas transfer measurements in the Aeolotron in 2013 were conducted and analysed in the same way like the ones in 2011. The analysis is described in [Krall, 2013]. The data are still under evaluation and only preliminary results for the transfer rates and Schmidt number exponents are given in table A.19.

date	condition	1	2	3	4	5.1	5.2	5.3	6	7
30.04.	u_{ref} $[\frac{m}{s}]$	1.46	2.08	2.68	3.61	4.81	ns	ns	6.43	8.17
	k $[\frac{cm}{h}]$	1.31	2.13	3.16	5.19	11.48	ns	ns	26.36	42.1
	Sc	597.2	596.8	596.6	596.7	596.7	ns	ns	596.8	596.9
	n	0.719	0.686	0.641	0.588	0.511	ns	ns	0.465	0.467
03.05.	u_{ref} $[\frac{m}{s}]$	1.46	2.09	2.68	3.61	4.8	ns	ns	6.43	8.16
	k $[\frac{cm}{h}]$	1.52	2.55	4.47	7.8	12.27	ns	ns	30.22	46.4
	Sc	620.3	618.5	618.2	617.9	618.3	ns	ns	617.7	616.4
	n	0.767	0.693	0.641	0.613	0.560	ns	ns	0.504	0.466
08.05.	u_{ref} $[\frac{m}{s}]$	1.47	2.11	2.72	3.67	4.87	4.86	4.84	6.47	8.19
	k $[\frac{cm}{h}]$	0.66	0.95	1.52	2.21	5.74	7.13	8.01	25.51	42.31
	Sc	597.2	496.2	596.1	595.2	595.4	595.2	595.1	595.1	595.0
	n	0.713	0.681	0.715	0.748	0.623	0.576	0.492	0.464	0.498
10.05.	u_{ref} $[\frac{m}{s}]$	1.44	2.11	2.73	3.67	4.87	4.85	4.84	6.45	8.17
	k $[\frac{cm}{h}]$	0.72	1.08	1.6	2.21	6.0	7.06	7.48	26.29	42.38
	Sc	590.5	589.5	589.1	588.8	588.5	588.5	588.5	589.3	589.3
	n	0.865	0.861	0.905	0.882	0.727	0.64	0.551	0.493	0.477

Table A.19.: Transfer velocities for nitrous oxide k , Schmidt numbers Sc and Schmidt number exponents n in dependency of the reference wind speed, measured in the Aeolotron in 2013 - preliminary results, provided by Kerstin Krall. At the first two measuring days, the surfactant did not rupture during condition five, therefore the condition was not splitet for the evaluation (ns).

Danksagung